Contents lists available at ScienceDirect

Materials Science & Engineering R

journal homepage: www.elsevier.com

High-Efficiency Silicon Heterojunction Solar Cells: Materials, Devices and Applications

Yuqiang Liu [a], Yajuan Li [a], Yiliang Wu [c], Guangtao Yang [d], Luana Mazzarella [d], Paul Procel-Moya [d], Adele C. Tamboli [e], Klaus Weber [c], Mathieu Boccard [f], Olindo Isabella [d], Xinbo Yang [b,*], Baoquan Sun [a,*]

[a] Jiangsu Key Laboratory for Carbon-Based Functional Materials & Devices, Institute of Functional Nano & Soft Materials (FUNSOM), Joint International Research Laboratory of Carbon-Based Functional Materials and Devices, Soochow University, 199 Ren'ai Road, Suzhou, 215123, Jiangsu, PR China
[b] College of Energy, Soochow Institute for Energy and Materials InnovationS (SIEMIS), Soochow University, Suzhou 215006, PR China
[c] Research School of Electrical, Energy and Materials Engineering (RSEEME), Australian National University, Canberra 2601, Australia
[d] Photovoltaic Materials and Devices Group, Delft University of Technology, Mekelweg 4, 2628 CD, Delft, the Netherlands
[e] National Renewable Energy Laboratory, Golden, CO, 80401, United States
[f] Photovoltaics and Thin-Film Electronics Laboratory (PV-lab), Institute of Microengineering (IMT), Ecole Polytechnique Federale de Lausanne (EPFL), Rue de La Maladiere 71b, CH-2002, Neuchatel, Switzerland

ARTICLE INFO

Keywords:
Heterojunction silicon solar cells
Amorphous silicon
Transition metal oxide
Organic Semiconductor
Halide Perovskite
Device physics

ABSTRACT

Photovoltaic (PV) technology offers an economic and sustainable solution to the challenge of increasing energy demand in times of global warming. The world PV market is currently dominated by the homo-junction crystalline silicon (c-Si) PV technology based on high temperature diffused p-n junctions, featuring a low power conversion efficiency (PCE). Recent years have seen the successful development of Si heterojunction technologies, boosting the PCE of c-Si solar cells over 26%. This article reviews the development status of high-efficiency c-Si heterojunction solar cells, from the materials to devices, mainly including hydrogenated amorphous silicon (a-Si:H) based silicon heterojunction technology, polycrystalline silicon (poly-Si) based carrier selective passivating contact technology, metal compounds and organic materials based dopant-free passivating contact technology. The application of silicon heterojunction solar cells for ultra-high efficiency perovskite/c-Si and III-V/c-Si tandem devices is also reviewed. In the last, the perspective, challenge and potential solutions of silicon heterojunction solar cells, as well as the tandem solar cells are discussed.

1. Introduction

Energy is an indispensable necessity for human survival. As global energy consumption is expected to be doubled by the midcentury due to population and economic growth, it is critical to conserving our natural resources [1]. A large quantity of fossil energy expended to meet human daily requirements also entails the release of pollutants that lead to an unsustainable balance between humans and nature. Hence, renewable energy will be one of the strongest determinants of global development over the coming century. Among the present renewable energy sources, solar energy is one of the most widely exploitable sources. Nevertheless, it is challenged to efficiently capture and convert solar energy into a useful form of energy for human use.

Over the past decades, photovoltaic (PV) technologies have been developed to address this challenge, converting solar energy to electricity. In 1954, the first valuable crystalline silicon (c-Si)-based solar cell was demonstrated at the Bell Labs [2]. Ever since, various PV technologies, from materials to devices, have attracted intensive investigation. Up to now, single-junction solar cells can be divided into three classes according to the absorber material and evolution: (i) c-Si solar cells; (ii) thin-film inorganic solar cells, mainly including cadmium telluride (CdTe), copper indium gallium selenide (CIGS), thin-film Si, gallium arsenide (GaAs), and indium phosphide (InP); (iii) emerging solar cells, such as perovskite, organic, dye-sensitized, and quantum dot solar cells [3].

Although thin-film and emerging solar cells have demonstrated remarkable progress, the world PV market is currently dominated by the c-Si PV technology, occupying a very high market share of ~95% in 2019, thanks to its combination of high power conversion efficiencies (PCEs), long stability, use of non-toxic and abundant materials, as well as its well-developed, scaled processing techniques. As the second most abundant element of the Earth's crust, Si provides an enormous source for the semiconductor field. Importantly, the fierce market competi-

* Corresponding authors.
Email addresses: louis.xbyang@gmail.com (X. Yang); bqsun@suda.edu.cn (B. Sun)

https://doi.org/10.1016/j.mser.2020.100579
Received 29 May 2020; Received in revised form 20 July 2020; Accepted 30 July 2020
Available online xxx
0927-796/

tion in integrated circuit chips field stimulates worldwide scientific and technical investments. Thus, the fundamental properties of Si are relatively well understood. The relevant techniques, such as c-Si ingot growth and wafer processing, could be utilized in c-Si PV industry directly, which provides c-Si solar cells with a dominant advantage, compared to other semiconductor materials. Moreover, the bandgap of c-Si (1.12 eV) is almost ideal to match the solar spectrum, making c-Si material an excellent solar converter.

Silicon solar cells so far can be divided into diffusion-based homojunction solar cells and Si heterojunction solar cells, according to their device technologies. Currently, the dominant PV productions are homojunction c-Si solar cells, mainly including aluminum back surface field (Al-BSF) cell and passivated emitter and rear cell (PERC), occupying a market share of 40% and 50% in 2019, respectively [4]. A typical p-type Al-BSF cell (Fig. 1 (a)) features a phosphorus-doped n^+ emitter and an aluminum (Al) doped p^+ BSF, which is formed by a firing process after screen-printing Al paste. Melted Si would recrystallize into a region containing Al during a cooling process. This is equivalent to a doping process resulting in the formation of a p^+ BSF, which is highly p-type doped and hence not very conductive to electrons, preventing the latter to reach the rear metal surface and reducing recombination. The Al-BSF technology is of importance for the success of Si PV industry in the last decade. However, the PCE of Al-BSF cell ($\lesssim$ 20%) is mainly limited by the high carrier recombination velocity at Si rear surface.

To reduce rear surface recombination losses, a passivation dielectric layer is inserted between the Si rear side and Al contacts, resulting in so-called PERC technology (Fig. 1 (b)) technology [5]. A world-record PCE of 25% has been achieved on lab-size PERC cell in 1999 [6,7], using thermally-grown Si dioxide (SiO_2) passivation at both sides. On industrial production lines, aluminum oxide (Al_2O_3) is the most widely used rear passivation layer, featuring excellent and stable passivation on p-type Si, thanks to a high negative charge density ($\sim 10^{13}$ cm^{-2}) that shields the electrons at the c-Si surface [8]. Additionally, local p^+ BSF can be formed simultaneously during the laser contact opening at the rear side. Similarly, the PCE of PERC cells with a diffused p-n junction and BSF is mainly limited by the high carrier recombination losses at the metal-Si contact regions. When directly in contact with c-Si, metals induce large densities of electronic states near the interface within the bandgap of Si, resulting in > 50% recombination losses in high efficiency c-Si solar cells [9]. Besides, heavily doping also induces Auger recombination, bandgap narrowing and free carrier absorption in c-Si, which further limit the device performance [10]. According to the research and development (R&D) roadmap (Fig. 1 (c)), the PCE limit of industrial Al-BSF and PERC production is ~20% and ~24%, respectively [11].

The main objective of c-Si PV technology development is to increase the PCE and reduce further the production costs, aiming to reduce the levelized cost of electricity (LCOE). Since 2015, remarkable PCE improvement has been made on c-Si solar cells [13], mainly rely on the development of Si heterojunction solar cells using advanced passivating contact technology. As predicted in Fig. 1 (c), c-Si heterojunction solar cells with passivating contacts will be the next generation high-efficiency PV production ($\geq$ 25%) after PERC. This article reviews the recent development of high-efficiency Si heterojunction solar cells based on different passivating contact technologies, from materials to devices. The development status of ultra-high efficiency tandem devices based on c-Si heterojunction bottom cell is also reviewed. The basic theory and characterization of c-Si heterojunction solar cells, including charges separation and carrier selectivity formation, carrier recombination and minority carrier lifetime in c-Si, parameters of solar cells, and related characterization techniques, are briefly presented in Section 2. C-Si solar cells based on Si heterojunction technology and polycrystalline Si (poly-Si) passivating contact technology have achieved very high efficiencies of 26.7% and 26.1%, respectively [14,15]. These doped Si layer-based passivating contacts and devices demonstrate the desired scheme achieving higher efficiency at a low cost, which will be discussed in detail in Section 3. In the meantime, metal compounds, organic and two dimensional (2D) materials with extremely low or high work function (WF) and/or suitable band alignment with c-Si were intensively investigated as so-called dopant-free passivating contacts for c-Si solar cells [10,16]. The most successful examples are electron-selective titanium dioxide (TiO_2) and hole-selective molybdenum oxide (MoO_x) contacts, achieving a high PCE of 22.1% and 23.5%, respectively, using a simple full-area contact architecture [17,18]. These dopant-free passivating contacts are easy to deposit using simple techniques at a low temperature, such as thermal evaporation, sputtering, atomic layer deposition (ALD) and spin coating, and will be discussed in Section 4. The tandem structure is a promising scheme to achieve ultrahigh efficiency, surpassing the Shockley-Queisser limit of single-junction c-Si solar cells (> 29.4%). The 1.12 eV bandgap makes c-Si solar cells an ideal bottom sub-cell for a tandem device, which will be discussed in Section 5. Metal halide perovskite materials with a tunable bandgap are a promising candidate for top sub-cell, and a certified high efficiency of 29.1% has been reported for perovskite/c-Si tandem solar cells [19]. III-V/c-Si tandem devices have also demonstrated an ultrahigh efficiency of up to 35.9% [13,20]. All above have demonstrated that the development of high-efficiency c-Si heterojunction solar cells as well as tandem devices

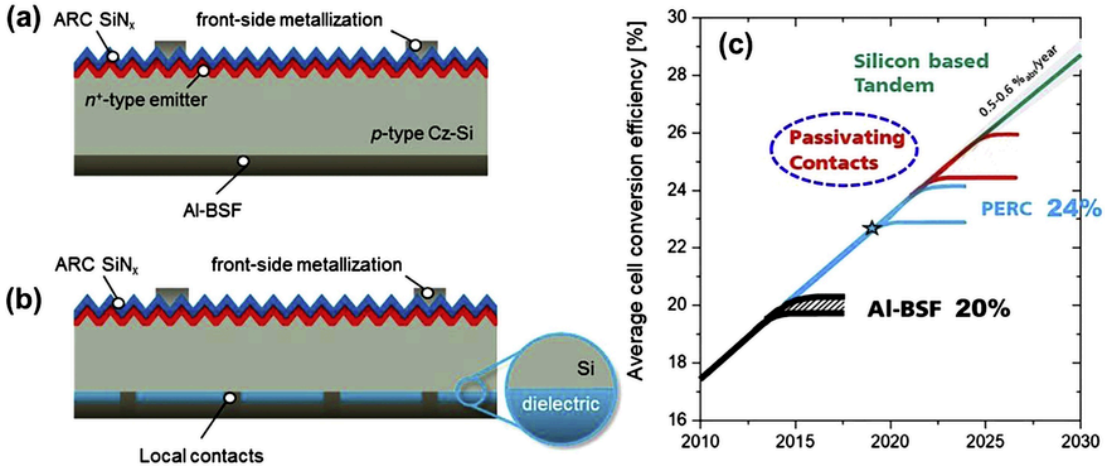

Fig. 1. Schematic of (a) Al-BSF and (b) PERC cells. Reprinted with permission from ref. [12]. Copyright 2017, Elsevier. (c) Research and development roadmap of c-Si PV productions. Reprinted with permission from ref. [11]. Copyright 2020, The American Institute of Physics. (Al-BSF: aluminum back surface field cell, PERC: passivated emitter and rear cell).

are very successful in the last couple of years, which deserves a comprehensive review to summarize these progress.

2. Basic theory and characterization of c-Si heterojunction solar cells

2.1. Charges separation and carrier selectivity formation

A comprehensive theory of c-Si heterojunction solar cells is that selective transport of photo-generated charges is achieved by the vastly asymmetrical conductivity of electrons and holes [21], which can be originated from exterior doping processes or intrinsic properties of materials. The different conductivities of electrons and holes in two regions of c-Si solar cells can be identified as the essential ingredient for charge carrier separation [21]. Electron-selective transport layers that possess a large electron conductivity and a smaller hole conductivity admit electrons being through the contact region and block holes. While, holes-selective transport layers possess an opposite conductivity, corresponding to the hole selectivity. Typically, when p-n homojunction under illumination, the current is mainly carried by electrons at the electron contact side (phosphorus diffused regions), due to a large conductivity of electrons. Although the holes subject to a much larger driving force toward the electron contact side, corresponding to a larger gradient in their quasi-Fermi energy, their current is smaller than the electron current due to the much smaller hole conductivity [21]. As for p-i-n heterojunction under illumination, two wide bandgap functional layers with different conductivities of electrons and holes (*e.g.*, doped hydrogenated amorphous Si (a-Si:H)) provide the function of charge separation and carrier selective transport. One layer with a larger electron conductivity (*e.g.*, phosphorus-doped a-Si:H) charges for electron-selective transport. On the contrary, the opposite layer charges for hole-selective transport, owing to its larger hole conductivity (*e.g.*, boron-doped a-Si:H). The reason for carrier separation and efficient device operation is that the p-i-n heterojunction ensures a very small minority carrier conductivity in the wide bandgap transport layers in both dark and illumination conditions, which minimizes the carrier recombination at the metal contacts [21]. For efficient c-Si heterojunction solar cells, especially these dopant-free passivating contact materials we are going to discuss in Section 4, it is necessary that the Fermi energy of the electron-selective contact is at higher energies than the conduction band minimum of c-Si. Similarly, the Fermi energy of the hole-selective contact has to be lower than the maximum of the valence band. Then the work functions lead to electron (hole) accumulation at the electron (hole) contact combined with a depletion of the other kind of charge carrier, resulting in large different conductivities of electrons and holes in the vicinity of the contacts [21].

2.2. Carrier recombination and minority carrier lifetime

The density of electrons and holes in the equilibrium state is expressed by n_0 and p_0, respectively. After absorbing incident photons, non-equilibrium electrons (Δn) and holes (Δp) are generated. At this moment, the density of electron and hole are n and p, respectively: $n = n_0 + \ \ n$, $p = p_0 + \ \ p$. The system with non-equilibrium carriers is in a meta-stable state and would stabilize to an equilibrium condition by electrons and holes recombination that includes radiative recombination, defect-assisted (*e.g.* Shockley-Read-Hall (SRH)) recombination, and Auger recombination [22,23].

Radiative recombination is caused by the direct recombination of electrons and holes, accompanied by the emission of photons. Since c-Si is an indirect bandgap material, this phenomenon requires the simultaneous absorption or emission of a phonon, making this recombination mechanism non-dominant in c-Si solar cells.

SRH recombination is caused by defects and impurities in Si wafer. Unlike radiative recombination, SRH recombination releases energy in the form of vibration relaxation. SRH recombination is processes of capturing and recombining charges, corresponding a recombination rate (U) [22,23]:

$$U = \frac{N_t r_n r_p \left(np - {n_i}^2\right)}{r_n\left(n + N_c e^{\left(\frac{E_t - E_c}{k_0 T}\right)}\right) + r_p\left(p + N_v e^{\left(-\frac{E_t - E_v}{k_0 T}\right)}\right)}$$

where, N_t is the density of recombination center, r_n (or r_p) is the capture coefficient of an electron (or hole), N_C (or N_V) is the density of states of conduction band (E_C) (or valance band (E_V)), E_t is the traps energy level. When E_t is close to E_C (or E_V), *i.e.*, shallow energy level, the captured electrons (or holes) re-emit back to E_C (or E_V) easily, rather than recombined with the holes (or electrons). However, when the position of E_t is deep, the SRH recombination is relatively serious. Defects and impurities, such as iron, nickel, copper and chromium, generate trap energy levels that significantly suppress the efficiency of c-Si solar cells [24,25]. Iron generates deep-level trap energy with a larger capture cross-section of charges. Consequently, the effective lifetime of Si wafer with a high iron concentration is much lower [26]. Nickel can diffuse to and precipitate at Si surfaces during cooling process, because of its fast-diffusing property [27]. This causes serious surface recombination. Typically, these impurities, especially the detrimental iron, can be removed by gettering using high-temperature phosphorus or boron diffusion [28]. Surface passivation films (*e.g.* SiO_2 or Al_2O_3) are also effective in removing metal impurities. Liu et al. reported that ALD Al_2O_3 films generate a strong gettering effect, removing 50% of the iron after 30 min at 425 °C [26]. Surface etching and passivation can reduce nickel-related surface recombination [27].

Presently, the bulk defects or impurities inside c-Si have been well controlled. Surface recombination caused by surface-defect states so far is the dominant form of SRH recombination for all high-efficiency c-Si heterojunction solar cells. The surface state mainly arises from the unsaturated bonds, lattice distortion, defects, and adsorbed impurities, and distributes inside the forbidden band. The surface recombination rate (U) [22,23]:

$$U = \sigma v_T N_s (\Delta n)$$

where σ is carrier capture cross-section, v_T is carrier thermal velocity, N_S is surface density of state. Surface recombination depends on surface recombination velocity ($S = \sigma v_T N_s$) and the density of non-equilibrium carriers. Si solar cells usually have a textured Si surface to reduce the reflectivity, which causes masses of surface traps that lead to a higher surface recombination loss. According to the following equation of lifetime to bulk and surface recombination [29]:

$$\frac{1}{\tau_{eff}} = \frac{1}{\tau_{bulk}} + \frac{S_{eff1} + S_{eff2}}{d}$$

where, τ_{eff} is the effective minority carrier lifetime, τ_{bulk} is the effective carrier lifetime of Si substrate, d is wafer thickness, S_{eff1} and S_{eff2} are the front and rear carrier recombination velocity, respectively. On a high-quality c-Si wafer with a high bulk lifetime, the surface recombination velocity dominates the effective minority carrier lifetime, especially on a thin substrate.

Auger recombination involves three charges (two electrons/one hole or two holes/ one electron). When an electron and a hole are recombined, instead of generating a photon, the released energy transfers to the third charge and then dissipates to the lattice through collisions with phonons. The rate of Auger recombination (R_{aug}) is [23]:

$$R_{aug} = n_e n_h \left(C_e n_e + C_h n_h\right)$$

where C_e and C_h are Auger recombination coefficient of electrons and holes. Auger recombination is most important at high carrier concentrations caused by heavy doping. The more heavily doped the wafer is, the shorter the Auger recombination lifetime. Auger recombina-

tion leads to an unavoidable energy loss in c-Si solar cells based on the doped p-n junction and is especially detrimental with a high doping concentration. This is typically the case in the doped regions of homojunction solar cells, but is also a significant recombination loss mechanism at open-circuit and maximum-power-point conditions in high-efficiency heterojunction solar cells. In the latter, the use of thin and high-quality wafers (< 170 μm) with excellent surface passivation boosts the minority-carrier density well over 10^{15} cm^{-3} at maximum power point operation.

2.3. Parameters of solar cells

The solar cell performances are evaluated by four basic parameters: short-circuit current (I_{SC}), open-circuit voltage (V_{OC}), fill factor (FF), and PCE [22,23], extracted from the illuminated current-voltage (I-V) curve (Fig. 2 (a)) [30]. The I_{SC} is the current passing through a solar cell when the solar cell is in a short-circuited condition. Considering the dependence of junction area, short-circuit current density (J_{SC}) is listed generally ($J_{SC}=I_{SC}$/area). The V_{OC} is the maximum voltage acquired at zero current in a solar cell. FF is defined as the ratio between the maximum power density extractable from the solar cell to the product of J_{SC} and V_{OC}. As the most direct parameter, PCE is defined from the ratio of output energy from solar cells to input energy from the sun.

$$PCE = \frac{P_m}{P_{in}} \times 100\% = V_{oc} \times J_{sc} \times FF \times 100\%$$

where P_m is output energy, P_{in} is input energy (equal to 1000 W/m^2 for the standard-test irradiation AM1.5 G).

The photo-generated current value (I_L) of a solar cell exposed under sunlight is determined by the following equation [22]:

$$I_L = q\int_0^{\infty} N(E)\,QE(E)\,(1-R(E))\,dE$$

where, N(E) is the incident photon flux density, QE(E) is the internal quantum efficiency, R(E) is the reflectance. Low-energy photons cannot be absorbed by semiconductor materials.

When modeling it with an electrical circuit, an ideal solar cell is regarded as a constant-current source in parallel to a diode which models the recombination of photogenerated charges. Hence, subtracted to the photo-generated current I_L, there is a recombination current flowing through the diode known as dark current (I_d) [22]:

$$I_d = I_0(T) \bullet \left(e^{\frac{qV}{nKT}} - 1\right)$$

where n is the ideality factor, K is the Boltzmann's constant, I_0 is the reverse saturation current, T is the temperature. The output current of ideal solar cells can be calculated by the following equation:

$$I = I_L - I_d = I_L - I_0(T) \bullet \left(e^{\frac{qV}{nKT}} - 1\right)$$

Herein, I_{SC} is acquired at V = 0, and V_{OC} is acquired at I = 0. That is,

$$I_{SC} = I_L,\ V_{OC} = \frac{nKT}{q}\ln\left(\frac{I_L}{I_0(T)} + 1\right)$$

According to upper equations, the I_{SC} is directly produced by I_L, and the V_{OC} is influenced by I_L and $I_0(T)$. The V_{OC} results from the separation of the quasi-Fermi energy measured at each contact polarity in equilibrium condition. A high photo-generated charges concentration (large I_L) and a low recombination loss (small $I_0(T)$) increases the split of quasi-Fermi energy, generating a large V_{OC}.

Because of the existence of resistance and non-radiative recombination, the equivalent circuit of a practical solar cell is complicated, as shown in Fig. 2 (b) [31]. The equivalent circuit contains a constant-current source, diode 1 (diffusion current), diode 2 (recombination current), a shunt resistance (R_{SH}), and a series resistance (R_S) [32,33]. Hence, the characteristic between current and voltage meets the following relation [32]:

$$I = I_L - I_{01}\left(e^{\frac{q(V+IR_s)}{n_1KT}} - 1\right) - I_{02}\left(e^{\frac{q(V+IR_s)}{n_2KT}} - 1\right) - \frac{V+IR_s}{R_{sh}}$$

With a determined I_L and I_d, the output quality of solar cells is influenced by R_S and R_{SH}. R_S is mainly caused by contact resistance, collection resistance, and materials resistance; R_{SH} mainly results from leakage and recombination current. As shown in Fig. 3, the effects of R_S and R_{SH} cause a displacement of current-voltage characteristics to a lower voltage and a lower current, respectively. FF reflects these influence, as shown in the following equation [34]:

$$FF = FF_0\left(1 - r_s\right)\left(1 - \frac{1}{r_{sh}}\right)$$

where, FF_0 is ideal FF, r_s and r_{sh} are normalized resistance given by:

$$r_s = R_s/R_{CH},\ r_{sh} = R_{sh}/R_{CH},\ R_{CH} = V_{oc}/J_{sc}$$

Hence, a larger R_{SH} and a lower R_S lead to a larger FF, corresponding to higher output.

2.4. Characterization techniques

Determining the complex relationships among materials, structures, and properties is of great importance to design efficient Si solar cells. Characterization techniques are the prerequisite for analyzing their relationships. Among various common techniques, incident light inten-

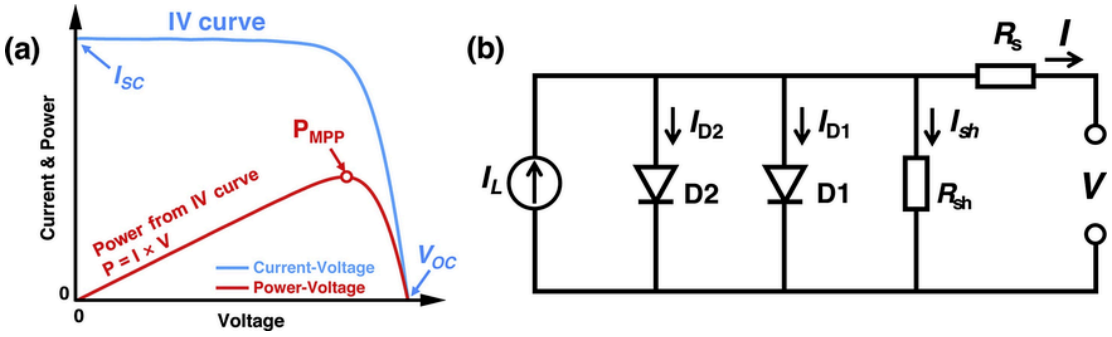

Fig. 2. (a) I-V and power-voltage (P-V) curves of a solar cell. To get the maximum power output of a solar cell, it needs to operate at the maximum power point, P_{MPP}. (b) Equivalent circuit of practical solar cells. I_L is a constant-current source, I_{D1} is diffusion current, I_{D2} is recombination current, R_{SH} is shunt resistance, R_S is series resistance.

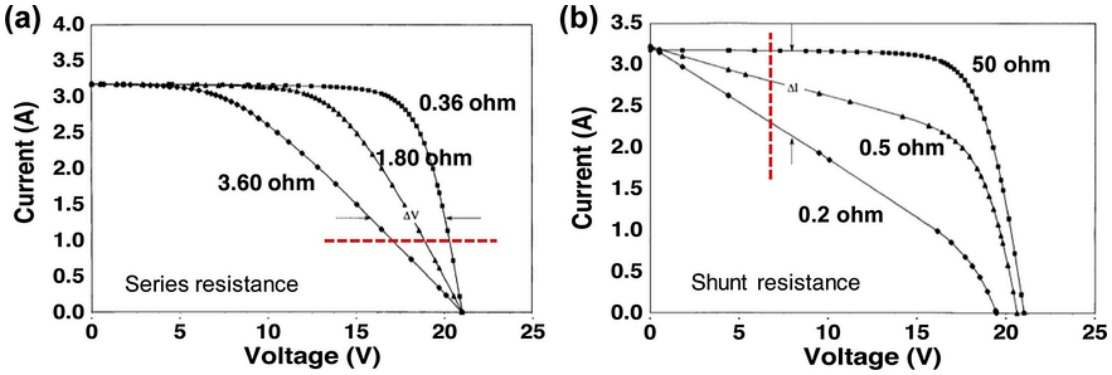

Fig. 3. Current-voltage characteristics of solar cells on different (a) series resistances and (b) shunt resistances. Reprinted with permission from ref. [32]. Copyright 2004, Elsevier.

sity-V_{OC} (*Suns*-V_{OC}), photoconductance decay (PCD) and quasi-steady-state photoconductance (QSSPC) are typical techniques in the field Si solar cells. *Suns*-V_{OC} demonstrates a pseudo-current-voltage characteristic obtained from measuring V_{OC} as a function of illuminated light intensity [35]. Compared with traditional current-voltage characteristics, the pseudo-current-voltage characteristics eliminate the influence of R_S. Importantly, *Suns*-V_{OC} can measure the properties of Si junction, for instance, passivation effect, resistance and τ_{eff}, before made into a practical solar cell, which is facile to guide the design of efficient Si solar cells.

The surface passivation quality is evaluated by the PCD technique by measuring the τ_{eff} [36,37]. Following a pulse generation of carriers in a passivated Si wafer with a flash of light, the decay of the photoconductance is monitored leading to the determination of τ_{eff} according to the corresponded calculation:

$$\tau_{eff} = \frac{\Delta n(t)}{G(t) - d\Delta n(t)/dt}$$

where n is the excess carrier concentration, G(t) is the time-dependent generation rate of excess carriers. The measured lifetime is typically graphed as a function of the excess carrier density n. The transient model is used for higher lifetime samples, where the generation rate G(t) can be ignored. To ensure the validity of this condition, a short flash is used and only the lifetime data following the decay of the flash is used. The QSSPC model is used for lower lifetime samples. Under this condition, the time derivative of the excess carrier concentration is assumed to be negligible. Many useful parameters, such as *implied* V_{OC}, *implied* FF, recombination parameter (J_0), surface recombination velocity (S_{eff}) can be obtained or extracted from τ_{eff} measurement.

Contact resistivity (ρ_c) is a key parameter to evaluate the electrical contact property of heterojunction structures. There are two common methods to measure ρ_c. One method devised by Cox and Strack [38] and another is the transmission line model (TLM) [39]. Fig. 4 (a) shows an example of Cox and Strack method used to measure the ρ_c at MoO_x/p-Si heterojunction [40], where an array of circular Al with different diameters was deposited on MoO_x as front contact and a full-area Al was served as the rear electrode. A series of resistance values can be extracted from dark current-voltage characteristics that are measured between the front and rear electrodes. After that, ρ_c can be determined by fitting the curve of resistance versus front contact electrode diameters. TLM method determines ρ_c by fitting the curve of resistance versus electrode intervals. Fig. 4 (b) shows an example of

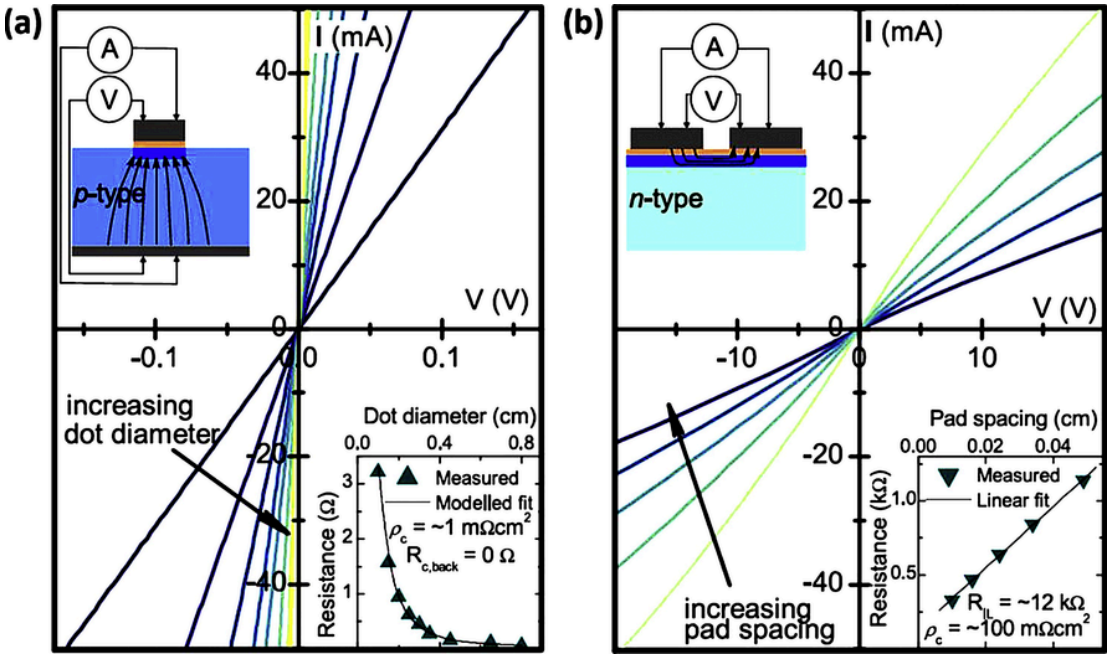

Fig. 4. (a) Cox and Strack method used to measure the contact resistivity of MoO_x/p-Si heterojunction. (b) TLM method used to measure the contact resistivity of MoO_x/n-Si heterojunction. The measurement structures and the fitting process were shown as insets. Reprinted with permission from ref. [40]. Copyright 2014, The American Institute of Physics.

TLM method used to measure the ρ_c at MoO_x/n-Si heterojunction [40], where rectangle electrodes with the same area were deposited on MoO_x with different distance intervals. Resistance values between different electrodes can be calculated from their corresponded current-voltage characteristics, followed by the determination of ρ_c.

As illustrated in Fig. 4, the Cox and Strack method features current flow transport through the carrier-selective contact layer of MoO_3 and Si substrate vertically. On the contrary, current flow transports horizontally through the Si substrate in the TLM method. When highly conductive materials serve as carrier-selective contact layers, the TLM method cannot be conducted to extract ρ_c, because current flow would transport through these highly conductive materials horizontally, instead of Si substrate. Notably, owing to the rectification effect of Schottky junction, Ohmic contact is required between electrodes and Si substrates. Otherwise, it is hard to determine the ρ_c accurately by the traditional Cox and Strack method or TLM method [41]. To resolve this issue, Wang et al. proposed an expanded Cox and Strack model, where the inversion region is formed between the MoO_3 layer and Si substrates [41]. This model guarantees to extract the ρ_c accurately with a wider application range.

3. Si heterojunction solar cells based on doped Si films

3.1. Si heterojunction solar cell based on doped amorphous Si films

3.1.1. Development history: from 13% to 26.7%

Si heterojunction (SHJ) solar cells consist of the happy marriage of c-Si as an absorber layer, with thin-film Si for the selective-contacts of both polarities. This architecture has been known for several decades, yet it has only recently dragged significant attention due to the reaching of record-high efficiency of 26.7% [14,42], and the expiry of key patents from Sanyo (now Panasonic), protecting the technology until a few years ago [43]. The production is still confidential compared to more standard technology based on diffused doped contact (*e.g.* PERC), but it is expected to gain >10% market shares in the next few years, as predicted by the International Technology Roadmap for Photovoltaic (ITRPV) in 2019 (Fig. 5 (a)) [4]. More and more industry players are joining the adventure, both in and outside China. SHJ technology has notably appeared as a possible way to differentiate from mainstream products [44,45]. Compared to these, it typically brings a premium in efficiency that could leverage the presumed higher production cost oftentimes due to relatively small production volumes [46].

The early days of combining a c-Si absorber with a thin-film-Si contact layer occurred half a century ago, with various architectures. In the 1960s and 1970s, heterojunctions consisting of a stack of a Si wafer and a transparent conductive oxide (TCO) started to be studied [48,49]. Regarding the use of amorphous Si, we can consider that Fuhs et al. brought the first stone to this field [50], although the authors themselves mention that "*First experiments of this kind have been performed by the Bucharest group on Junctions between amorphous and crystalline Ge and Si*", making the exact beginning uneasy to set. The SHJ technology as we know it today did not start yet so early, and the closest concepts following directly were using thin-film c-Si. The use of amorphous Si was indeed rather focused towards entirely thin-film PVs devices for the next four decades since thin-film PVs were in the air at that time [51]. Only at the turn of the century did the heterojunction approach, using c-Si as an absorber, started to drag momentum again, notably thanks to the demonstration of over 20%-efficient, large-area devices [52]. Fig. 5 (b) shows the recent progress of efficiency and FF for SHJ solar cells [47]. The efficiency of double-side contacted SHJ solar cells reached 25.1% in 2015, surpassing the champion efficiency of homojunction PREC cell, thanks to the breakthrough of a high FF over 83% [42]. By eliminating the parasitic absorption of a-Si:H layers using interdigitated back-contact (IBC) design, the J_{SC} of SHJ cells was significantly improved, resulting in the world-record efficiency of 26.7% in 2017 [14,42]. We will focus on the status of the technology in 2020, and review the most important key evolutions which occurred recently, which enabled the latest outspread of high-efficiency devices and sustain the industry potential.

3.1.2. Device structure: Si layers and TCOs

Fig. 6 shows the typical fabrication sequence of double-side contacted rear junction SHJ solar cells [10], mainly including chemical processes for texturing and cleaning, intrinsic and doped a-Si deposition by plasma-enhanced chemical vapor deposition (PECVD), TCO deposition by sputtering and metallization by screen printing using a low-temperature silver paste. SHJ device features a symmetrical structure, a thin intrinsic a-Si:H passivation layer is sandwiched between the c-Si wafer and the doped a-Si:H layers; TCOs on both sides for lateral charge transport to the electrodes. The rear junction configuration is the most frequently investigated structure, because a high transparent TCO with less conductivity can be applied at the front side resulting in a higher current density. Furthermore, the hole contact formation in SHJ is often considered to be more delicate compared to the electron contact [47]. SHJ with IBC architecture was implemented to reduce the parasitic absorption in the front TCO and a-Si:H layers, though the high fabrication complexity limits its commercial success. The symmetrical structure of SHJ solar cells makes it very attractive for bifacial design, enabling a high bifaciality factor and high energy yield. Compared to the industrial PERC process, the lean basic SHJ process ensures a shorter production line with less equipment, enabling potential lower capital expenditures (CAPEX) and operational expenditures (OPEX). Moreover, the low-temperature fabrication process (≤ 200 ℃), high bifaciality factor, thinner wafer compatibility, low-temperature coeffi-

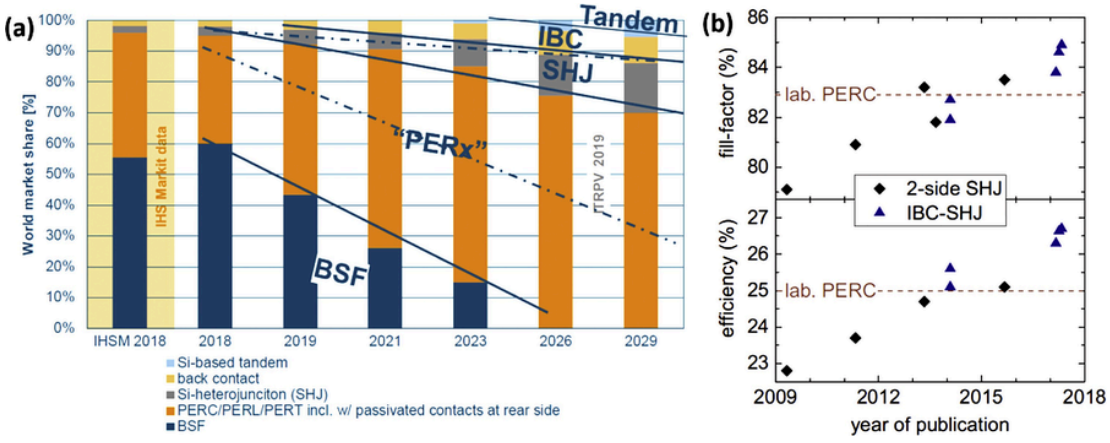

Fig. 5. (a) Future share of c-Si solar cell technologies predicted by ITRPV 2019 [4]. (b) Recent progress of efficiency and FF for SHJ solar cells. Reprinted with permission from ref. [47]. Copyright 2018, Elsevier.

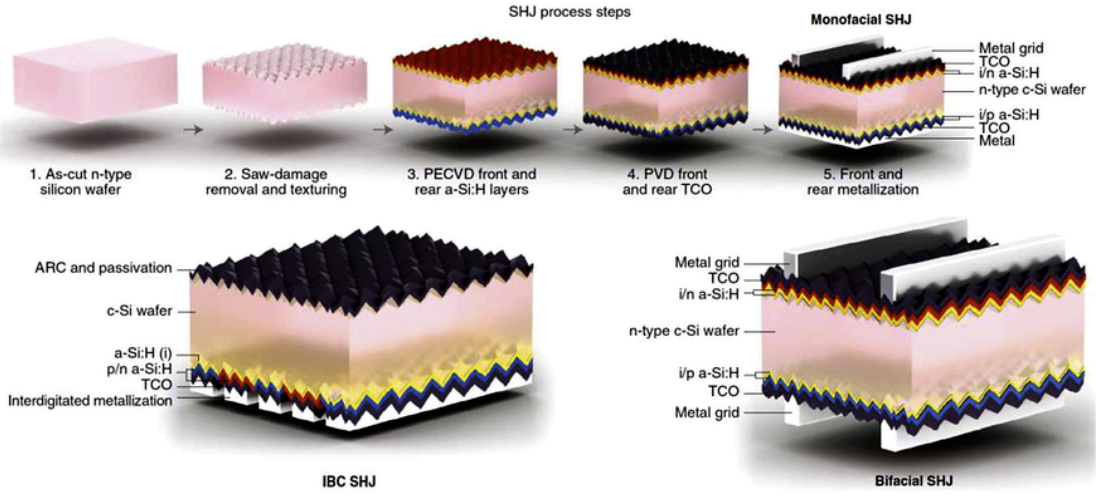

Fig. 6. Fabrication sequence of double-side contacted rear junction SHJ solar cell, as well as the sketches of IBC SHJ and bifacial SHJ solar cells. Reprinted with permission from ref. [10]. Copyright 2019, Springer Nature.

cient and high energy yield make SHJ technology bears the potential to achieve an ultra-low LCOE [47].

SHJ solar cells are at times rightfully referred to as wafer-enhanced amorphous Si solar cells [first coined by Arno Smets]. Indeed, the resemblance between these two devices is striking and a large part of the know-how required to fabricate an efficient SHJ solar cell lies in mastering the fabrication of the thin Si-based layers and transparent electrodes, which is also key to thin-film Si device fabrication [53,54]. The requirements for the layers, however, differ between thin-film Si and Si heterojunction. Sensitivity to impurities is less stringent for surface passivation of the c-Si wafer in the Si heterojunction architecture than for the absorber layer in thin-film Si devices. Light exposure also leads to performance improvement in most relevant cases [55], contrary to thin-film Si [56], although for thin-film Si, light-induced improvements of the contact performance were observed in some cases (typically for thin contact layers) [57].

Concerning the intrinsic a-Si:H passivation layer, antagonist desirable properties are epitaxy-free growth and high hydrogen content. This is typically achieved through a multi-step growth, either by hydrogen-plasma post-growth treatment or by implementing a multi-step strategy, with a relatively hydrogen-poor epitaxy-breaking layer and a hydrogen-rich subsequent layer. Incorporating carbon in the first layer is another way to prevent epitaxial growth [58], as carbon incorporation in amorphous Si leads to increased disorder amongst other properties [59,60]. Such an approach was shown to additionally provide improved temperature stability [59], yet the use of carbon was not reported for the highest-reported-efficiency devices, presuming that these advantages do not balance the increased defectiveness of these alloyed layers. Although the intrinsic amorphous Si layer is providing most of the surface passivation, the quality and thermal stability of this passivation depend largely on the WF of the layer subsequently deposited [61]. In particular, good performance after the deposition of the p-type contact is particularly challenging yet necessary for high-efficiency demonstration. The reaching of a high microstructure ratio (corresponding to a local hydrogen bonding structure favoring multiple hydrogens attached to a single Si atom [62]) in the intrinsic amorphous Si layer is key to that respect [63], which can notably be achieved through the use of a multi-layer scheme [64]. A fine trade-off is overall required for this particularly delicate layer, as exemplified with the reported sensitivity to deposition temperature in high-efficiency devices [65]. Besides alloying with carbon, several attempts to mitigating parasitic absorption in this film through the incorporation of oxygen were made [66,67]. Moderate improvements under specific conditions could be demonstrated, such as high operating temperature, yet it seems again that the highest-efficiency devices use a pure-Si layer for passivation. Recently, Liu et al. demonstrated that the bandgap and surface passivation of a-Si:H passivation layer can be effectively manipulated by tailoring the Si-H bonding state [68]. Hydrogen atoms bonded to internal-void surfaces in a-Si:H can broaden its optical bandgap and improve the surface passivation, resulting in higher performances (Fig. 7).

On the doped-layers side, the demonstration of doping in amorphous Si dates back to the mid-seventies [69]. Although remarkable for an amorphous semiconductor [70], doping is not as efficient as in c-Si, especially for p-type layers, which can impede hole extraction and hence the efficiency of Si solar cells. This effect is particularly observed under low operating temperature, or for high-illumination measurements [71,72]. Transport across the c-Si/a-Si:H interface has been subject to studies for three decades, and is still an active topic of research [73–75]. Better mastering of this aspect probably contributed to the recent progress in reducing series resistance in high-efficiency devices, featuring a high FF over 83% (Fig. 5 (b)). There is however still in 2020 a part of mystery to this, despite the numerous publications studying the influence of the multiple energy barriers at the interfaces between the different materials involved in the structure [76,77]. This triggered a growing interest, especially in the last five years, in doped nanocrystalline Si as a replacement of doped a-Si:H, possibly alloyed with oxygen into a mixed-phase nanocrystalline Si oxide [78–81]. Such layers were shown to be beneficial for both optical and electrical performance in thin-film Si devices a decade ago [82,83].

In general, challenges for implementing nanocrystalline Si layers in heterojunction devices are the demonstration of sufficient doping, and the reaching of fast nucleation without damaging the passivation quality or impeaching current collection [84]. Multi-layers are oftentimes advantageous to obtain thin layers with adequate properties [85]. The use of a pre-deposition treatment was shown to be key for this latter point, either through the use of an oxidizing plasma for p-type layers [86] or through the use of a high-phosphorous-doped seed layer for n-type layers [81]. Fig. 8 shows a typical example of the successful reaching of a highly nanocrystalline p-type layer directly on top of a thin oxidized interface in a Si heterojunction solar cell. Although the nanocrystals are hardly noticeable on the HRTEM image, the diffraction pattern in the fast-Fourrier transformed (FFT) image clearly indicates numerous nanocrystals. Selecting specific diffraction points (colored circles in this image) enables to visualize these grains in space dimension the inversed FFT (iFFT) image. The abrupt nucleation is striking for the red nanocrystal grows directly on top of the oxidized interface. Reducing the deposition temperature compared to the traditional ~200 °C was another key enabler for p-type nanocrystalline Si-

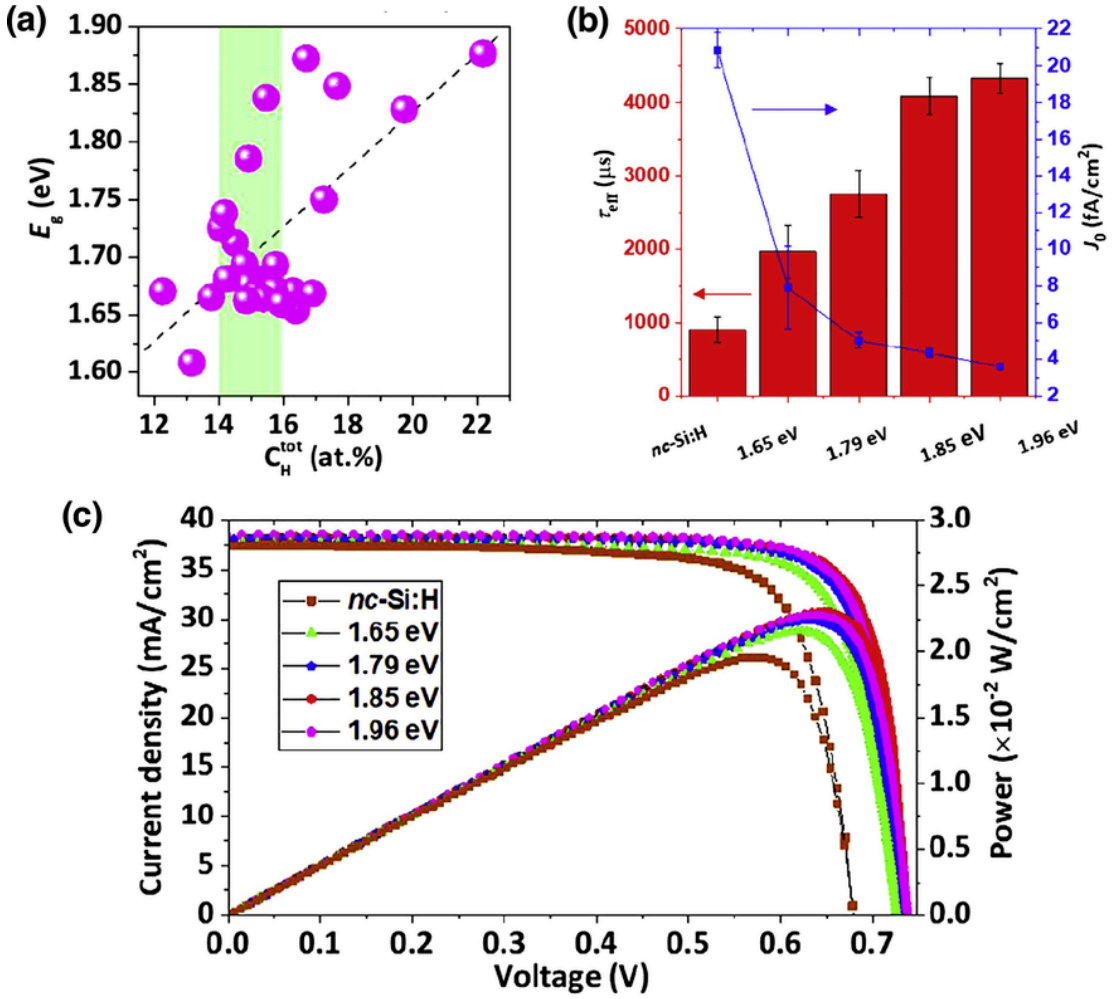

Fig. 7. (a) Bandgap of intrinsic a-Si:H as a function of the total hydrogen concentration, determined by Fourier-transform infrared spectrum. (b) Effective lifetime and saturation current density of n-type Si wafers passivated by a-Si:H layers with different bandgap. (c) Light I-V and P-V curves of SHJ solar cells with front a-Si:H passivation layers featuring different bandgap. E_g: bandgap, τ_{eff}: effective lifetime, J_0: saturation current density. Reprinted with permission from ref. [68]. Copyright 2020, Elsevier.

doped layers to reach similar efficiencies to the ones demonstrated with amorphous Si [80].

3.1.3. *Importance of bulk quality and post-deposition treatments*

In addition to the contact layers, the quality of the bulk of the c-Si absorber is critical, with the highest performance obtained on high-lifetime material [87]. An overview of the performance achievable depending on the material quality can be found in the table reported by Chen et al. [88]. Defects such as thermal donors are typically causing a decrease in minority carrier lifetime, translating in a drop in efficiency [89]. To mitigate the influence of some defects, many strategies are suggested to use low-bulk quality materials while maintaining high performance. These include gettering treatments, as well as annealing in hydrogen atmosphere [87,88,90–95]. Performance improvement can be spectacular, with for example lifetime increase by a factor six, enabling V_{OC} approaching and even surpassing 700 mV with low-initial-quality material. Nowadays, the quality of mass-produced n-type Cz-grown wafers is high enough to not induce penalty compared to float-zone material even at the highest efficiency level; reported efficiencies on p-type material are however lower than on n-type material, making the latter preferable although recent cost analysis suggests that there is a window of opportunity for p-type material use [87].

Concerning surface passivation, performance increase can be obtained through annealing up to approximately 200 °C, although the stability in time of this improvement is questioned [96]. Upon higher-temperature annealing, passivation is progressively lost, setting the temperature limit to the possible processing steps after amorphous Si deposition. On that note, although annealing a wafer passivated with intrinsic amorphous Si at temperatures above 400 °C causes lifetimes to drop from multiple-milliseconds down to a few microseconds, passivation can be, at least partly, recovered through application of hydrogen plasma, indicating that the key properties enabling this amorphous Si network to provide excellent passivation are not affected through these annealing steps [97]. This beneficial effect from a hydrogen plasma is however only effective on intrinsic layers, and cannot be applied on finished devices.

Prolonged light illumination is known to induce metastable defects in amorphous Si, referred to as the Staebler-Wronski effect. A negative effect of light soaking is typically also observed for Si wafer passivation from intrinsic amorphous Si layers only [55,98–100]. This effect was also shown to be beneficial to performance [55], presumably due to passivation improvements although the exact mechanisms are yet to be fully explained. In particular, this light-induced degradation was reported to be dependent on the device architecture, notably the thickness of the p-doped and intrinsic amorphous Si layers [101]. Defect creation in the doped layers, leading to a positive effect on the device performance is suspected to be the main mechanism at stake [102].

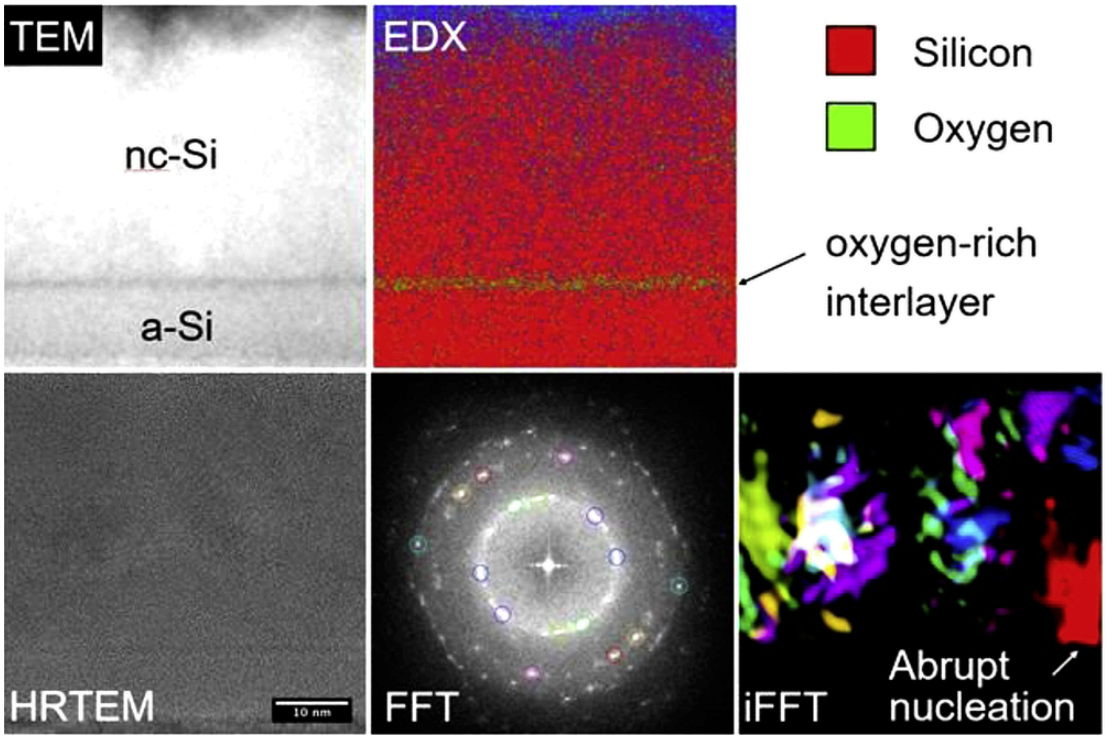

Fig. 8. Microscopy image of a p-type nanocrystalline Si layer grown on top of an amorphous Si layer treated with an oxidizing plasma.

3.1.4. Electrode deposition, metallization and industry perspective

Low-temperature curing paste is required, but recent progress enabled to bridge part of the performance gap compared to traditional high-temperature pastes [103–105]. This includes significantly higher bulk conductivity and reduced finger spreading, enabling thinner fingers. This is advantageous in terms of higher performance as well as a reduced cost since silver paste has been a major cost in this technology. Another key recent innovation is the Smartwire technology, which illustrates how challenges can be turned into opportunities for smarter technology. By enabling a low-cost interconnection with typically 18 wires (corresponding to 18 busbars), the fingers can be made much thinner leading to remarkably low silver usage per wafer [106]. Such creative innovations could apply to many aspects of the Si heterojunction manufacturing, would a sufficient market be here to trigger massive research and development. For example, although capital is required for the deposition reactors for the thin-film Si layers, advantageous reactor designs could be imagined (and were imagined [107]) for lowering their cost while maintaining high film quality. Arguably, this capital-intensiveness is the result of the lack of competition and of the small market, which prevented innovative solutions to be brought in. Multiple strategies are however being studied and could lead to a new paradigm shortly, since the time seems ripe for mass production of Si heterojunction modules [46,108]. Moreover, copper plating has also been investigated as an alternative approach, reducing the expensive silver usage. A possible process to realize directly copper metallization for bifacial SHJ devices has been proposed by Geissbühler et al., demonstrating a low cost potential upon mass production [109,110].

The high cost of the TCO, usually indium tin oxide (ITO) and indium tungsten oxide (IWO) has also been finger pointed as a no-go for SHJ technology. Generally, ITO and IWO are deposited by magnetic sputtering and reactive plasma deposition (RPD), respectively [111]. Replacing indium with alternative materials such as aluminum-doped zinc oxide (AZO) is, therefore, an actively followed route, enabling similar or even improved performance [112,113]. Indium can even be omitted with still remarkable efficiency in two-side contacted devices [114] and IBC solar cells [87,115]. Reducing the thickness of the TCO layer and substituting part of it with a more transparent and less expensive dielectric film is another followed approach. This can lead to high performances both with traditional ITO and with AZO films [114,116,117]. Alternatively, higher-mobility materials compared to ITO are successfully implemented in Si heterojunctions, following the success of hydrogen-doped indium oxide [118,119]. These typically rely similarly on solid-phase crystallization of an amorphous doped indium-oxide film. Amongst the potential dopants, tungsten, zirconium and cerium were reported to enable highly efficient devices [120–122].

The interplay between the electrode and the rest of the device is stringent in Si heterojunction solar cells, and this calls for a holistic approach to fully harvest the potential of this technology. The transparent electrode deposition by reactive sputtering is known to increase recombination in these devices, although this effect is usually reversible upon annealing [123]. Recent studies point out a non-reversible drop of minority-carrier lifetime at low injection conditions. This effect can be caused by a modification of the density of fixed charges at the wafer surface, typically due to the influence of the WF of the transparent electrode [124–126], or the interconnection of local surface defects with a mostly well-passivated area [127]. Another aspect is the lateral transport of charges towards the metal grid. Although the thin-film Si contact layers are not sufficiently conductive to contribute to lateral charge transport – forcing the use of a transparent electrode – the wafer itself can contribute to lateral charge transport, under specific conditions for passivation and contact resistance [128]. Note that highly efficient collection of charges while maintaining excellent surface passivation could be demonstrated as evidenced by the very high-efficiency devices demonstrated by multiple companies including Panasonic, Kaneka and Hanergy [42,129,130].

3.2. Si heterojunction solar cells based on polycrystalline Si on oxide

3.2.1. The development history

In 1947, Bell Laboratories started the race in the semiconductor industry to enhance the performance of Si devices by improving sur-

face electrical stability using dopants and reducing the concentration of defect states with Si oxide (SiO_x) [131,132]. Since then, R&D groups in the industry of semiconductor devices devoted great efforts in optimizing processes and technologies related to passivation of defects by SiO_x and incorporation of dopant species.

These technologies were also the foundation for the development of solar cell devices. The concept of highly-doped poly-Si layer combined with an intentionally grown thin SiO_x layer was discovered in the 1970s and, since then, widely applied in the transistor technology [133]. Over the years, a large amount of experimental and theoretical investigations has disclosed the mechanisms that dominate the device behavior making this approach suitable for many more applications. Kwark et al. developed the so-called semi-insulating poly-Si (SIPOS) hetero-contact demonstrating saturation current reduction [134]. Furthermore, Yablonovitch et al. applied the SIPOS structure in a PV device obtaining a V_{OC} of 720 mV [135]. In the same year, solar cell devices featuring a highly-doped poly-Si confirmed the potential of this approach in the PV field with efficiency close to 12% [136,137].

However, only after more than 20 years, this device concept had a great revival in the PV community. This contact structure is widely referred to as poly-Si carrier-selective passivating contact (CSPC). In 2013 Feldmann et al. introduced, for the first time, the *tunnel oxide passivated contact* (TOPCon) solar cell concept that consists of a mono c-Si wafer with a boron-diffused front emitter and a SiO_x/n-type poly-Si contact stack at the rear side [138]. Shortly after, Römer et al. proposed the so-called polycrystalline-silicon-on-oxide (POLO) architecture with both electrical polarities based on poly-Si CSPCs [139]. Nowadays, several universities, R&D groups and cell manufacturers work on cell concepts endowed with at least one CSPC based on SiO_x/poly-Si stack, such as 'PERPoly' [140], 'monoPoly^{TM}' [141], 'i-TOPCon' [142], and 'poly-poly' [143], among the others. Record efficiencies of 25.8% [144,145] and 26.1% [15] have been achieved in front/back-contacted (FBC) and IBC architectures, respectively.

3.2.2. Poly-Si passivating contact technology development

3.2.2.1. Working principle PV community typically evaluates the quality of CSPC in terms of passivation with recombination parameter J_0 and transport with contact resistivity ρ_c. In this respect, the quality of poly-Si CSPC stands on minimizing J_0 together with ρ_c [146–148].

Poly-Si CSPC adopts two well-established technologies from semiconductor industry: (i) the SiO_x as a passivating layer for c-Si wafer surface [149] and (ii) the doped poly-Si layer to build the electrical field at c-Si wafer interface and to enable the transport of selective carriers [131]. The SiO_x layer chemically passivates the c-Si interface, but it also builds a potential barrier (Fig. 9 (a)) that eventually quenches the flow of collecting charges.

To mitigate the detrimental effect of SiO_x potential barrier on carrier collection, PV community has proposed two approaches for the design of poly-Si CSPCs (Fig. 9 (c) and (d)): (i) tunneling of carriers through the thin SiO_x [150–156] or (ii) breakage of the dielectric film creating the so-called pinholes [157–159]. For tunneling to be the driving transport mechanism in a poly-Si CSPC, carrier collection requires an ultra-thin tunneling SiO_x layer with a thickness below 1.5 nm [160–162]. For the case of thicker (> 2 nm) SiO_x layer, the transport is pinholes-driven, where the thick SiO_x layer eventually breaks/thins during subsequent high-temperature annealing process allowing thus the flow of charge [158,163]. In this case, the trade-off between passivation and collection is related to the total pinhole area [157,164]. In reality, it is worth noting that poly-Si CSPC can feature both mechanisms (*i.e.* tunneling and pin-holes) due to uniformity and specific thermal processes [155,159,165], in a wide range of SiO_x thicknesses.

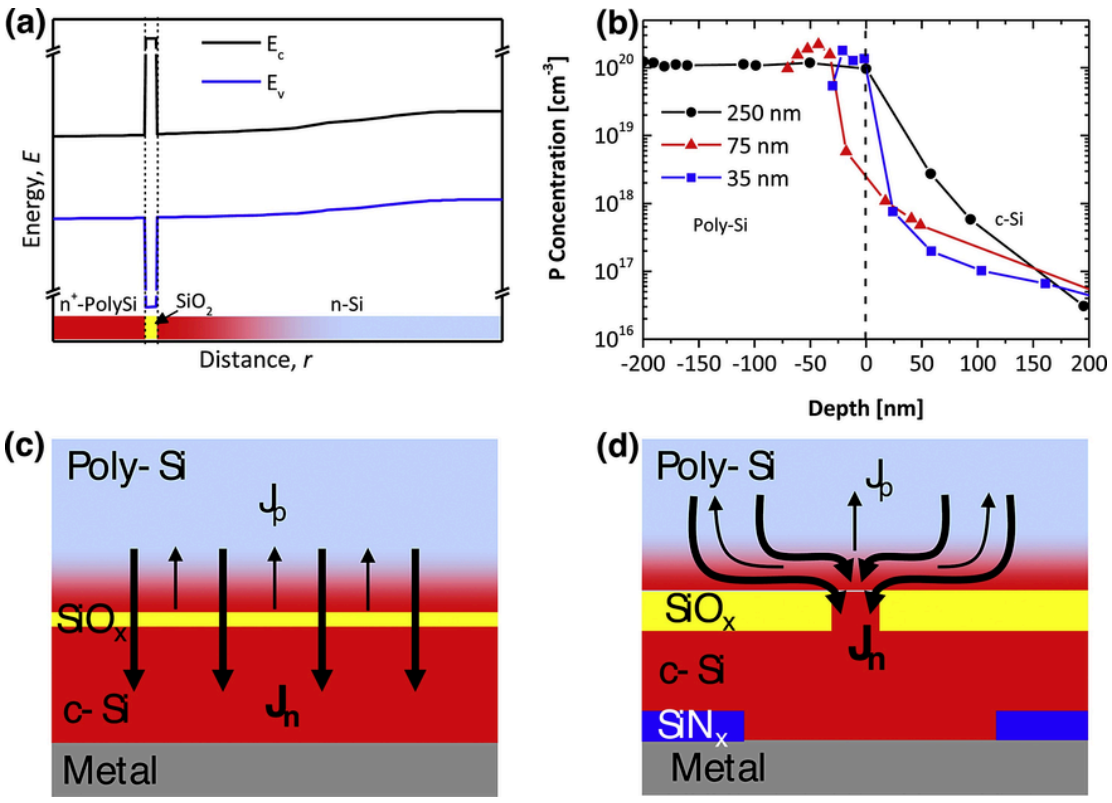

Fig. 9. (a) Schematic band diagram illustrating the potential barriers built by SiO_x passivating layer in case of n-type poly-Si CSPC [160]. (b) Typical phosphorous doping profile for n-type poly-Si CSPC for different poly-Si thicknesses. Reprinted with permission from ref. [143]. Copyright 2020, Wiley-VCH. Note that the doping profile extends also inside the c-Si wafer after thermal treatments. Schematic of charges transport in n-type poly-Si CSPC based on (c) tunneling or (d) pinholes structure. The two sketches summarize the design parameters driving the selective transport by promoting the current of majority carriers (J_n) while quenching the current of minority carriers (J_p). The red-colored fading represents the diffused dopants from the poly-Si into the c-Si bulk.

The doping type of poly-Si layers determines its carrier selectivity. Certainly, to improve the collecting carrier population, such doping levels are typically larger than the effective density of states in conduction and valence band ($> 4 \times 10^{19}\,cm^{-3}$). During thermal processes, the dopant species eventually diffuse through the SiO_x layer into the c-Si wafer thus extending the doping profile into the bulk (Fig. 9 (b)) [157,166]. The presence of the doping profile induces a field effect at the c-Si interface with the CSPC stack, promoting the transport of majority carriers while enhancing the conductivity and electrical passivation [146,147,167]. The doping tail buried inside c-Si must be carefully engineered to allow an efficient carrier separation inside the bulk.

In contrast, such buried doping is unnecessary when the electronic properties of poly-Si CSPC induce an enhanced built-in potential (V_{bi}) inside c-Si. This is the case of wide bandgap hole collector layers [162,168,169], where the integration of carbon or oxygen elements into the poly-Si increases the bandgap of the doped layers [156,168,170,171]. Note that pure poly-Si layers exhibit the same electronic properties as c-Si material (Fig. 9 (a)).

Following the concepts of contact selectivity and selective transport [146–148], it is also crucial to minimize the conductivity of non-collecting carriers. In principle, band-offsets support this effect depending on the energy band structure of hetero-interfaces. In particular, when the collection of carriers is based on tunneling mechanism, non-collecting carriers cannot reach the metal electrode due to potential barriers and minimal carrier population [161,162], For the case of poly-Si material with similar electronic properties as c-Si, the thickness of SiO_x above 1 nm is crucial to prevent non-collecting carriers from reaching the electrode [160]. Therefore, research groups concentrate the study on achieving SiO_x layers within 1 to 1.5 nm alongside buried optimal doping profile in the poly-Si layer and c-Si [166].

If the transport is based on the current flowing through pinholes, the conductivity of non-collecting carriers relies on the asymmetry of carrier populations and the pin-hole area fraction [146,164]. Still, since there is no ideal isolation of non-collecting carriers from the bulk to the electrode, metal fraction needs to be reduced to obtain more efficient contacts [15].

3.2.2.2. Processing The process for manufacturing SiO_x/poly-Si CSPC typically consists of the following steps: (i) SiO_x deposition or growth, (ii) poly-Si deposition with in- or ex-situ doping, (iii) thermal annealing and (iv) hydrogenation.

The key element of this contact is the chemical saturation of dangling bonds present at the c-Si surfaces that provides low recombination for minority carriers [172]. Similarly to the intrinsic a-Si:H, the use of a thin dielectric layer can provide surface passivation while allowing the tunneling of majority charge carriers [173]. The main advantage of SiO_x passivating layer stands on the high thermal stability that enables a wide temperature process window.

In SIPOS-based contact and, later, in poly-Si CSPC technology, the passivation is usually provided by a thermally-grown ultra-thin SiO_x film [173]. Alternative routes are: chemical oxidation in nitric acid [143,154], sulfuric acid [174], hydrogen peroxide solution [175], ozone-based oxidation techniques (UV/O_3 or DI-H_2O) [176], PECVD [177], or ALD oxidation [178]. Extremely low J_0 and ρ_c are obtained independently from the growth method used for the SiO_x [179]. Besides that, oxide layers with a more stoichiometric structure provide a better passivation quality and, therefore, a higher i-V_{OC} [176]. In this respect, chemical oxidation might be less performing due to the slow decomposition of the nitric acid molecule that provides the reactive oxygen species [176]. Furthermore, the layer uniformity and homogeneity depend on the oxidation methods [176], substrate morphology [180], and c-Si orientation [180,181]. More exotic materials suggested for c-Si passivation are calcium oxide (GaO_x) [182], aluminium nitride (AlN) [183], hafnium oxide (HfO_x) [184], *etc*.

On top of the thin oxide layer, a poly-Si film with opportune doping is required to establish the selectivity of one type of carriers. Usually, the Si layer is deposited *via* low-pressure chemical vapor deposition (LPCVD) or PECVD in an initial amorphous state. Recently, alternative depositions have been proposed such as sputtering [185] or hot wire CVD [171]. Often, phosphorous and boron dopants are incorporated *in situ* during the film deposition [186,187] or introduced *ex-situ* by thermal diffusion from a P or B doped silicate glass [188–190] and by implantation (P, B, As, Ga) [15,143,154,191,192]. The subsequent annealing step, performed at a temperature in the range of 800-1000 °C, partially crystallizes the amorphous Si and activates the dopants. The result is a shallow dopant diffusion from the poly-Si through the SiO_x controlled by the annealing time/temperature and doping concentration in the film. The parallel electrode PECVD process has the advantage of decoupling front/back deposition, allowing for more flexibility and possibly leaner flowcharts than LPCVD. While for PECVD is possible to obtain front and rear layers with different thicknesses, in case of LPCVD the growth happens simultaneously on both sides of the substrate. Conversely, PECVD layers might be prone to form blisters due to the initial hydrogen content and the effusion of H_2 and/or H_2O during annealing. This shortcoming can result in severe degradation of performances [186]. To avoid blistering, incorporation of a small amount of carbon has been found to enhance stability [193,194]. Finally, the hydrogenation treatment consists of annealing in forming gas at relatively low temperature (400-450 °C), usually in the presence of a hydrogen-rich capping layer (SiN_x or AlO_x) [195] or in remote hydrogen plasma [196].

To improve the optoelectrical properties of poly-Si based layers, some R&D groups proposed to alloy them with oxygen [170,197] or carbon [156,198] that can be incorporated in the a-Si film. The final material consists of a poly-Si film with an alloyed amorphous fraction. Nevertheless, deep optical characterization showed that this approach leads to increased parasitic losses upon annealing in the short wavelength region, but decreased losses in the infrared wavelength region due to the lowered free carrier absorption [199]. Recently the use of nitrogen-doped Si carbide deposited *via* hot wire CVD has been successfully applied in device with demonstrated improved transparency [200]. This approach is very promising because it does not require any post-deposition treatment [201]. On the other hand, the use of Si carbide (SiC_x) films fabricated with industrial tools, like tube furnace, is challenging due to the difficulties to sufficiently dope the material or recover the implantation damages [202].

3.2.3. Towards high-efficiency Si solar cells

Poly-Si CSPCs enable high efficiency in a wide variety of solar cell structures. Depending on the way of combining the poly-Si CSPC in a solar cell device, as shown in Fig. 10, the cells can be classified into four groups, including PERC-like poly-Si FBC, poly-poly FBC, poly-finger FBC and poly-Si IBC. Besides, all the architectures depicted in Fig. 10 are extended to bi-facial approach to further enhance their output power [142,203,204].

Fig. 11 shows an overview of conversion efficiency evolution for the abovementioned poly-Si CSPC structures developed worldwide by different universities and R&D groups, featuring a rapid increase in performance with about $1\%_{abs}$/year achieving over 26%. In the following, the features of each architecture will be described.

3.2.3.1. PERC-like poly FBC solar cells In PERC-like poly-Si FBC cell, the rear contact is replaced by a poly-Si CSPC while the front side contact can be either homo-junction [213,215,218,223,228,232] or a low-temperature CSPC (such as SHJ [168,233] or TMOs [234]). Here we discuss the case of TOPCon cell as an example. The advantage of PERC-like poly FBC solar cells compared to PERC cells stands on minimizing recombination losses at the rear side by avoiding direct Si-metal contact (Fig. 12). Moreover, comparing to the PERC cell, the TOPCon cell structure has a simpler device design which enables a mono-dimensional (1-D) current flow in the c-Si absorber that avoids FF losses originated from a 3-D carrier transport in the PERC cell structure (Fig. 12) [210].

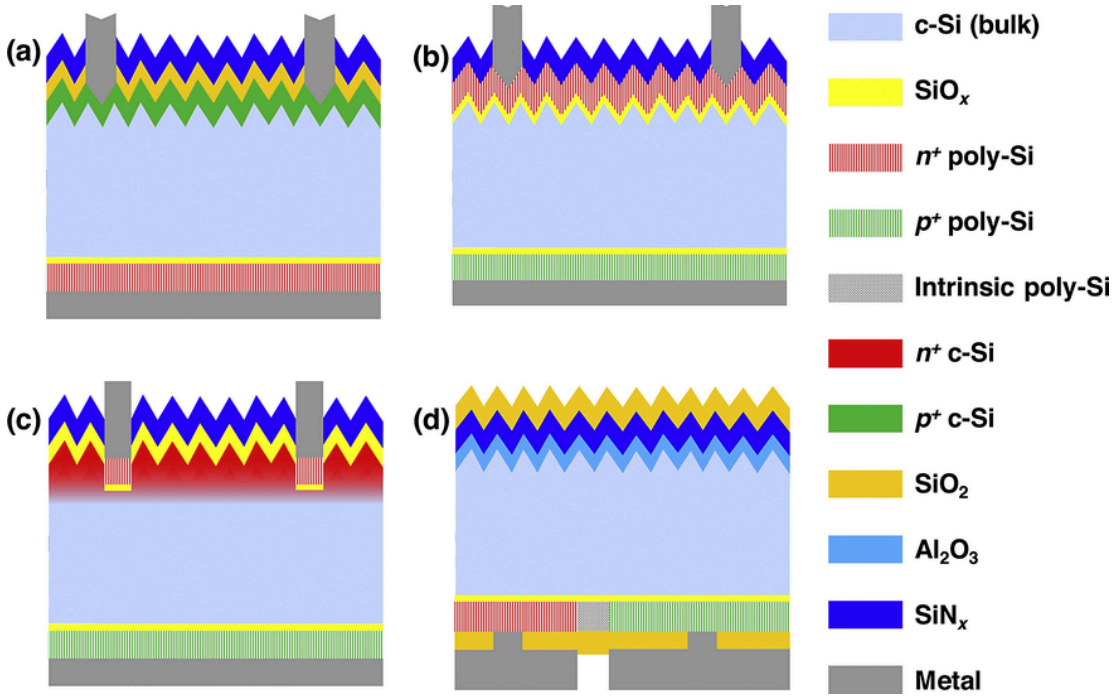

Fig. 10. Sketch examples of solar cells that deploy poly-Si CSPC structure. (a) one polarization PERC-like poly FBC [138], (b) two polarizations on full area poly-poly FBC [143], (c) localized poly-Si contact poly-finger FBC [205], and (d) interdigitated back contacted solar cells poly-Si IBC [15].

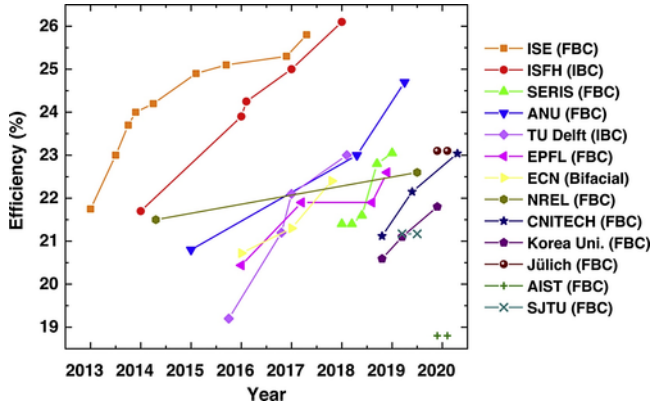

Fig. 11. The conversion efficiency evolution poly-Si CSPC solar cells from R&D groups: Fraunhofer Institute for Solar Energy Systems (ISE) in Germany, Institute for Solar Energy Research in Hamelin (ISFH) in Germany, Solar Energy Research Institute of Singapore (SERIS), Australian National University (ANU), Delft University of Technology (TU Delft) in the Netherlands, École Polytechnique Fédérale de Lausanne (EPFL) in Switzerland, Energy Research Centre of the Netherlands as part of Netherlands Organisation for Applied Scientific Research (ECN.TNO), National Renewable Energy Laboratory (NREL) in America, Ningbo Institute of Industrial Technology (CNITECH) in China, Korea University (Korea Uni.), Forschungszentrum Jülich (Jülich) in Germany, Advanced Industrial Science and Technology (AIST) in Japan, Shanghai Jiao Tong University (SJTU) in China. Data were from references [15,138,141,144,152–155,160,166,175–177,191,192,195,203,204,206–231].

Besides the quality of the front side homo-junction structure, the factors that influence the performance of this cell architecture are the (i) passivation quality of the rear poly-Si CSPC, (ii) the efficiency of carrier selective collection by the poly-Si alloy contacts, and (iii) the influence of the metal contact formation. Optoelectrical simulations on this cell structure predict a theoretical PCE above 28% [235]. Since the development of poly-Si alloys CSPC, their application in solar cell enables a continuous increase of cell efficiencies, with the best efficiency reaching 25.8% [144,145].

3.2.3.2. Poly-poly FBC solar cells Poly-poly FBC devices feature poly-Si CSPCs on both polarities [143,236,237]. From the solar cell process point of view, the most simplified approach to deploy the poly-Si CSPCs in the c-Si solar cell is the poly-poly FBC device, as shown in Fig. 10 (b). In this cell structure, the poly-Si contacts are applied on both sides as hole and electron selective contacts. On the other hand, the heavily doped poly-Si CSPC exhibits a high parasitic absorption which increases optical losses. Recent material and device characterizations reveal the corresponding optical properties of poly-Si alloys materials and their influence on the cell performances [170,199,238,239], as shown in Fig. 13 of the calculated absorptance of poly-Si layers with different thicknesses when used at the front and rear of the c-Si solar cell and their corresponding photocurrent losses [143].

To minimize the parasitic optical absorption, a possible approach is to thin the poly-Si CSPC layers on the front side. However, the sheet resistance of this layer will increase, resulting in enhanced resistive losses (*i.e.* lower FF). On one hand, to compensate for such loss, the TCO is normally used on top of the thin poly-Si alloy contact to facilitate current collection. On the other hand, the WF of the TCO layer needs to be carefully chosen for n-type or p-type poly-Si alloy contacts. A large WF mismatch between TCO and the poly-Si alloy layers might lead to a significant Schottky barrier, which can limit the FF of the device [237,240]. To minimize this barrier, interlayer(s) between TCO and the poly-Si alloy can be placed. In principle, a low WF TCO for n-type poly-Si alloy and a high WF TCO for the p-type poly-Si alloy are required for obtaining a high FF [237]. Even though sputter deposition of TCO harms the passivation quality of poly-Si CSPCs, post-TCO-deposition treatment, such as annealing in different atmospheres, could recover (or partly) the passivation quality degradation due to the sputtering damage [241]. Some research groups proposed to use a pre-diffused c-Si surface before the poly-Si deposition, aiming at minimizing the series resistance by promoting the current flow within the high conductive pre-diffused region [242]. However, the FF improvement is still limited [242,243].

3.2.3.3. Poly-finger FBC solar cells To solve the abovementioned optical issue raised by the front poly-Si layers, researchers have recently proposed to apply the poly-Si CSPC only underneath the metal fingers,

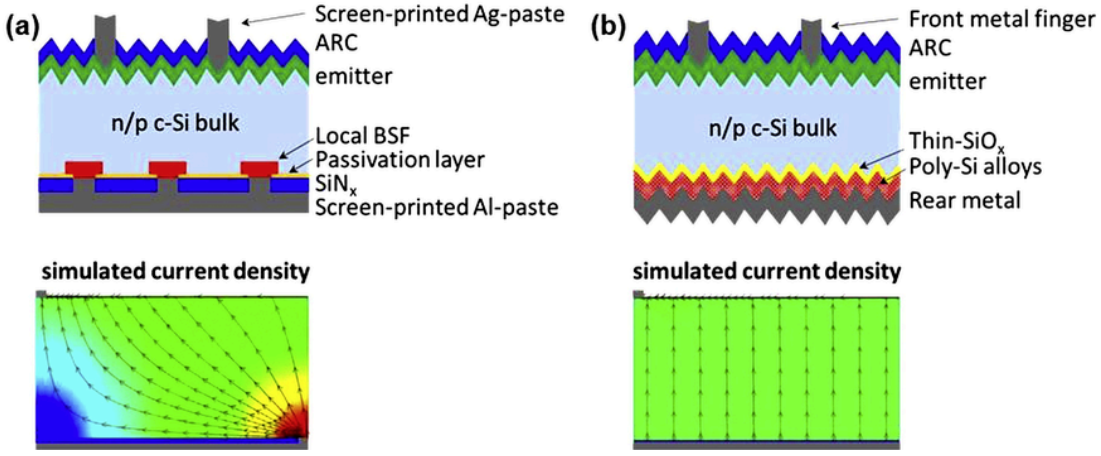

Fig. 12. The sketch of (a) PERC cell structure and (b) PERC-like poly FBC (n-TOPCon cell) with the corresponding simulated current density contour plots. Reprinted with permission from ref. [210]. Copyright 2014, Elsevier.

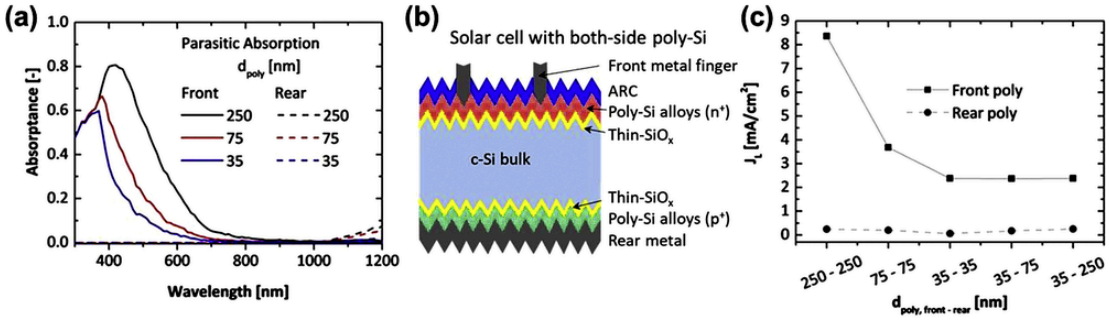

Fig. 13. (a) Simulated absorption spectra of n-type poly-Si layers with different thicknesses on the front (continuous line) and rear (dashed line) sides used in (b) poly-poly FBC cell. (c) Simulated equivalent photocurrent density losses related to different front and rear poly-Si layer thickness combinations. Reprinted with permission from ref. [143]. Copyright 2020, Wiley-VCH.

as depicted in Fig. 10 (c). This approach was in principle called PeR-FeCT (Passivated Rear and Front ConTacts) solar cell architecture when it was proposed for the first time [205]. In this cell structure, the metal contact grid shades the poly-Si CSPC layer away from light illumination. Therefore, the application of the poly-Si CSPC fingers does not contribute to any optical parasitic absorption, while maintaining the lowest possible J_0. This architecture is already under research at TU Delft, ANU, and ISE, with potential efficiency above 26% [204,244,245].

3.2.3.4. Poly-Si IBC solar cells Concerning solar cell architectures, the IBC concept stands out as the main option to demonstrate remarkable efficiencies owing to the absence of front shading contact (Fig. 10 (d)) [15,222,246–249]. Therefore, by combining the optical advantage of IBC structures together with the electrical advantages of the poly-Si CSPCs, a remarkable efficiency above 26% has already been demonstrated [15], as summarized in Fig. 11. Efficiency calculations reveal a practical limit above 27% by tuning thin-SiO_x thickness, pitch size, emitter-to-BSF ratio, and the separation between the BSF and emitter fingers [160,209].

3.2.4. Commercialization challenges

As described above, poly-Si CSPCs enable very high efficiencies at lab scale with different cell architectures, demonstrating the potential for industrial up-taking. However, the question is how to integrate this technology into industrial processes. Among compatible solar cell architectures, PERC-based FBC and IBC are the most promising for upgrading to poly-Si CSPC technology.

Independently from which cell structure will be industrially exploited, one of the main challenges is the metallization step. For example, the lab-scale 25.8% efficient TOPCon cell presents physical vapor deposited (PVD) Ti/Pd/Ag followed by plating of Ag fingers and full-area PVD Ag for front and rear metallization, respectively [149]. Further, also the *POLO-junction IBC* cell exhibiting 26.1% efficiency features PVD metallization process. The industrialization of these technologies requires high-throughput low-cost metallization processes. For these reasons, screen printing is a commonly used technology in the PV industry. The fire-through type of metal paste is one of the most used for screen printing metallization, which leads to a simple and low-cost process. However, when it is used for contacting poly-Si CSPCs, the settings for screen-printing and firing step are similar to those used for homo-junction c-Si solar cells but need further optimization [250]. These adjustments aim at maintaining the thermal stability of the poly-Si CSPCs while preventing the metal paste from penetrating c-Si bulk through the poly-Si layers [250]. Fire-through Ag/Al and Ag pastes are commonly used [250–253]. Other options are (i) single firing thermal annealing combining dielectric-driven hydrogenation and metallization [168] and (ii) low-temperature Ag pastes mostly alongside TCO for contacting [241,254,255]. Besides these approaches, to commercialize these new technologies, R&D groups are developing other metallization approaches employing laser ablation and electrical plating [15,256,257].

Nowadays, PERC technology dominates the PV market with very high efficiency already achieved. However, its manufacturing process is still complex due to the patterning steps to minimize the contact fraction between metal and Si, aiming to reduce the recombination losses at the contact regions. Several studies evaluated the feasibility of upgrading PERC cell structure with poly-Si CSPCs with both n-type and p-type c-Si as bulk materials [258]. Besides the abovementioned metallization challenges, the upgrades in the current PERC production lines to accommodate for poly-Si technology require extra equipment invest-

ments for the preparation of poly-Si CSPCs. For instance, a set of thermal oxidation furnaces or wet chemical oxidation setups are needed for the preparation of the ultra-thin SiO_x layer; and PECVD or LPCVD equipment is required for the deposition of poly-Si alloy layers, doping and thermal treatments. Efforts from R&D groups and PV industry have made the large-area cell efficiency to go above 23% with the TOPCon cell structure from JinkoSolar [259], i-TOPCon from Trina [142], monoPoly™ cell from SERIS [141], and PERPoly cell from ECN.TNO [260] among others. Currently, most of the abovementioned industry developments are on n-type mono-Si bulk. However, developments on n-type or p-type cast mono-Si as bulk material have also lead to record high efficiencies for industrial solar cells [261,262]. An overview of the research institutes and PV industries that produce large-area (> 100 cm^2) solar cells based on poly-Si CSCs is summarized in Table 1.

Considering the high absorptance of poly-Si CSPCs when used at the front side of the solar cells, and the complexity of processing cells with poly-Si finger cells, IBC solar cell architecture with poly-Si alloy CSPCs is one of the main approaches for industrializing this technology [15,270], as already shown by company Trina with their *poly-IBC* cell [269]. However, the main challenges are the patterning of p^+ and n^+ poly-Si fingers and the subsequent metallization with the industrial tools. The patterning of poly-Si fingers can be done by a few steps of wet/dry etching with dielectric coatings as masking layers, or by selectively ion-implanting B or P for p^+ or n^+ poly-Si doping, respectively [222,271]. The first approach is complex for industrialization, while the latter one is simple and was demonstrated in the PV industry by Trina with large area record cell efficiency around 25% [269]. Compared to the FBC cell case, besides the challenge in deploying the right paste and metallization recipe for contacting poly-Si materials, the metallization for IBC cells is *per se* more complicated, as extra attention is needed on the alignment of the screen-printed metal fingers with the poly-Si fingers. Special processes, like laser ablation for opening the dielectric layers followed by screen-printing, are now under investigation for possible industrialization [15].

4. Novel concept Si heterojunction solar cells

4.1. Si/metal compound heterojunction solar cells

4.1.1. Development status

Although the doped Si film based heterojunctions solar cells have achieved remarkable success, the parasitic absorption from either intrinsic or doped Si film limits the PCE of the devices. Hence, the ultra-high efficiency devices with either SHJ or TOPCon technology utilize the complex IBC design, to minimize the parasitic absorption losses from Si layers [15,272]. Moreover, the Si-based films were deposited by either PECVD or LPCVD, which are capital-intensive techniques with mandatory safety systems because of the use of pyrophoric silane and toxic boron/phosphorous gas precursors.

To overcome these demerits, alternative dopant-free, carrier-selective contact materials (DFCSC) based on wide bandgap metal compounds are intensively investigated by the PV community. These contact materials exhibit a simultaneous combination of optimal transparency, surface passivation and carrier selectivity, which can be deposited easily, economically, and safely with minimal hazardous risks. Metal compounds with an extremely low or high WF and/or a suitable band alignment with Si are considered to be potential DFCSC materials. In principle, wide bandgap materials featuring a small E_C offset (ΔE_C) with Si or a low WF (typically WF $< E_{C,\,Si}$ of ~ 4.1 eV) can be developed as the electron-selective contacts (ESCs). Accordingly, materials with a high WF (typically WF $> E_{v,\,Si}$ of ~ 5.2 eV,) or a small E_V offset (ΔE_V) with Si can be a hole-selective contact (HSC) candidate. Fig. 14 shows the band alignment of carrier-selective contact materials with Si, including both Si-based and metal compound based passivating contacts [10]. In principle, these metal compounds based passivating contacts mainly consist of metal oxides, alkali/alkaline metals and salts, and transition metal nitrides (not shown in Fig. 14), which can be deposited using simple techniques, such as PVD (thermal evaporation, sputtering, e-beam), solution-based processing (spin-coating) and ALD. Table 2 listed all the key parameters of the metal compound based passivating contacts by far, as well as the device configuration and performance. Full-area contact design of the DFCSC is the most attractive route, considering the fabrication complexity and cost. It can be seen that the titanium oxide (TiO_x) based ESC and the MoO_x based HSC are the most successful examples, achieving the best PCE of 22.1% and 23.5% with a full-area contact design, respectively [18,273]. More interestingly, a state-of-the-art PCE of 21.4% was achieved on c-Si solar cells with double-side dopant-free passivating contacts, employing a front hole-selective MoO_x contact and a rear electron-selective zinc oxide (ZnO)/ lithium fluoride (LiF)/Al contact [274]. All these achievements demonstrate the high potential of DFCSCs for high-efficiency, low-cost c-Si solar cells. We will discuss the development status and details by dividing them into two types based on their carrier selectivity, *i.e.* ESCs and HSCs.

4.1.2. Electron-selective contact materials and devices

The transition metal oxides based ESCs are most widely investigated, mainly including TiO_x [273,275–277], magnesium oxide (MgO_x) [278,279], tantalum oxide (TaO_x) [280], ZnO [274], and niobium oxide (NbO_x) [281]. Among them the most successful ESC

Table 1
Efficiencies achieved on large-area solar cells with poly-Si CSPC from the research institutes and PV industry.

R&D Institute and PV industry	Area (cm^2)	Cell structure	Poly-Si contact	Metallization approach	Efficiency (%)	Reference
ISE	100	FBC	n^+ (rear)	PVD-Ti/Pd/Ag	24.5	[263]
ISFH/HZB	244	FBC	n^+ and p^+	TCO/SP-Ag	21.7	[264]
CSEM/EPFL	245	FBC	p^+ (rear)	ITO/Ag	22.5	[213]
SERIS	244	FBC (bifacial)	n^+ (rear)	FT-SP	23.1	[219]
ECN.TNO	244	FBC (bifacial)	n^+ (rear)	FT-SP-Ag	22.4	[260]
CNITECH	244	FBC	n^+ (rear)	FT-SP	21.4	[265]
Julich	244	FBC	n^+ (front)	ITO/Ag	23.1	[266]
SJTU	244	FBC (bifacial)	n^+ (rear)	SP	21.2	[267]
Jolywood (R&D)	244	FBC (bifacial)	n^+ (rear)	SP	23.3	[268]
Jolywood (Production)	244	FBC (bifacial)	n^+ (rear)	SP	22.66	[268]
TrinaSolar	244	FBC	n^+ (rear)	SP-Ag	24.6	[142]
Jinko Solar	244	FBC	n^+ (rear)	/	24.2	[259]
Canadian Solar[a]	246	FBC	/	/	23.8	[261]
Canadian Solar[b]	246	FBC	/	/	22.8	[262]
TrinaSolar	243.2	IBC	n^+	/	25	[269]

[a] n-type cast mono Si bulk.
[b] p-type cast mono Si bulk.

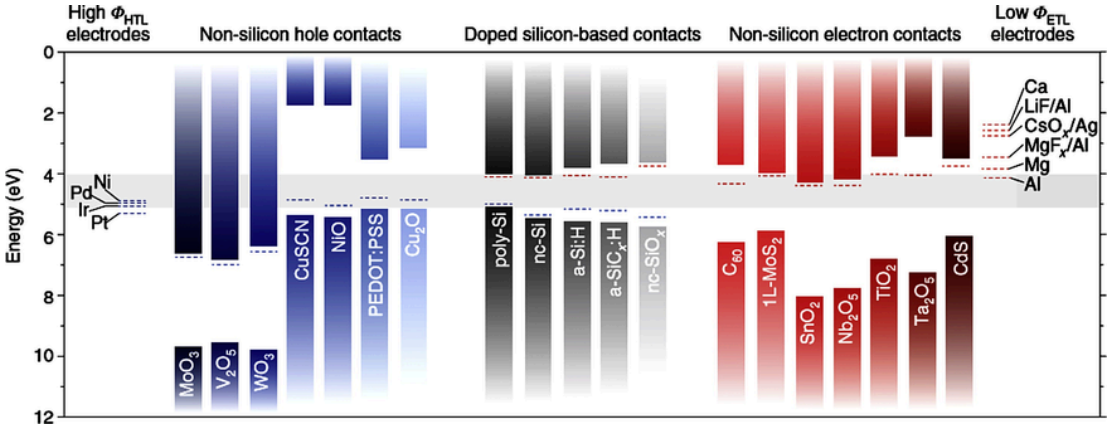

Fig. 14. Passivating contacts materials for c-Si solar cells. Conduction and valence band positions (upper and lower rectangles, respectively), and indicative Fermi level positions (dashed lines) of various metals, metal compounds and organic semiconductors, with ESCs in red and HSCs in blue. The band edges of c-Si are shown as a grey bar for reference. Reprinted with permission from ref. [10]. Copyright 2019, Springer Nature.

Table 2
Key parameters of metal compounds based passivating contacts, and the device configuration and performance.

Material	Type	Contact Structure	Thickness (nm)	ρ_c (mΩ•cm^2)	Device configuration[a]	Best PCE (%)	Reference
TiO_x	ESC	TiO_x	4.5	40	p^+/n-Si/TiO_2/Al	19.8	[275]
		SiO_2/TiO_x	1.5/3.0	63	p^+/n-Si/SiO_2/TiO_2/Al	22.1	[273]
		a-Si:H/TiO_x/LiF	5.0/1.5/0.6	4	MoO_x/i/n-Si/ i/TiO_x/LiF/Al	20.7	[294]
		a-Si:H/TiO_x/Yb	8.0/1.0/40	1	ip/n-Si/i/TiO_x/Yb/Ag	19.2	[289]
		TiO_x/LiF	1.5/1.0	5	Rear point contact	23.1	[287]
		TiO_x/Ca	3.5/30	5	Rear point contact	21.8	[288]
MgO	ESC	MgO	1.0	18	p^+/n-Si/MgO/Al	20.0	[278]
		a-Si:H/MgO	5.0/3.5	950	ip/n-Si/i/MgO/Al	16.8	[279]
TaO_x	ESC	TaO_x/Mg	6.0/10	350	p^+/n-Si/TaO_x/Mg/Ag	19.1	[280]
ZnO	ESC	a-Si:H/ZnO/LiF	7.0/75/1.5	136	MoO_x/i/n-Si/ i/ZnO/LiF/Al	21.4	[274]
LiF	ESC	LiF	1.0	1	Rear point contact	20.6	[295]
		a-Si:H/LiF	5.0/1.0	7	MoO_x/i/n-Si/i//LiF/Al	19.4	[293]
MgF_2	ESC	a-Si:H/MgF_2	6.5/1.0	76	p^+/n-Si/i/MgF_2/Al	20.1	[296]
Mg	ESC	a-Si:H/Mg	6.0/10	310	p^+/n-Si/i/Mg/Al	19.0	[298]
		SiO_2/Mg	1.8/20	26	n-Si/SiO_2/Mg/Al	15.0	[299]
TaN_x	ESC	TaN_x	2.5	53	p^+/n-Si/TaN_x/Al	20.1	[302]
TiN	ESC	SiO_2/TiN	1.7/300	16.4	p^+/n-Si/SiO_2/TiN	20	[303]
MoO_x	HSC	a-Si:H/MoO_x	5.0/4.0	200 ± 100[b]	MoO_x/i/n-Si/in/ITO/Ag	23.5	[18]
		MoO_x	15.0	60	Rear point contact	20.4	[323]
VO_x	HSC	VO_x/Ni	40/5.0	115	IBC	19.7	[311]
		a-Si:H/VO_x	5.0/4.5	95	in/n-Si/i/VO_x/Ag	21.6	[319]
CrO_x	HSC	CrO_x	4.0	45	Partial rear contact	20.2	[320]
PEDOT:PSS	HSC	SiO_2/PEDOT:PSS	1.5/140	100	n^+/n-Si/SiO_2/PEODT:PSS/Ag	20.6	[324]

[a] p^+: boron-diffused p^+ emitter; i: intrinsic a-Si:H; ip: intrinsic a-Si:H/p-type a-Si:H stack; in: intrinsic a-Si:H/n-type a-Si:H stack; IBC: interdigitated back-contact.
[b] Data obtained through personal discussion with Dr. Mathieu Boccard, EPFL.

is TiO_x, featuring a very small ΔE_C (~ 0.05 eV) and a large ΔE_V (~ 2 eV) with Si [275], resulting decent electron-selective, hole-blocking property of Si/TiO_x heterojunction. Thin TiO_x was also demonstrated to provide excellent surface passivation on c-Si surface, probably due to a negative charge in TiO_x and the formation of Si-O-Ti covalent bonding at the Si/TiO_x interface [282,283]. TiO_x deposited by a modified CVD process was firstly implemented on the front side of *p*-Si solar cells for electron collection, achieving a low efficiency of 7.1%, limited by the high carrier recombination at both sides and poor lateral conductivity of TiO_x [277]. By shifting the TiO_x contact to the rear side of n-Si solar cells together with a front PEDOT:PSS for hole collection, the PCE was significantly enhanced to 13.9% [284]. The breakthrough of TiO_x contact was realized by Yang et al., who developed the ALD deposited TiO_x-based contact, achieving excellent surface passivation and a low contact resistivity simultaneously [275]. A low effective surface recombination velocity of 11 cm/s, equivalent to a J_0 of ~ 20 fA/cm^2, was obtained on n-Si passivated by 5.5 nm ALD TiO_x [275]. More importantly, n-Si/TiO_x/Al hetero-contact with a thin TiO_x interlayer (2.5 ~ 5.5 nm) exhibited a low contact resistivity (ρ_c < 0.1 Ω•cm^2) after forming gas annealing, which is below the threshold of a full-area contact for high efficiency c-Si solar cells [147]. The PCE was further improved to 19.8% on n-Si solar cells, featuring a full-area single-layer TiO_x rear contact and a conventional boron-diffused p^+ emitter at the front. However, the PCE is much lower than expected, based on the J_0 and ρ_c of TiO_x contact, which can be attributed to the electron selectivity degradation of TiO_x after Al metallization. The degradation was ascribed to the undesired reaction between TiO_x and Al [275]. A tunnel oxide (SiO_2) passivation interlayer was innovatively inserted between n-Si and TiO_x, which further boosted the PCE to 22.1% (Fig. 15a) [273,275]. The electron selectivity of Si/SiO_2/TiO_x heterojunction was proven to keep at a high quality after Al metallization. However,

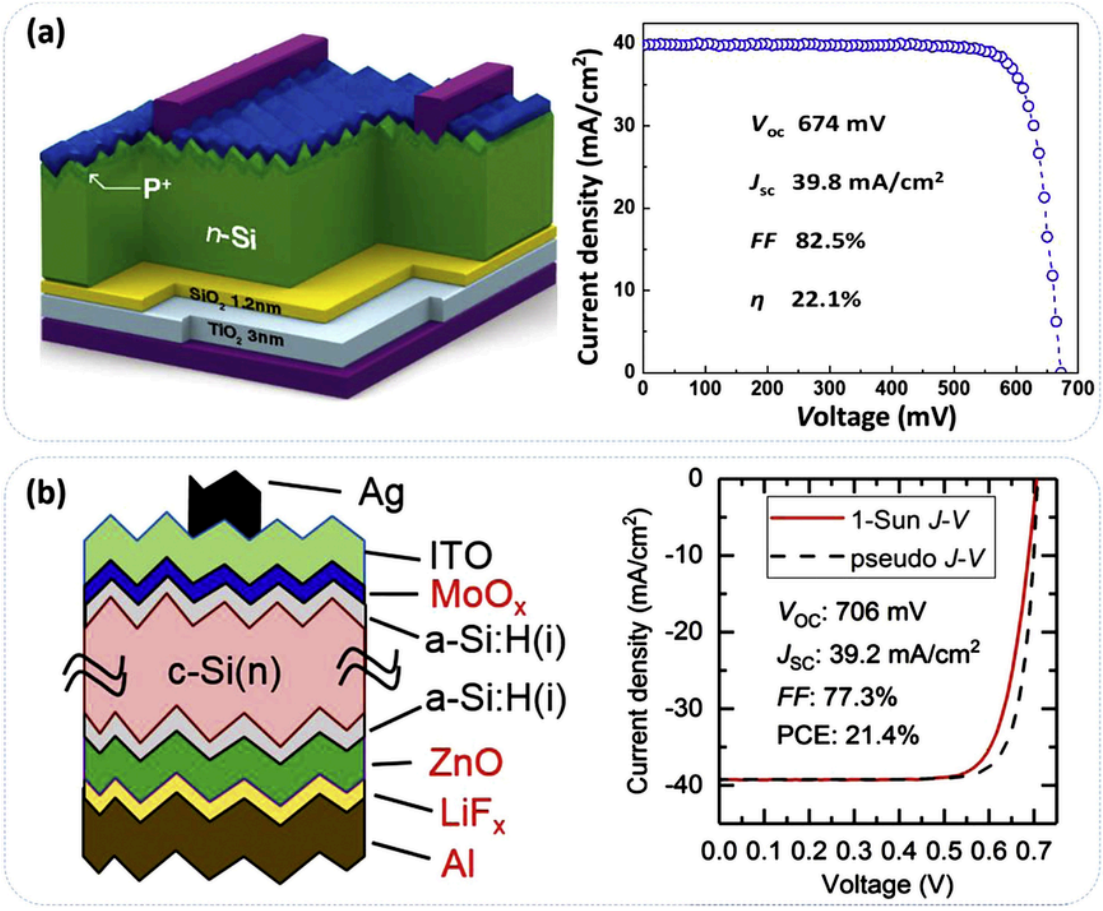

Fig. 15. (a) The sketch of c-Si solar cells featuring a full-area TiO_x-based ESC, and the illuminated J-V curve of the best device. Reprinted with permission from ref. [273]. Copyright 2017, Wiley-VCH. (b) Schematic of a solar cell with dopant-free hole-selective MoO_x and electron-selective $ZnO/LiF_x/Al$ contacts on the front and rear sides, respectively, and the Sun J-V curve and pseudo-J-V curve of the device. Reprinted with permission from ref. [274]. Copyright 2020, Wiley-VCH.

the PCE of the devices with TiO_x-based ESC was limited by a relatively low V_{oc} (~ 675 mV), compared to that of SHJ and TOPCon devices. Although a-Si:H/TiO_x stack was demonstrated to exhibit excellent surface passivation, the illuminated J-V curve of the device with a-Si:H/TiO_x contact exhibits an "S-shape", indicating a poor electron selectivity [285,286].

A low WF material capping (*e.g.*, LiF, Ca and Yb) was found to be effective in improving the electron selectivity of TiO_x-based ESC [287–289]. The ρ_c of Si/TiO_x heterojunction was dramatically reduced to ~ 5 mΩ•cm^2 by introducing the LiF and Ca capping, enabling a partial contact design. By the implementation of a partial TiO_x/LiF and TiO_x/Ca passivating contact on n-Si solar cells, high PCEs of 23.1% and 21.8% were achieved, respectively [287,288]. With the Yb capping, a very low ρ_c ~ 1 mΩ•cm^2 was realized on textured Si/a-Si:H/TiO_x/Yb hetero-contact, and a PCE of 19.2% was achieved [289]. TiO_x-based ESC was proven to be the most promising dopant-free passivating contacts for c-Si solar cells, given its high electron selectivity, flexible deposition techniques and relatively high stability.

Other metal oxides (*e.g.*, MgO, NbO_x and ZnO) with a suitable band offset with Si were also investigated as ESC for c-Si solar cells. MgO deposited by either thermal evaporation or ALD was proven to be an efficient ESC for c-Si solar cells [278,279]. The electron selectivity of MgO was attributed to the high electron concentration and high bulk conductivity of MgO [278]. Although a low ρ_c of ~ 18 mΩ•cm^2 was achieved on Si/MgO hetero-contact, MgO deposited by either thermal evaporation or ALD exhibits poor surface passivation on c-Si [278,279]. A moderate PCE of 20% was achieved using thermal evaporated MgO contact, figuring a low V_{OC} of 629 mV [278]. In contrast, thin TaO_x deposited by ALD exhibits excellent surface passivation (J_0 ~ 22.5 fA/cm^2), but the high-quality electron selectivity cannot be achieved unless an additional hydrogenation process and Mg capping were applied together, probably due to a poor band alignment with c-Si [280]. Moreover, the surface passivation of TaO_x suffered from a severe degradation after Al metallization, similar to that of TiO_x contact. Therefore, the device with TaO_x contact exhibits a low V_{OC} of 638 mV and a low FF of 79.3%, resulting in a low PCE of 19.1%. It would be interesting to introduce the tunnel SiO_2 passivation interlayer into the MgO and TaO_x contacts in the future work, similar to that of SiO_2/TiO_x contact. Thin NbO_x deposited by ALD seems to be an excellent ESC for c-Si solar cells, which simultaneously exhibits excellent surface passivation (J_0 ~ 25 fA/cm^2) and an acceptable contact resistivity (ρ_c ~ 70 mΩ•cm^2) [281]. However, no device with NbO_x-based contact has been reported. ZnO is supposed to be an ideal ESC for c-Si solar cells, thanks to a small ΔE_C and a large ΔE_V with c-Si. Unfortunately, early works demonstrated that ZnO exhibited poorer performance than expected, featuring low surface passivation and a high ρ_c [290–292]. Zhong et al. found that a rather thick ZnO film (75 nm) capped with LiF_x/Al simultaneously enables efficient electron selectivity and suppression of parasitic infrared absorption. Combined the electron-selective ZnO/LiF/Al contacts with transparent MoO_x-based hole-collecting contacts at the front, both-side dopant-free contact solar cells with a state-of-the-art efficiency of 21.4% was achieved (Fig. 15 (b)) [274]. It was found that metal oxide-based passivating contacts have to be metallization with a low WF Al, which mostly results in degrading passivation quality. To avoid the electron selectivity degradation,

a passivation interlayer (*e.g.*, SiO_2 or a-Si:H) or a low WF capping layer (*e.g.*, LiF) is necessary.

Beside transition metal oxide, other types of ESC materials consist of alkali/alkaline fluorides or metals, mainly including LiF, magnesium fluoride (MgF_2) and Mg. Thermal evaporated LiF, featuring a very low WF of ~ 2.9 eV, is the most frequently studied. Very low ρ_c of ~ 1 mΩ•cm^2 and ~ 7 mΩ•cm^2 were achieved on the n-Si/LiF and n-Si/a-Si:H/LiF hetero-contacts, respectively [293]. A PCE of 19.4% was initially obtained on n-Si solar cells featuring a full-area electron-selective a-Si:H/LiF hetero-contacts [293], and further enhanced to 20.7% with a modified a-Si:H/TiO_x/LiF hetero-contacts featuring better thermal stability [294]. Benefiting from the ultra-low contact resistivity, partial LiF contact was successfully implemented into n-Si solar cells, achieving a PCE of 20.6% [295]. The results reveal that LiF capping is an efficient way to improve the electron selectivity of metal oxide-based ESCs, as demonstrated on TiO_x/LiF and ZnO/LiF stacks. Low WF MgF_2 (~ 3.5 eV) deposited by thermal evaporation was also developed as ESC for c-Si solar cells. n-Si/MgF_2 and n-Si/a-Si:H/MgF_2 hetero-contacts exhibited a low ρ_c value of ~ 35 mΩ•cm^2 and ~ 76 mΩ•cm^2, respectively. A PCE of 20.1% was obtained on n-Si solar cells featuring a full-area a-Si:H/MgF_2/Al hetero-contacts [296]. With a further improved a-Si:H/MgF_2 hetero-contacts using Mg capping, a PCE of 22.1% was obtained on n-Si solar cells with IBC design [297]. Moreover, low WF metals (*e.g.*, Ca and Mg) combined with passivation interlayers (*e.g.*, a-Si:H, SiO_2, and TiO_x) were also developed as ESCs for c-Si solar cells. With a full-area a-Si:H/Mg or SiO_2/Mg contact, *n*-Si solar cells with PCEs of 19% and 15% were achieved, respectively [298,299]. Although alkali/alkaline fluorides or metals based ESCs can form a low ρ_c on c-Si, they are not stable in air and require continuous metallization without vacuum break, which limits their application for mass production. Moreover, they exhibit a very poor surface passivation quality, so a passivation interlayer is necessary to improve the J_0.

Considering the stability issue and low conductivity property of metal oxide/fluoride-based ESCs, transition metal nitrides are being investigated as potential alternatives. Transition metal nitrides are widely used as a copper diffusion barrier for microelectronics and photoanode for photo-electrochemical water splitting, thanks to their high stability and high conductivity [300–302] tantalum nitride (TaN_x) deposited by ALD was first developed as an efficient ESC, simultaneously featuring moderate surface passivation and a low ρ_c on c-Si [302]. A PCE of 20.1% was obtained on n-Si solar cells featuring a full-area TaN_x rear contact for electron collection. Although TaN_x exhibits much poorer surface passivation than that of TiO_x and TaO_x, the device with TaN_x contact exhibited a higher FF and a comparable V_{OC}, resulting in a higher PCE than that of single-layer TiO_x and TaO_x contacts. It means that the surface passivation and contact resistivity of TaN_x were fully maintained on the device level, indicating that no degradation occurring during metallization. Verified by high-resolution TEM measurement, no interlayer was observed at the Si/TaN_x/Al interfaces, confirming the high stability of TaN_x contact. Titanium nitride (TiN) deposited by reactive sputtering was also developed as electron-selective, hole-blocking contact for c-Si solar cells [303]. Highly conductive TiN combined with a SiO_2 passivation interlayer was demonstrated to be an effective ESC on c-Si, featuring a low ρ_c of 16.4 mΩ•cm^2 and a tolerable J_0 of ~ 500 fA/cm^2. SiO_2/TiN contact was innovatively employed as surface passivating and metal electrode simultaneously on n-Si solar cells, achieving a PCE of 20% with a simplified fabrication process and low cost (Fig. 16 (a)). It is by far the only developed ESC without

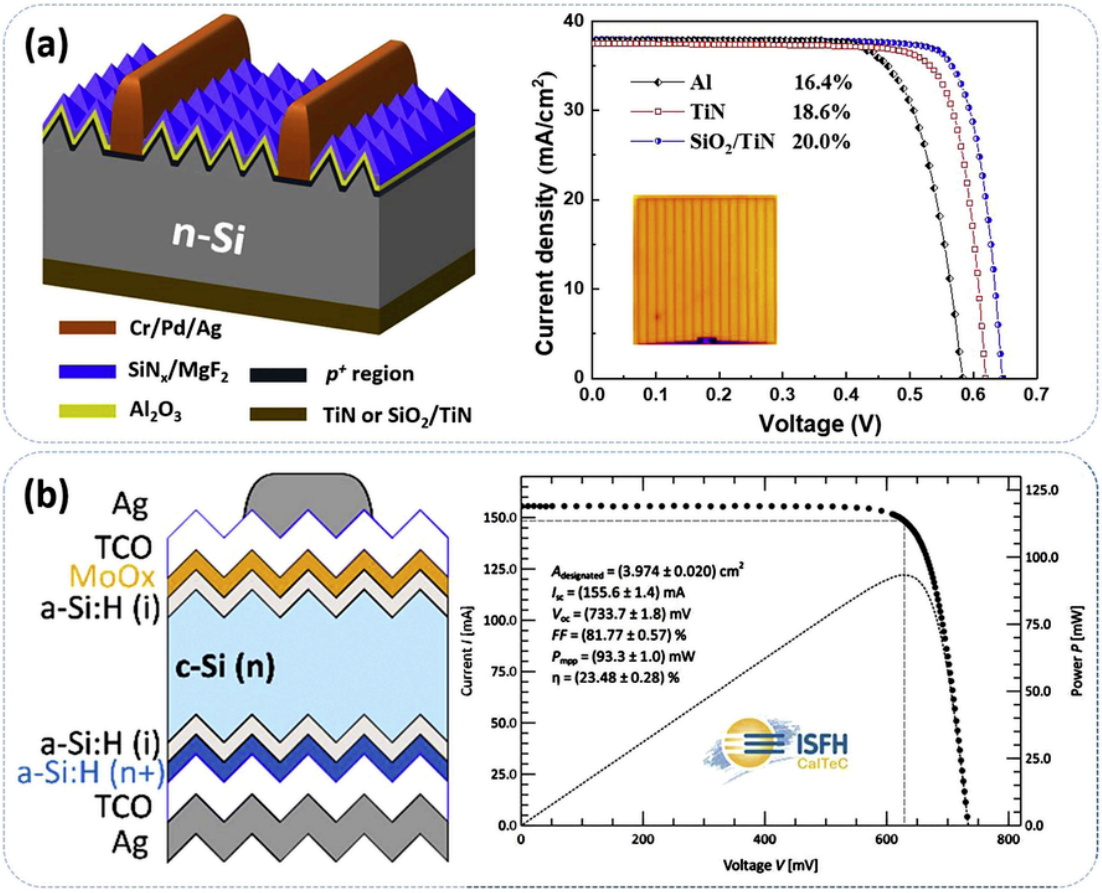

Fig. 16. (a) Sketch of an n-Si solar cell featuring full-area TiN rear contacts, and their light J-V curves. Reprinted with permission from ref. [303]. Copyright 2019, Elsevier. (b) SHJ solar cells with a front hole-selective MoO_x contact, achieving a certified efficiency of 23.5%. Reprinted with permission from ref. [18]. Copyright 2020, Elsevier.

low WF metal capping. The surface passivation quality of both TiN_x and TaN_x contacts is still poorer than that of metal oxides, which limits the PCE of the devices. Both works demonstrated the high potential of metal nitride-based ESCs for c-Si solar cells, which might improve the device performance and reduce the fabrication cost simultaneously. Other transition metal nitrides (*e.g.*, zirconium nitride (ZrN_x), hafnium nitride (HfN_x), molybdenum nitride (MoN_x)) might be interesting for further investigation.

4.1.3. Hole-selective contact materials and devices

In the meantime, researchers were also researching HSC materials for c-Si solar cells. P-type transition metal oxides with a small ΔE_V with Si are less abundant than of ESC, as shown in Fig. 14. Nickel oxide (NiO_x) and copper oxide (Cu_2O) with a small ΔE_V with Si were initially investigated as HSC [304–306]. Unfortunately, both NiO_x and Cu_2O exhibited poor surface passivation and hole selectivity, resulting in inferior device performances.

Transition metal oxides featuring a high WF, mainly including MoO_x, vanadium oxide (VO_x) and tungsten oxide (WO_x), were intensively investigated as HSC materials [40,307–314]. High WF materials deposited on c-Si are supposed to induce strong upward band bending, favoring the hole-transport at the interface. Among them, MoO_x deposited by thermal evaporation is the most successful HSC developed by far. A low ρ_c was obtained at the Si/MoO_x heterojunction, and wide bandgap MoO_x also exhibited moderate surface passivation on c-Si and high transparency [40]. By replacing the p-type a-Si:H in SHJ device with the highly transparent MoO_x, the external quantum efficiency in the blue and visible range was enhanced, resulting in an obvious improvement of J_{SC} ($> 1\,mA/cm^2$) [18,307]. A PCE of 22.5% was achieved on SHJ device with a hole-selective MoO_x front contact in 2015 [309], and recently the PCE has been enhanced to 23.5% by further optimizing the MoO_x thickness and fabrication process (Fig. 16 (b)) [18]. However, the hole selectivity of thermal evaporated MoO_x was found to be unstably incompatible with the final contact annealing (~ 200 °C) of SHJ device, which was attributed to the reduced MoO_x by the hydrogen diffusion from the a-Si:H passivation layer. Although a pre-annealing in the air at 250 °C followed by a short hydrofluoric acid dipping was developed by Essig et al. to overcome this problem, the process complexity was enhanced [315]. MoO_x films deposited by both ALD and sputtering at low temperatures were also investigated; however, the result indicated that the WF of ALD MoO_x is too low to be an efficient HSC for c-Si solar cells [316,317].

Beside MoO_x, VO_x deposited by vacuum thermal evaporation was also intensively investigated as HSC for c-Si solar cells [311,312,318]. Gerling et al. reported that VO_x exhibited better surface passivation than that of MoO_x, which predicted the high potential of VO_x as HSC [318]. However, until now the best PCE of 19.7% was reported on IBC c-Si solar cells with thermal evaporated VO_x contact [311]. Recently, VO_x deposited by ALD was demonstrated to be a promising HSC, featuring good surface passivation, a high WF (~ 6 eV), a tolerable ρ_c and high stability. By replacing the rear p-type a-Si:H with VO_x contact, a state-of-the-art PCE of 21.6% was achieved on SHJ device featuring a rear junction configuration [319]. It would be more interesting to apply the ALD VO_x contact on the front side of SHJ devices in future work. WO_x deposited by thermal evaporation was also investigated as HSC for c-Si solar cells [313,314], however, the best PCE reported was lower than that of MoO_x and VO_x. It was suspected that the high oxygen vacancy in WO_x reduces its WF, resulting in a reduced band bending and consequently a poor hole selectivity [314]. Chromic oxide (CrO_x) deposited by thermal evaporation was also developed as HSC, achieving a low ρ_c of 40 $m\Omega \cdot cm^2$ on p-Si/CrO_x hetero-contact [320]. By the implementation of a partial CrO_x rear contact, a PCE of 20.2% was achieved on p-Si solar cells.

All these high WF HSC materials deposited by thermal evaporation exhibit poor surface passivation on c-Si, and their hole selectivity is quite sensitive to air exposure, thermal annealing and electrode materials [321,322]. If combined with an a-Si:H passivation interlayer, they suffered from the hydrogen-induced hole selectivity degradation. Until now, it is still a very challenging topic to develop high-quality HSC with high stability. A fundamental understanding and investigation of the material and hetero-contact properties that governing the hole selectivity and surface passivation is high required for further engineering and tailoring of the metal oxide-based HSC.

4.2. Si/organic heterojunction solar cells

4.2.1. Development status

In 1990, Lewis and coworkers firstly presented a Si/organic heterojunction solar cell with a very low PCE of ~1% [325]. The heterojunction is made of poly-$(CH_3)_3$Si-cyclooctatetraene and Si. After that, several organic materials, such as poly(2-methoxy-5-(2'-ethyl-hexyloxy)-1,4-phenylenevinylene), PEDOT:PSS, poly(3-hexylthiophene) (P3HT), and branched polyethylenimine (b-PEI), were proposed to fabricate Si/organic heterojunction solar cells [326–329]. The best PCE of 20.6% has also been achieved by far [324]. The evolvement of PCE promises a tendency to reach the efficiency of homojunction Si solar cells fabricated by complicated processes. PV parameters of typical Si/organic solar cells are summarized in Table 3.

4.2.2. Progress of Si/organic heterojunction solar cells

Among various Si/organic heterojunction solar cells, Si/PEDOT:PSS based ones have been researched widely. Fig. 17 (a) shows the chemical structure of PEDOT and PSS. PEDOT molecule (molecule weight (MW) ~1000-2500 Da) is hydrophobic, while PSS molecule (MW~400000 Da) is hydrophilic. PEDOT adheres to the segment of PSS chain *via* Coulomb attraction, forming PEDOT:PSS molecules [349]. Because of the different dispersibility, PEDOT:PSS presented a colloidal structure in water, where PEDOT is sheltered by PSS to form a stable colloid in water. Sulfonate groups on PSS serve as a dopant of PEDOT to improve the conductivity of PEDOT:PSS. On the other hand, the insulation of PSS causes a barrier that blocks the charge transfer among PEDOT molecules. Additionally, because of the interaction among PEDOT, PSS and water, the segment of PEDOT:PSS is twisted, reducing the charge transfer property. And the twisted structure is conserved in film condition (Fig. 17 (b)) [350]. The conductivity of PEDOT:PSS plays a key role in the performance of Si/PEDOT:PSS solar cells. There are several schemes on targeting the conductivity of PEDOT:PSS, such as, tailoring the ratio of contents, changing the molecular conformation, improving WF, and mixing high conductivity materials [334,337,339,351–356].

Polar solvents are effective in improving the conductivity of PEDOT:PSS films. The mechanism includes two aspects typically: changing the conformation of PEDOT molecules or decreasing the ratio of PSS. As shown in Fig. 17 (c, d), adding dimethyl sulfoxide (DMSO) enhances the π-π interchain packing and enlarges the crystalline domain size of PEDOT. This leads to a significant enhancement in the charge transfer property of PEDOT. In contrast, ethylene glycol (EG) treatment can decrease the ratio of insulating PSS. In other words, EG decreases the charge transfer barrier among PEDOT domains [357]. Leung and coworkers treated PEDOT:PSS with DMSO or EG, which changed the content and conformation of PEDOT:PSS and consequently improved the conductivity of PEDOT:PSS film. A PCE of 12% was realized in Si/PEDOT:PSS solar cells [352]. Similarly, p-toluenesulfonic acid as an additive in PEDOT:PSS can realize the phase separation between PEDOT and PSS, resulting in an increased conductivity of PEDOT:PSS film. The PCE of solar cells improved from 12% to 14% [337]. Methanol and EG were also mixed as additives to treat PEDOT:PSS and presented a PCE of 14.6% [339]. Meanwhile, highly conducting materials, such as silver nanowires and carbon nanotubes, were embedded into PEDOT:PSS film [355,356]. Upon incorporating silver nanowires, the resistance of PEDOT:PSS film was reduced to 100 Ω/sq, enhancing the charge collection significantly, and a PCE of 15% was achieved [356].

Table 3
Electrical properties of typical Si/organic heterojunction solar cells.

Device configuration[a]	Si structure	V_{OC} (V)	J_{SC} (mA/cm2)	FF	PCE (%)	Reference
ITO/PEDOT:PSS/Si	nanowire	0.47	19.28	0.61	5.09	[328]
Ag:Cu/PEDOT:PSS/Spiro/Si/In:Ga	nanowire	0.527	31.3	0.588	9.7	[330]
Ag/Pd/PEDOT:PSS/P3HT/Si/Al	planar	0.59	29	0.59	10.1	[331]
Ag/PEDOT:PSS/Si/Al	pyramid/nanowire	0.52	34.46	0.641	11.48	[332]
Ag/PEDOT:PSS/TAPC/Si/Al	nanowire	0.54	34.76	0.695	13.01	[333]
MoO_3/Ag/PEDOT:PSS/Si/Liq/Al	planar	0.63	29.2	0.749	13.8	[334]
Ag/PEDOT:PSS/Si/Al	UMG	0.523	30.9	0.745	12.0	[335]
Ag/PEDOT:PSS/Al_2O_3/Si/Al	nanowire	0.539	36.0	0.678	13.2	[336]
TiO_2/Ag/PEDOT:PSS:PTSA/Si/In:Ga	planar	0.62	34.3	0.73	15.5	[337]
ITO/PEDOT:PSS/TiO_2/Si/TiO_2/Al	nanohole	0.63	35.91	0.65	14.7	[338]
Ag/PEDOT:PSS:EG:MeOH/Si/Al	planar	0.62	29.3	0.802	14.6	[339]
Ag/PEDOT:PSS:GOPS/Si/Al	nanowire	0.64	30.2	0.728	14.1	[340]
Ag/PEDOT:PSS/Si/in/ITO/Ag	pyramid	0.634	36.2	0.705	16.1	[341]
Ag/PEDOT:PSS/Si/F-N2200/Al	nanowire	0.635	31.1	0.733	14.5	[342]
Ester/Ag/PEDOT:PSS/Si/in/Al	pyramid	0.634	36.5	0.70	16.2	[343]
Ag/PEDOT:PSS/Si/PCBM/Al	nanowire	0.646	31.37	0.743	14.9	[344]
Ag/PEDOT:PSS/Si/CPTA/Al	pyramid	0.632	34.7	0.763	16.73	[345]
CuI/Ag/PEDOT:PSS/Si/PTB7-NBr/Al	pyramid	0.638	32.8	0.765	16.0	[346]
Ag/PEDOT:PSS/Siloxane/Si/Siloxane/Ti/Ag	micropillar/pyramid	0.61	38.41	0.74	17.34	[347]
Ag/PEDOT:PSS/Si/TiO_2/LiF/Al	pyramid	0.626	31.9	0.756	15.1	[348]
Ag/ITO/ip/Si/Si/i/b-PEI/Al	pyramid	0.72	37.0	0.729	19.4	[329]
Ag/PEDOT:PSS/SiO_2/Si/n^+ Si/SiN_x/Al	pyramid	0.657	38.9	0.806	20.6	[324]

[a] i: intrinsic a-Si:H; in: intrinsic a-Si:H/n-type a-Si:H stack; ip: intrinsic a-Si:H/p-type a-Si:H stack; Spiro: spiro-OMeTAD; TAPC: 1,1-bis[(di-4-tolylamino)phenyl] cyclohexane; Liq: 8-hydroxyquinolinolato-lithium; UMG: upgraded metallurgical grade; PTSA: p-toluenesulfonic acid; MeOH: methanol; GOPS: 3-glycidoxypropyltrimethoxydsilane; F-N2200: naphthalene diimide-based conjugated polymer; PCBM: [6,6]-phenyl-C61-butyric acid methyl ester; CPTA: C60 pyrrolidine tris-acid; PTB7-NBr: conjugated polyelectrolytes; b-PEI: branched polyethylenimine.

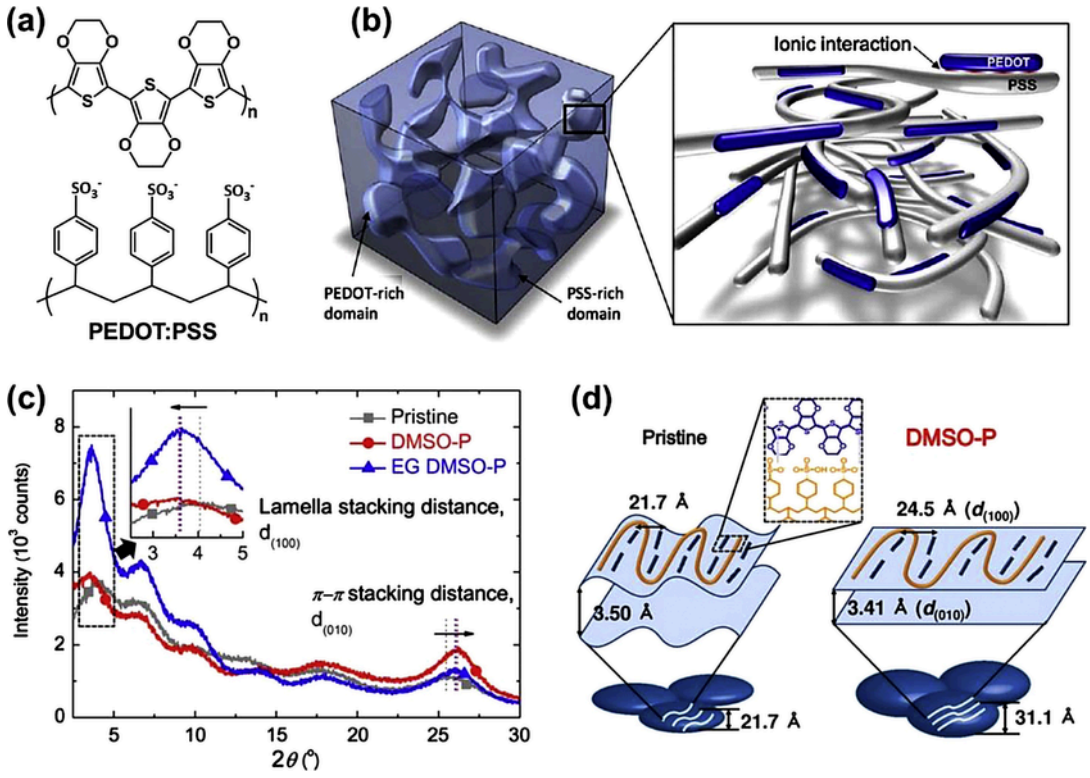

Fig. 17. (a) Chemical structure of PEDOT:PSS molecules. (b) Schematic diagram of PEDOT:PSS film morphology. Reprinted with permission from ref. [350]. Copyright 2017, AAAS. (c) X-ray diffraction and (d) conformation change of PEDOT:PSS films. Pristine: reference PEDOT:PSS film. DMSO-P: dimethyl sulfoxide treated PEDOT:PSS film. EG DMSO-P: dimethyl sulfoxide and ethylene glycol treated PEDOT:PSS film. Reprinted with permission from ref. [357]. Copyright 2012, American Physical Society.

On the other hand, a well-matched WF between Si and organic materials is critical to efficiencies [358,359]. PEDOT:PSS with a deep WF is favorable for generating a large V_{bi}. Targeting a deep WF of PEDOT:PSS, perfluorinated ionomer (PFI) was added into PEDOT:PSS. Due to the high electron affinity of PFI, the WF of PEDOT:PSS film increased ~0.2 eV, enlarged the V_{bi} of solar cells. As a result, the PCE enhanced by 20% compared with pure PEDOT:PSS based solar cells [354]. Cobalt sulfide was also served as an additive to increase the WF of PEDOT: PSS, which resulted in an obvious increase of PCE [360]. In addition to additive engineering, post-treatment is a facile method im-

proving the WF of PEDOT:PSS. Depositing an organic molecule of 1, 4, 5, 8, 9, 11-hexaazatriphenylene hexacarbonitrile (HAT-CN) onto PEDOT:PSS films improved the WF of PEDOT:PSS from 5.0 eV to 5.4 eV [361]. A strong inversion layer was formed on a Si surface, which results in a larger V_{bi}, thus increases carrier collection and decreases the adverse recombination [358,362]. Evaporated tungsten oxide [363] or copper iodide [364] demonstrated similar results with HAT-CN, and the PCE of a Si/PEDOT:PSS solar cell reached 14.3% [364].

The reflection of planar Si would limit light harvest efficiency. Si surface texture is a general solution reducing reflection. By far, various structures, such as nanowires, nanocones, nanopillars, nanotubes, nanoholes, pyramids, and composite structures, are successively used in Si/PEDOT:PSS solar cells to reduce the reflection [365–372]. On the other hand, because of the large surface tension of PEDOT:PSS solution, conformal contact is difficult to be realized between textured Si and PEDOT:PSS film, as shown in Fig. 18 (a). The existence of the space blocks the charges transport. At the same time, the exposed Si surface is prone to the formation of defects that cause serious recombination losses. Sun and coworkers incorporated a silane chemical of 3-glycidoxypropyltrimethoxydsilane (GOPS) into PEDOT:PSS, where GOPS could act as a bridge to anchor PEDOT:PSS *via* building chemical bonds with Si. These bonds lead to a favorable contact between PEDOT:PSS film and textured Si surface (Fig. 18 (b, c)). Besides, GOPS can suppress surface Si defect due to formation of Si-O bond, reducing the surface recombination velocity. With the improvement of the contact, both the charge transfer barrier and recombination losses were reduced. As a result, the V_{OC} and the FF increased significantly, yielded a PCE of 14% [340]. Ye and coworkers applied a bilayer PEDOT:PSS structure to realize a conformal contact between Si and PEDOT:PSS film. A high-adhesion PEDOT:PSS deposited onto Si substrates, followed by a PEDOT:PSS film with high conductivity (Fig. 18 (d, e)). This bilayer structure optimized the contact and improved the PCE to 17% [345].

Due to masses of defects on the textured Si surface, a severe surface recombination loss is existence in solar cells. This loss limits the V_{OC} of solar cells. Therefore, passivation engineering is essential in the textured Si surface. Chemical passivation, field-effect passivation, and selective contact passivation are widespread methods suppressing surface recombination [173,373,374]. Among various passivation methods, methyl-termination is a facile one achieving chemical passivation on Si surface [375]. The unsaturated bonds on Si surface can be terminated by methyl groups by forming Si-CH_3 bonds that suppress surface recombination effectively. Meanwhile, methyl-termination generates a positive dipole that is favorable for charges collection, as shown in Fig. 19 (a) [376]. After methyl passivation, the champion PCE reached 10.2% in Si/organic solar cells [377,378]. Tetramethylammonium hydroxide (TMAH) is another effective material to control Si surface recombination *via* solution processes [379]. TMAH can reduce surface/volume ratio of textured Si through chemical etching, which decreases masses of surface traps and also improves the contact quality between Si and PEDOT:PSS. Sun and coworkers chose TMAH as a second etching material to tailor the surface condition of Si. The reverse saturation current was suppressed, as shown in Fig. 19 (b) of I-V curves under dark condition and a PCE of 12.0% was achieved in upgraded metallurgical-grade based Si/PEDOT:PSS solar cells [335].

It is worth noting that these passivation effects are not independent, *i.e.*, one material could possess more than one passivation effect. For instance, Al_2O_3 demonstrates chemical and field-effect passivation effects simultaneously [369,380]. Because of the large negative charge density, electrons will be repulsed away from Si surface, generating a strong inversion layer that realizes a field-effect passivation effect. Meanwhile, the chemical bonds formed between Al_2O_3 and Si can reduce surface traps. Pudasaini and coworkers deposited an ultrathin Al_2O_3 layer onto the Si surface, improving the PCE to over 10% [369]. Si-O-Ti bonds formed on the Si surface after depositing TiO_x film, which could reduce the density of traps and improve minority carrier lifetime effectively. [381–383]. Pei and coworkers presented an improved efficiency after depositing TiO_x layer between Si and PEDOT:PSS. A PCE of 14.7% was achieved [338]. The selective contact passivation of TiO_x is unfavorable for holes collection at Si/PEDOT:PSS side. However, chemical passivation took a larger advantage over selective contact one in this case. Additionally, organic interface layers with holes selective property are also applied to reduce recombination between Si front surface and PEDOT:PSS. Sturm and coworkers incorporated P3HT between Si and PEDOT:PSS, where P3HT could block electrons transferring to PEDOT:PSS film. The blocking effect reduced the dark current caused by the injection of electrons from Si to PEDOT:PSS, as shown in Fig. 19 (c) [331]. Yu and coworkers introduced an organic molecule of 1,1-bis[(di-4-tolylamino)phenyl]cyclohexane (TAPC) between Si and PEDOT:PSS, where the τ_{eff} was improved to 88 μs (Fig. 19 (d)), and consequently, the PCE improved to 13% [333]. Inserting an electron block material of N,N'-bis(3-methylphenyl)-N,N'-diphenylbenzidine between Si and PEDOT:PSS demonstrated similar effects with P3HT or TAPC [384].

In addition to these applied strategies of front surface, various organic materials present facile choices for controlling the recombina-

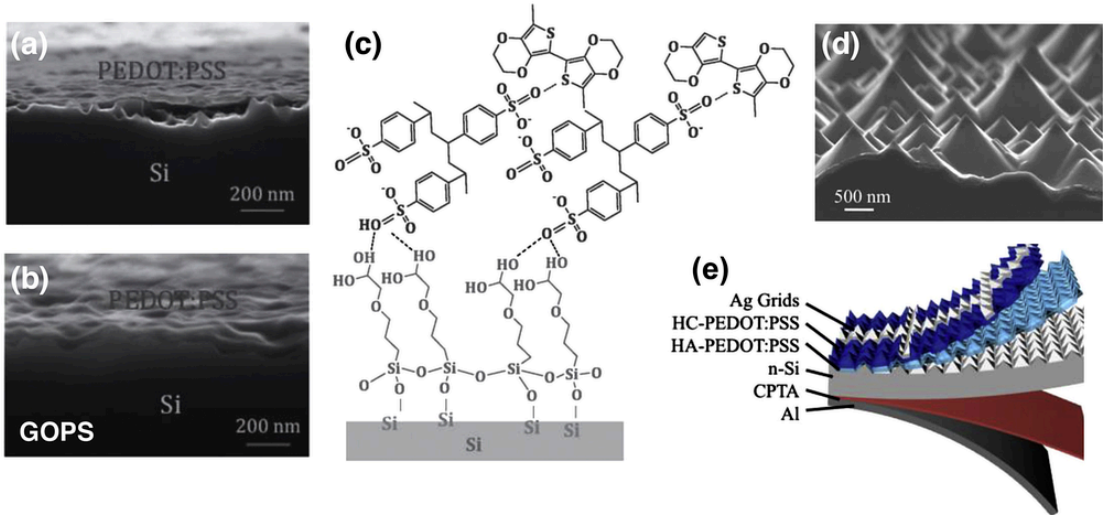

Fig. 18. Cross-sectional SEM images of PEDOT:PSS on textured Si substrates (a) without or (b) with GOPS. (c) Chemical bonds among Si/PEDOT:PSS/GOPS. Reprinted with permission from ref. [340]. Copyright 2016, Wiley-VCH. (d) Cross-sectional SEM image and (e) schematic of bilayer PEDOT:PSS on textured Si substrates. Reprinted with permission from ref. [345]. Copyright 2018, Wiley-VCH.

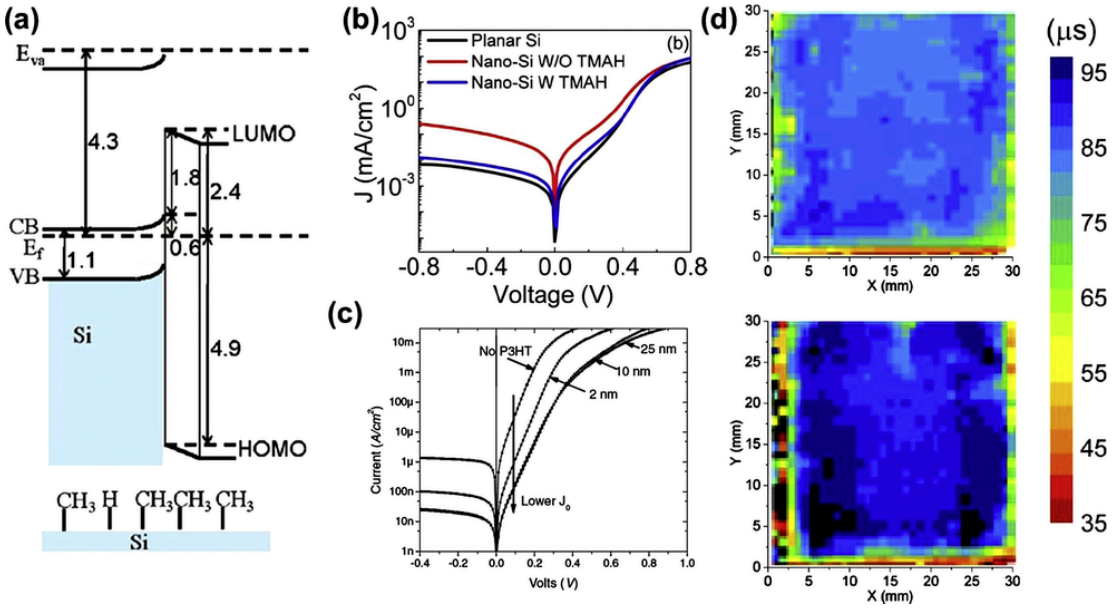

Fig. 19. (a) Energy band diagram of methyl-terminated Si. Reprinted with permission from ref. [376]. Copyright 2011, American Chemical Society. (b) Current-voltage curves of solar cells with or without TMAH modification under dark condition. Reprinted with permission from ref. [335]. Copyright 2014, American Chemical Society. (c) Current-voltage curves of solar cells with or without P3HT interface layers under dark condition. Reprinted with permission from ref. [331]. Copyright 2011, Wiley-VCH. (d) Spatial mapping of the minority carrier lifetime. Reprinted with permission from ref. [333]. Copyright 2013, American Chemical Society.

tion losses that occurred between Si rear surface and electrodes. "BackPEDOT" fabricated by organic materials deposited onto Si rear surface is an enlightened structure to reduce rear surface recombination losses [324,385–388]. Zielke et al. presented a "backPEDOT" Si solar cell with phosphorus diffused front emitter [385]. Compared with conventional Si solar cells, such as Al-BSF or PERC, solution-processed "backPEDOT" simplified the fabrication techniques. However, owing to the FF is limited by relatively high contact resistance, the efficiency is 17.4%. Furthermore, Schmidt et al. incorporating sorbitol into PEDOT:PSS, achieving a low ρ_c of 56.3 mΩ•cm^2. The efficiency reached 20.6% that is close to 20.9% of AlO_x/SiN_x rear surface passivated PERC solar cell [324].

Meanwhile, an organic molecule of 8-hydroxyquinolinolato-lithium (Liq) is applied to modify the contact quality between the Si rear surface and electrodes (Al). Since Liq changed the WF of Al from 4.3 eV to 3.2 eV, the contact barrier was reduced and a favorable downward band bending was realized [389]. Ye and coworkers chose poly (ethyleneoxide) (PEO) as an interface layer between Si and electrodes. An interface dipole resulting from PEO interface enlarged the V_{bi}, and then realized a PCE of 12.3% [390]. He et al. introduced different narrow bandgap conjugated polyelectrolytes, PTB7-NBr and PTB7-NSO_3, to improve the contact quality between the Si rear side and Al [346]. The electrical property of PTB7-NBr realized a lower contact resistance of 6.7 ± 0.8 mΩ·cm^2 compared with that of PTB7-NSO_3 (50 ± 25 mΩ·cm^2). Additionally, the better passivation effect of PTB7-NBr reduced recombination losses. As a result, PTB7-NBr based solar cells gave a PCE 16% enhancement ratio. However, solar cells with PTB7-NSO_3 only presented an enhancement ratio of 6%. Additionally, b-PEI is utilized as a rear side buffer layer for amorphous Si/c-Si solar cells. The incorporation of b-PEI interlayer between c-Si(n) and Al results to a very low ρ_c of 24 mΩ·cm^2, and a device with an electron-selective contact comprised of a-Si:H(i)/b-PEI/Al yield a PCE of 19.4%. This electron-selectivity of b-PEI is ascribed to its Lewis basicity, *i.e.*, electron-donating ability, providing favorable band bending locate surface region for electron transport [329]. It worth noting that a pre-deposited amorphous Si is required to achieve low surface recombination c-Si substrate.

Although organic materials promise a wide choice of achieving recombination control, how to choose the appropriate material is not fully addressed. Sun and coworkers found that the interaction between Si and organic materials is of importance to realize a favorable charge collection [344]. Two widely researched organic materials of [6,6]-phenyl-C_{61}-butyric acid methyl ester (PCBM) and naphthalene diimide-based polymer (N2200) were conducted as interface layers to control recombination at Si rear side. Although both materials can improve the efficiency, different PCE of 13.7% and 14.9% demonstrated on PCBM and N2200 based solar cells, respectively. Further research proved that the molecule structure affected the physical distance between Si and organic materials. There is a shorter distance between PCBM and Si, where a higher charge transfer rate is expected. The higher rate is helpful to build a stronger rear surface field effect that reduced the surface recombination and consequently improved τ_{eff}. Furthermore, alternative naphthalene diimide derivative (F-N2200) was used for deeper exploration with N2200 [342]. The difference of chemical structure between F-N2200 and N2200 was the substitution of the fluorine atom for hydrogen, as shown in Fig. 20. According to the two-dimensional grazing incidence wide-angle X-ray scattering (Fig. 20), F-N2200 has a more compact intermolecular stacking on the Si surface. Meanwhile, density functional theory indicated that the physical distance between Si and F-N2200 backbone (4.2 Å) is shorter than that of N2200 (5.4 Å). Therefore, the PCE (14.5%) of F-N2200 based solar cells was better than that of N2200 based ones.

4.2.3. Ultrathin & flexible Si/organic heterojunction solar cells

With a standard industrial line, the Si thickness is generally no less ~150 μm. Reducing Si wafer thickness is feasible for realizing low-cost solar cells, and flexibility is a decisive advantage extending the application of Si solar cells into daily life, such as a power source of wearable devices and building-integrated photovoltaics (BIPV). Over 70% cost of Si materials can be economized using a 50-μm-thick Si wafer [391]. However, the efficiency is limited by the insufficient light absorption of ultrathin Si substrates, especially in the long-wavelength region. The nanostructure is an effective method of light trapping. For example, a 10-μm-thick Si with inverted nanopyramid achieves light absorption for effective solar cells [392]. Because organic films can avoid crack upon bending and fabricated at a low temperature, Si/organic solar cells possess superiorities compared with fragile Si p-n junction solar cells. A PCE of 5.6% was realized in Si/PEDOT:PSS solar cells based on

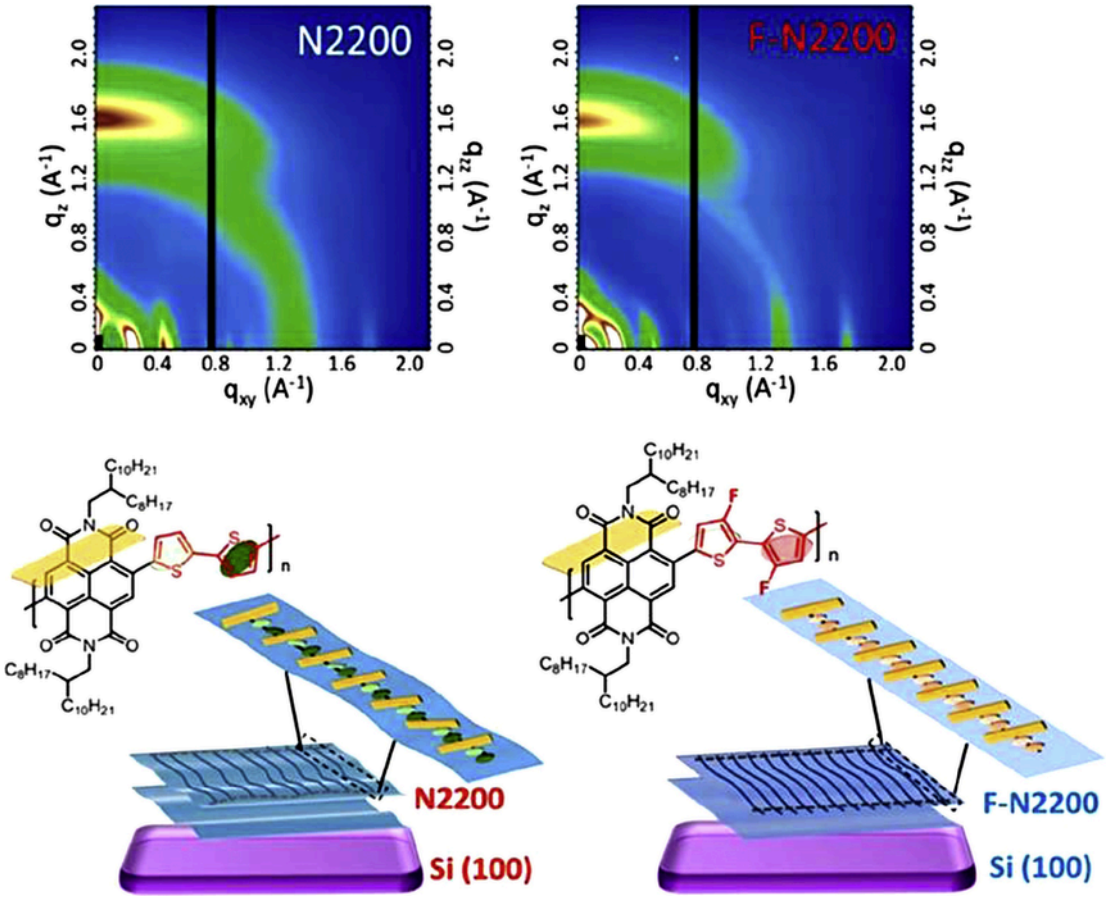

Fig. 20. Two-dimensional grazing incidence wide-angle X-ray scattering, chemical structures and schematic of intermolecular planarity stacking of N2200 or F-N2200 on Si substrates. Reprinted with permission from ref. [342]. Copyright 2017, American Chemical Society.

~2-μm-thick nano-textured Si substrates [393]. Sun and coworkers treated textured Si surface *via* a second etching process, reduced surface recombination losses. And consequently, a PCE of 9.1% was achieved in a flexible Si/PEDOT:PSS solar cell that was fabricated on a ~14-μm-thick Si substrate [394]. Meanwhile, plasmonic effect or hierarchical structure were used in flexible Si/organic solar cells [395,396], and a PCE over 13% was achieved on a 20 μm Si substrates [397]. Currently, the PCE of the ultrathin flexible Si/organic solar cells is mainly limited by low V_{OC}, due to the high surface recombination losses. Although the industrial surface passivation technologies, such as a-Si:H, SiN_x and SiO_2, are very effective, they would increase the cost due to the complex deposition processes and capital-intensive deposition system. Thus, achieving excellent surface passivation is still a challenge to flexible Si/organic heterojunction solar cells.

4.2.4. Stability of Si/organic heterojunction solar cells

To date, notable progress has been made in Si/organic heterojunction solar cells. However, device stability has not been fully addressed. Based on the present research results, the degradation can be attributed to the poor stability of organic materials and contact interfaces. The twenty-five years guarantee of commercial Si PV production demonstrates the long-term working stability of conventional Si solar cells. The organic materials are generally sensitive to the environment, such as heat, light, moisture and oxygen. Herein, a successful commercial product of PEDOT:PSS is taken as an example. As a general material in Si/organic heterojunction solar cells, PEDOT:PSS films present good thermal stability at 200 °C. The thermal degradation of PEDOT:PSS likely occurs at approximately 250 °C, resulted from the fragmentation of PSS groups. In other words, the thermal stability of PEDOT:PSS films meets the requirement of the 85 °C standards in the solar cell field. However, UV light and oxygen would degrade PEDOT:PSS films significantly. The sulfur atoms on the thiophene rings change into insulating sulfoxide and sulfone structures under oxygen conditions, in which UV light accelerates this oxidation process simultaneously. The degradation increases the resistivity and consequently limits device efficiency. Avoiding UV light explosion is necessary for the presence of oxygen, *vice versa*. Additionally, PEDOT:PSS films are sensitive to moisture, caused by the hygroscopic behavior of PSS groups. Removing PSS groups is a feasible method for improving moisture resistance. However, the PSS group owing ~5.5 eV WF is one reason that PEDOT:PSS films have high WF [398]. Hence, a balance is required between WF and PSS ratio. Heterojunction interface quality is another unstable issue. There is a possibility that air could diffuse into the space between Si and PEDOT:PSS inevitably, and then an oxide layer would begin to grow on Si surface, which is uncontrollable compared with that traditional growth at high temperature (over 700 °C) in dry air. A thick SiO_2 layer blocks the charge transfer between Si and organic materials, accompanied by a poor FF. Although encapsulation by far is an effective technology slowing down the degradation caused by the environment, improving environmental stability still needs to be addressed.

4.2.5. Integrated power system based on Si/organic solar cells

Weather condition is an intermittent and unpredictable factor that influents the power output of solar cells. Integrating solar cells with other devices is an alternative to resolve this problem. Generally, there are two schemes including integrating with an energy storage device [399–401] or with a different power collection system [402–405]. The flexibility gives Si/organic solar cells an advantage of integration with energy storage devices for wearable electronics. Sun and coworkers fabricated a self-charging power system by integrating a Si/PE-

DOT:PSS solar cell with a polypyrrole based supercapacitor, where the two units were connected by a shared titanium electrode, as shown in Fig. 21 (a). Record efficiency of 10.5% was realized for energy transformation from photoelectric energy of solar cells into energy stored in supercapacitors [406]. Triboelectric nanogenerators (TENGs) are feasible devices that can harvest mechanical energy from raindrops, wind, or tide. To further extend the utilization of Si/PEDOT:PSS solar cells in different weather conditions, TENGs were integrated onto solar cells [407]. In this case, a raindrop-driven TENG was made by a transparent poly(dimethylsiloxane) and a PEDOT:PSS film. And PEDOT:PSS films served as a conjunct component for a TENG and a solar cell. TENGs collect mechanical energy from raindrops (Fig. 21 (b)); solar cells harvest solar energy. Supercapacitors were charged by the integrated system after a rectifier, as shown in the circuit diagram in Fig. 21 (c). The voltage of a supercapacitor that charged by a solar cell reached 0.6 V. After that, the supercapacitor was charged by a TENG until the voltage came up to 0.9 V, as shown in Fig. 21 (d). The successful conversion from solar and mechanical energy into electrical power demonstrated a promising future for a wide application of Si/organic solar cells.

4.3. Si/two-dimensional materials heterojunction solar cells

Two dimensional (2D) materials possessing unique characteristics are widely applied in optoelectronic devices [408–412]. The heterojunction formed between graphene and n-Si is proved to be a nearly ideal Schottky junction with a low n of ~1.08 (Fig. 22 (a)) [413]. Pioneer work by Zhu and coworkers presented a graphene/Si solar cell with a PCE of 1.5% [414]. The lower efficiency was owing to the unmatched WF and the high vertical resistance of multi-layer graphene. Chemical doping is an effective solution for resolving these problems in graphene/Si solar cells. After a chemical doping, the V_{bi} was enlarged and the resistance of graphene sheets was reduced. As a consequence, the PCE of graphene/Si solar cells improved to 8.6% [415,416]. The high reflection of graphene/Si, as shown in Fig. 22 (b), also limits the efficiency of solar cells. To reduce reflection losses, an antireflection layer of TiO_2 was deposited onto graphene/Si solar cells. The J_{SC} was enhanced from 23.9 mA/cm^2 to 32.5 mA/cm^2, yielded an improved PCE of 14.5% [417]. Additionally, interface layers were also implemented to reduce charge recombination losses. An electron-blocking P3HT layer was inserted between Si and graphene, which reduced charges recombination and a PCE of 10.3% was achieved [418]. Kong and coworkers grew a native SiO_x between graphene and Si, where the recombination velocity was dramatically suppressed. Combined with chemical doping and anti-reflection technologies, a champion PCE of 15.6% was achieved in graphene/Si solar cells. On the other hand, Yu and coworkers demonstrated a quasi p-n junction generated in graphene/Si solar cells, by depositing a WO_3 onto Si [419]. Because of large Fermi-level offset between WO_3 and Si, a charge transfer occurred between Si and WO_3, resulting in a large upward band bending, accompanied by a large V_{bi} within graphene/Si junction. This case is favorable for high-efficiency graphene/Si solar cells.

As an important 2D transition metal, dichalcogenide material MoS_2, is attracting increasing attention in heterojunction solar cells [420–422]. Pioneer work by Chen and coworkers presented a MoS_2/Si heterojunction solar cell with a PCE of 5.23% *via* transferred large-scale MoS_2 onto p-type Si [423]. MoS_2 acted as an electron-selective contact in MoS_2/p-Si heterojunction devices, according to Fig. 22 (c) of energy change spectra. Because of MoS_2 was prepared by a chemical vapor deposition technology, the MoS_2/Si structure promises a wafer-sized heterojunction solar cell. On the other hand, trap-assisted recombination losses limit efficiency, and surface passivation has to be implemented. SiO_2 was first chosen as a passivation layer, resulting in an enhanced PCE from 1.4% to 4.5% [424]. Al_2O_3 was also served as a passivation layer in MoS_2/Si heterojunction solar cells. Different from the chemi-

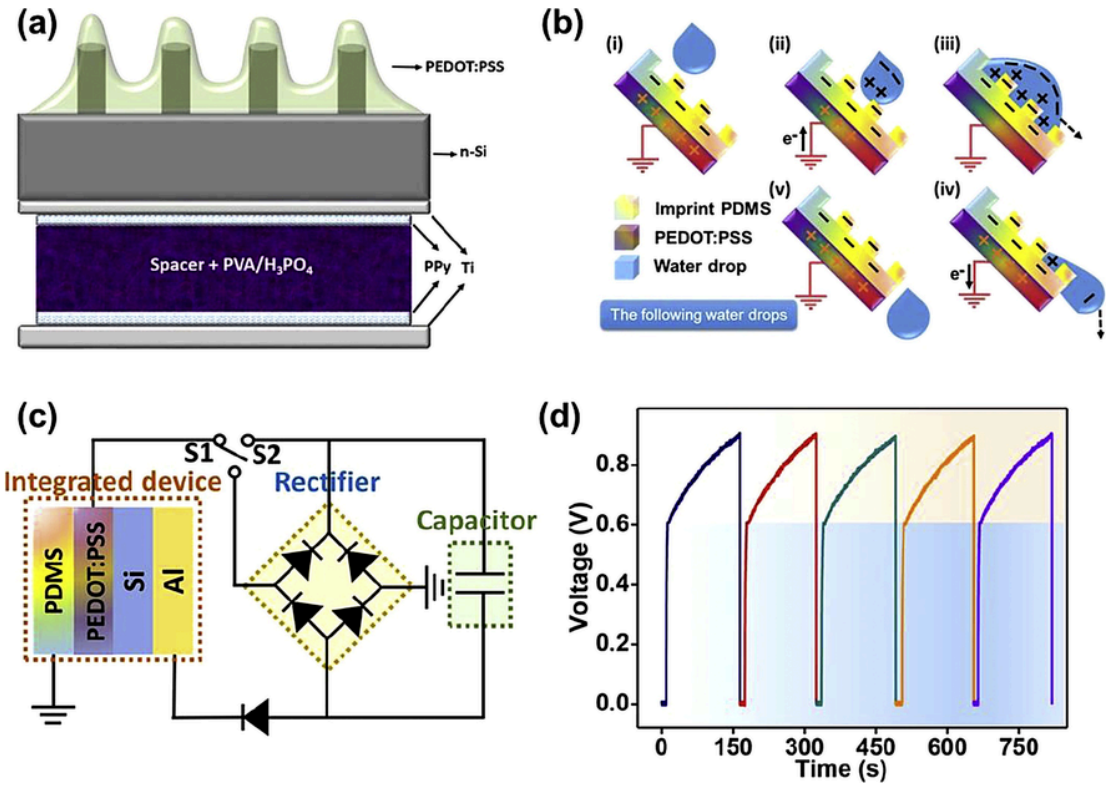

Fig. 21. (a) Schematic of a self-charging device contained a Si/PEDOT:PSS solar cell and a supercapacitor. Reprinted with permission from ref. [406]. Copyright 2017, American Chemical Society. (b) Working mechanism of a triboelectric nanogenerator. (c) Circuit diagram of the power system integrated with a Si/PEDOT:PSS solar cell and a triboelectric nanogenerator. (d) Voltage-time curves of a capacitor charged by a power system. Reprinted with permission from ref. [407]. Copyright 2018, American Chemical Society.

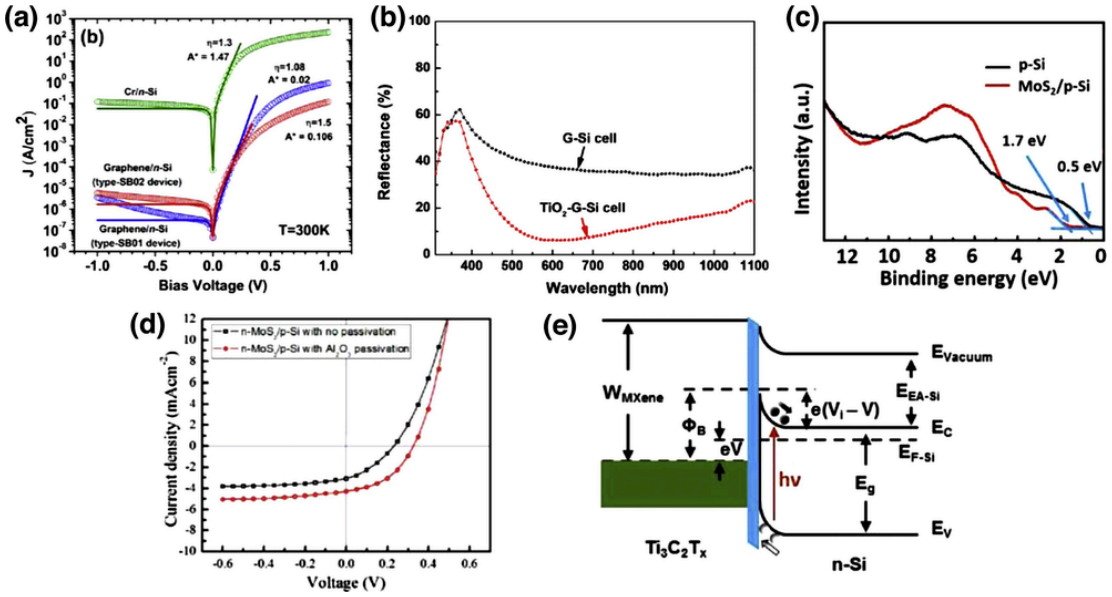

Fig. 22. (a) Current-voltage characteristics of graphene/Si Schottky junction diodes. Open circles and solid lines are measured and fitted current-voltage characteristics, respectively. A* is the effective Richardson constant. Reprinted with permission from ref. [413]. Copyright 2014, American Chemical Society. (b) Current-voltage curves in the dark condition. Reprinted with permission from ref. [417]. Copyright 2013, American Chemical Society. (c) Energy difference between the Fermi level and valence band maximum. Reprinted with permission from ref. [423]. Copyright 2014, American Chemical Society. (d) Current-voltage curves of MoS_2/Si heterojunction solar cells. Reprinted with permission from ref. [425]. Copyright 2016, American Chemical Society. (e) Energy band diagram of $Ti_3C_2T_x/SiO_2$/Si heterojunction. Reprinted with permission from ref. [428]. Copyright 2019, Wiley-VCH.

cal passivation from the SiO_2 layer, the Al_2O_3 layer was deposited onto MoS_2 films to realize the field-effective passivation and traps elimination. After incorporating Al_2O_3 layers, the PCE improved to 5.6% (Fig. 22 (d)) [425]. Additionally, a new class 2D material of transition metal carbides and carbonitrides (MXenes) [426,427] is proved to be an alternative forming a heterojunction with Si. Shapter and coworkers transferred a layered MXenes, $Ti_3C_2T_x$, onto n-type Si surface, forming a $Ti_3C_2T_x$/Si heterojunction solar cell with a PCE of 4.2%, as shown in Fig. 22 (e). To enhance the charge collection and light utilization, chemical doping and antireflection technologies were applied, and a PCE approaching 11% was achieved in $Ti_3C_2T_x$/Si heterojunction solar cells [428].

5. Tandem devices based on Si heterojunction solar cells

Over the decades there has been a steady improvement in device efficiency as well as a continuous decline in LCOE. To further improve the competitiveness of PV in the energy market, a lower LCOE is necessary, which can most effectively be achieved by boosting efficiency. Based on the heterojunction IBC structure, Yoshikawa et al. made a large area c-Si solar cell with an efficiency of 26.7% [14] that is approaching the theoretical efficiency limit (29.4%) of single-junction c-Si solar cells [429]. Any further improvement in efficiency will be significantly challenging. According to the R&D roadmap of c-Si solar cells (Fig. 1), tandem devices will be the inevitable next step for ultrahigh efficiency PV production. In this chapter, we will review the development status of tandem devices based on a c-Si bottom cells, mainly including perovskite/c-Si and III-V/c-Si tandem solar cells.

5.1. Perovskite/Si tandem solar cells

5.1.1. Tandem architectures

The rapid efficiency improvement of the perovskite solar cells has made >30% efficiency viable at a significantly lower cost than other materials such as GaAs [430]. There are two main streams for the design of tandem solar cells: two-terminal (2T) and four-terminal (4T) architectures as shown in Fig. 23. For 2T design, the top and bottom cells are connected in series, therefore only two external contacts are required and only the top contact needs to be transparent. The 4T design requires two sub-cells to be fabricated on two separate substrates, and physically stacked on top of each other. Therefore, the top cell must be semi-transparent, and four external electrodes are required, of which three must be transparent.

Compared with the parasitic absorption loss from two extra transparent electrodes of 4T architectures, a 2T device may have some efficiency advantage. However, the fabrication of 2T devices creates more technological challenges in terms of materials and device structures. For example, high-temperature annealing processes that are required for some inorganic carrier selective contacts can be detrimental for the passivation and contact quality of the bottom sub-cell. Furthermore, in a 2T configuration, the sub-cells are connected in series. According to Kirchhoff's law, the current flow through both cells must be matched, which means the photocurrent is determined by the sub-cell with a lower current output. Hence, the optical properties of the 2T device must be carefully manipulated to balance the current output from both sub-cells. Due to the geographical and temporal variations in the solar spectrum, the current output of the sub-cells could be substantially mismatched, and the device performance may be impacted. Hörantner and Snaith investigated in detail of this impact on 2T tandems [431]. They concluded that the optimum cell parameters – in particular, top cell thickness and bandgap – will vary somewhat with the geographical region in which the cells will operate. Provided that these parameters are optimized, then 2T tandems can deliver significant performance improvements. They conclude that the drive towards 2T tandems is justified. The progress in 2T perovskite/c-Si tandem devices is rapid. With careful implementation, perovskite and c-Si devices can be great partners for future commercialization to further bring down LCOE and make PV system more competitive in the energy market [432]. In 2018, a 28% certified efficiency was reported by Oxford PV on a 1 cm^2 device [433]. Recently, the efficiency was further boosted by HZB to 29.15% [19]. An overview of the efficiency evolution of perovskite/c-Si tandem devices is summarized in Fig. 24.

5.1.2. Homojunction c-Si sub-cell

The first presented monolithic perovskite/c-Si device was based on a homojunction c-Si bottom cell [434]. Mailoa et al. reported a per-

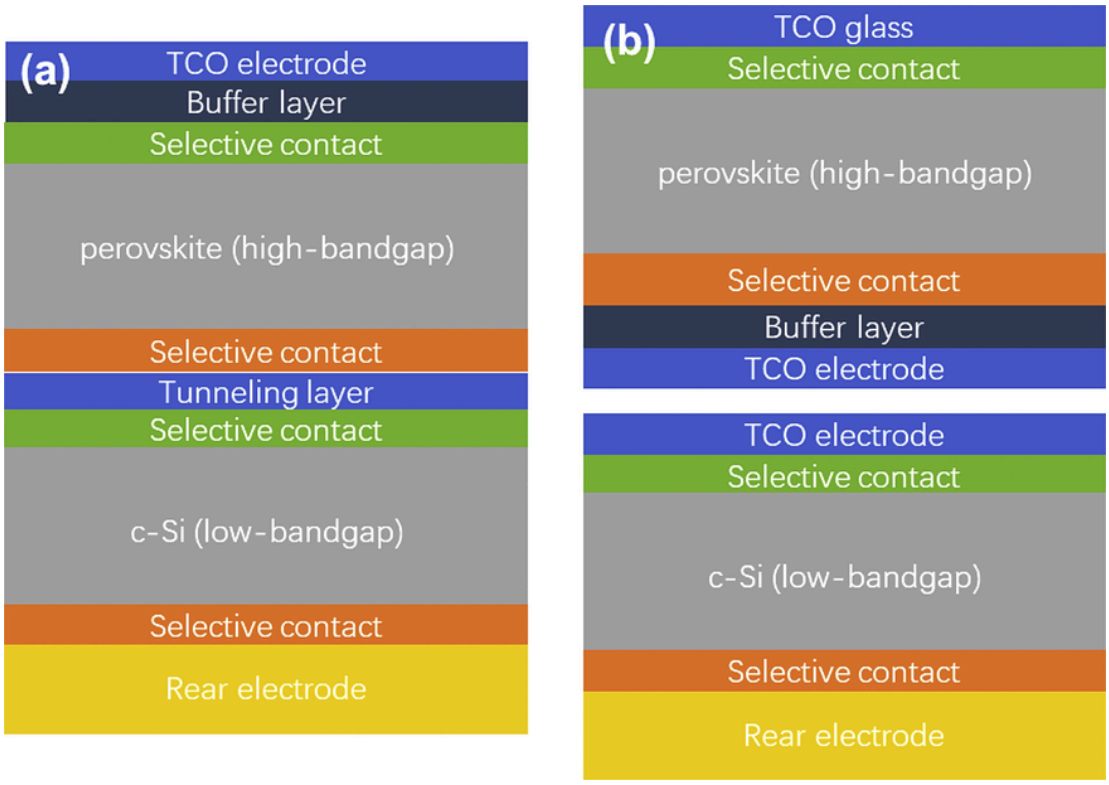

Fig. 23. Tandem configurations with varying degrees of electrical/optical independence. (a) 2 T series-connected tandem and (b) 4 T tandem with independent electrical connection to both cells.

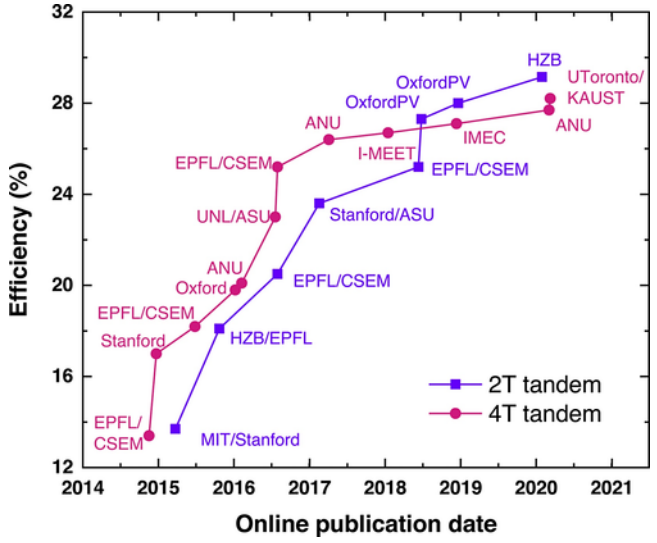

Fig. 24. Efficiency evolution of the 2 T and 4 T perovskite/c-Si tandem device. Data were from references [19,434–440] (2 T) and [441–452] (4 T). Massachusetts Institute of Technology (MIT) in America, Helmholtz-Zentrum Berlin für Materialien und Energie GmbH (HZB) in Germany, École Polytechnique Fédérale de Lausanne (EPFL) in Switzerland, Centre Suisse d'Électronique et de Microtechnique (CSEM) in Switzerland, Arizona State University (ASU) in America, University of Oxford (Oxford) in UK, Australian National University (ANU) in Australian, University of Nebraska-Lincoln (UNL) in America, Institute of Materials for Electronics and Energy Technology (I-MEET) in Germany, Interuniversity Microelectronics Centre (IMEC) in Belgium, University of Toronto (UToronto) in Canada, King Abdullah University of Science and Technology (KAUST) in Kingdom of Saudi Arabia.

ovskite/c-Si tandem solar cell with an efficiency of 13.7% in 2015. The front of the Si sub-cell was a full area heavily boron-doped emitter, while the rear side featured a standard full-area BSF structure. A heavily doped n-type a-Si:H layer was deposited between the two sub-cells and acted as a tunneling layer for the tandem device as shown in Fig. 25 (a). In addition to the fact that the efficiency of the perovskite top cell was still relatively low at that time, the device performance was limited for two chief reasons. Firstly, the bottom c-Si solar cell lacked good surface passivation layers. Secondly, the tandem structure resulted in large parasitic absorption losses. Despite these limitations, this pioneering work demonstrated the principle of 2 T perovskite/c-Si tandems.

Werner et al. chose zinc doped tin oxide (ZTO) as a recombination layer between sub-cells (Fig. 25 (b)). Combined with a rear surface passivation layer of SiO_2 and anti-reflection foil, the J_{SC} was boosted to over 15 mA/cm^2 and a PCE of 16.3% was realized [453]. However, the front side of the c-Si sub-cell still lacked passivation. After that, Wu et al. presented an innovative design for a monolithic perovskite/Si tandem solar cell, as shown in Fig. 25 (c), featuring a mesoscopic perovskite front cell and a high-temperature tolerant homojunction c-Si rear cell [454]. A Cr/Pd/Ag metal *via* array was placed between ITO and p-type doped front surface to decrease the resistive loss but enable a front surface passivated by Al_2O_3/SiN_x stack. The improved temperature tolerance of the c-Si bottom cell permits significantly increased flexibility in the design and fabrication of the perovskite cell. Consequently, a steady-state efficiency of 22.5% and a V_{OC} of 1.75 V were achieved on a 1 cm^2 tandem solar cell.

5.1.3. Heterojunction c-Si sub-cell

Monolithic tandem devices using SHJ solar cells as bottom cells have found widespread appeal. SHJ cells have achieved high efficiencies, which is a precondition enabling efficient tandem solar cells. Meanwhile, since SHJ devices feature full area passivating contacts, the interface architecture between the two sub-cells is significantly simplified. The drawback of SHJ cells for tandem applications is their limited temperature stability. The front cell must be processed at a temperature of less than 250 °C because SHJ cells' performance would be de-

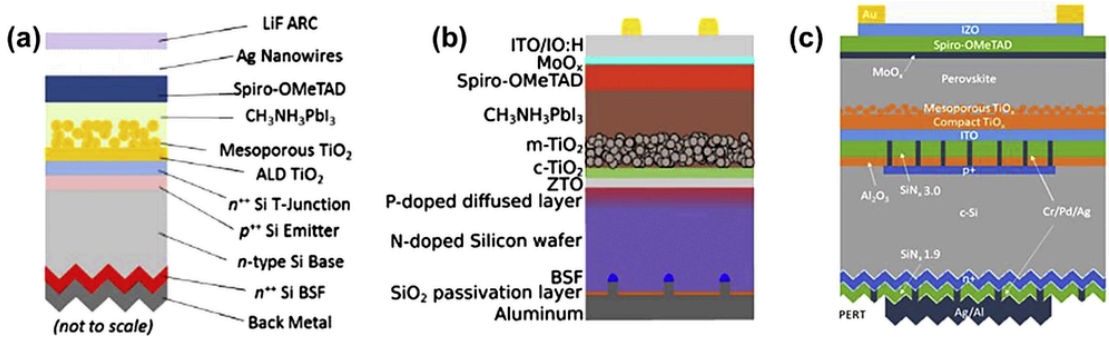

Fig. 25. Schematics of perovskite/c-Si monolithic tandem structures based on homojunction c-Si bottom device. (a) Reprinted with permission from ref. [434]. Copyright 2015, The American Institute of Physics. (b) Reprinted with permission from ref. [453]. Copyright 2016, The American Institute of Physics. (c) Reprinted with permission from ref. [454]. Copyright 2017, The Royal Society of Chemistry.

graded due to hydrogen escaping out of the a-Si:H passivation layer if overheated [10].

To avoid the degradation of bottom c-Si cells caused by high-temperature processes, Albrecht et al. applied a low-temperature ALD technology to grow a tin oxide (SnO_x) electron transporting layer (ETL) on a-Si:H, as shown in Fig. 26 (a). Meanwhile, a MoO_x buffer layer was deposited onto perovskite materials to protect and minimize the damage caused by ITO sputtering. Finally, a PCE of 18.1% was achieved in perovskite/Si tandem solar cells. Additional to this, a low-temperature solution-processed SnO_x was also introduced into perovskite/Si tandem solar cells and a PCE of 20.57% was obtained [455]. Werner et al., on the other hand, using PCBM instead of SnO_x for the ETL, realized a PCE of 21.2% using light management engineering [436].

Targeting a better bandgap match and higher stability, Bush et al. chose a Cs-FA (formamidinium) based perovskite material in tandem structures (Fig. 26 (b)) [437]. Several functional materials including LiF, PCBM, SnO_2, ZTO, and ITO were used as front ETLs and electrode, which not only realized a balance of electrical and optical properties but also minimized shunting path. To improve the Lambertian scattering and further reduce the parasitic absorption losses in the infrared region, Si surface texture technology and a Si nano-particle (SiNP) layer were introduced. Finally, a certified efficiency of 23.6% was achieved in a perovskite/c-Si tandem solar cell. Most recently, Sahli and co-workers reported a 25.2% efficient tandem device with a J_{SC} of 19.5 mA/cm^2. A critical design feature, in Fig. 26 (c), is a conformal structure of hole transporting layer (HTL), perovskite, ETL and front TCO layers on top of the textured c-Si wafer deposited through PVD and solution methods. Meanwhile, a double-sided textured c-Si substrate enabled a further significant reduction in reflection losses [438].

5.1.4. *Interconnection free and reversed TOPCon*

The first interconnection free perovskite/c-Si device was prepared by Zheng et al. in which the device used a homojunction bottom cell without front passivation [456]. Instead of using TCO as the recombination layer, a SnO_2 layer was directly deposited on top of the heavily boron-doped c-Si surface to form an ohmic contact between two sub-cells. The omission of the conventional recombination layer not only reduces the additional parasitic absorption and processing steps, but also provides significantly better shunt tolerance of the top cell due to the low sheet resistance at the interface between sub-cells. To further prove the point, Zheng et al. fabricated 16 cm^2 tandem devices, where the perovskite layer was fabricated with an anti-solvent method and achieved 21.8% efficiency [457]. Meantime, Shen et al. developed an interconnection free structure using ALD deposited TiO_x as the ETL of the perovskite top cell [458]. The device efficiency was further boosted to 24.2% by passivating the c-Si front surface with an ultra-thin SiO_2 and poly-Si layer, which could be considered a reversal of the so-called 'TOPCon' structure that was developed by Feldmann et al. to passivate the rear of c-Si cells [176]. Since the poly-Si passivating contact was prepared at a high-temperature of over 700 °C, the stack can sustain its passivation quality during the following high-temperature processes for the perovskite solar cell deposition. The process requires neither pho-

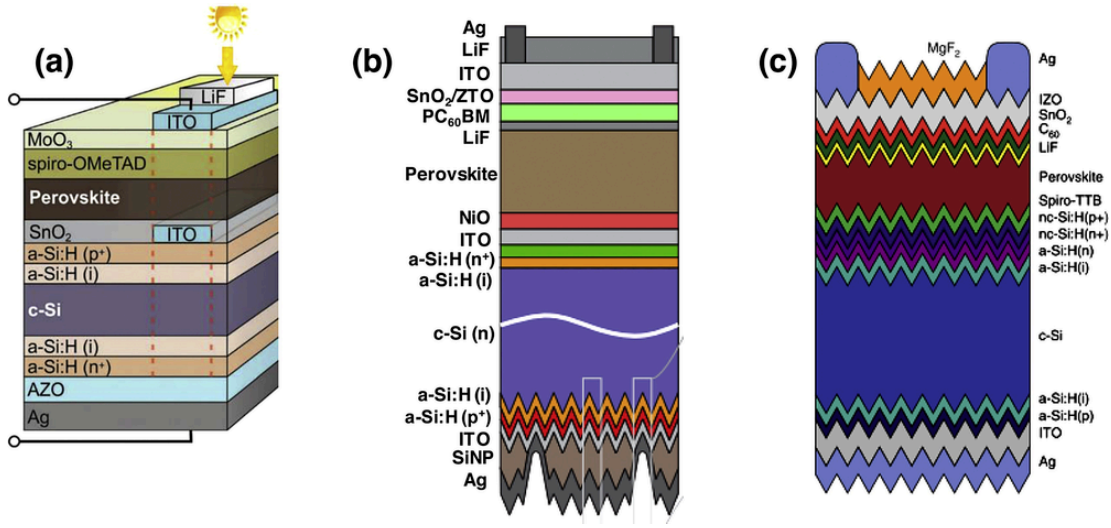

Fig. 26. The schematic drawing (not to scale) of the evolution of perovskite/c-Si monolithic tandem developed based on heterojunction c-Si bottom device, (a) Reprinted with permission from ref. [435]. Copyright 2016, The Royal Society of Chemistry. (b) Reprinted with permission from ref. [437]. Copyright 2017, Springer Nature. (c) Reprinted with permission from ref. [438]. Copyright 2018, Springer Nature.

tolithography nor laser contact opening and can be readily fabricated in industry. Importantly, the optimized simulation demonstrated that this 'reversed TOPCon structure with the same generation profile can achieve 11.84% efficiency compared to 12.34% obtained with an SHJ structure for the bottom cell, which is close but still 0.5% behind [459]. Additional to the PERC and the reversed TOPCon structure bottom cell, Nogay et al. presented a bottom cell structure can in principle tolerate the high temperature annealing process. The front and rear surfaces were capped by SiO_2/doped SiC_x stack for passivation and charge extraction. However, the top perovskite sub-cell is processed with low temperature [460].

5.1.5. Mechanical stacking

For a typical 2T tandem device, the cell with the wide bandgap is monolithically grown on top of the narrow bandgap one. In contrast, in the mechanical stacking approach, both top and bottom cells are fabricated individually, which lifts several competing limitations for fabrication. This method was developed to increase the yield of tandem devices since screening both sub-cells can potentially be completed prior to the bonding process. On the other hand, the most significant disadvantage of this structure is the need for at least one additional TCO layer, while in some cases, both intermediate TCO layers need to be sufficiently thick to avoid lateral resistive loss.

The use of transparent adhesive provides a simple method to achieve mechanical stacking through direct bonding of the top and bottom cells. Electrically conductive particles could be incorporated to connect both cells in series. The concept of using a transparent conductive adhesive (TCA) layer to bond multijunction devices was first developed by Sameshima et al., where a SHJ c-Si cell and an a-Si:H thin-film cell were bonded together by a polymide-ITO adhesive layer [461]. Recently, this concept was adapted to the perovskite/c-Si 2T tandem structure. A perovskite solar cell and a SHJ c-Si solar cell were fabricated separately and then bonded with a PEDOT:PSS-sorbitol layer realized a PCE of 21% on this particular stack [462]. Silver-coated PMMA microspheres are another candidate for intermediate contact and have been used in the III-V/Si tandem structure previously [463]. Owing to its micro-scale size, the TCA layer can be easily accommodated on a planar/textured surface and offers improved optical performance compared to a planar structure. An efficiency of 19.4% was achieved for the perovskite/c-Si tandem [464]. More recently, a 25.9% efficiency was achieved by stacking the semi-transparent top cell directly on top of the bus bar of the bottom c-Si cell, but the lack of light management between the bottom and top devices largely increase the reflection loss [465].

5.1.6. Light management

5.1.6.1. Anti-reflection Minimizing the reflection loss is one of the key challenges in achieving efficient tandem devices. The reflection losses stem from the interfaces with a large mismatch of the refractive index. Texturing the front surface is the most effective way to avoid such losses. The pyramid structure at the front surface allows the light that is reflected to be absorbed for the second time. With an additional layer of MgF_2 or LiF as the anti-reflection (AR) coating, reflection losses can be reduced to less than 2% [434,435,437,438]. Due to the fabrication complexity of evaporating a conformal perovskite layer on top of the textured surface, many researchers on 2T tandems are still focused on the deposition of the perovskite cell on the polished side of c-Si solar cells. Chen et al. and Hou et al. recently showed that solution-processed perovskite films can be deposited onto sub-micron sized pyramids [466,467]. At the front surface, an AR foil is still required for best results. The foil that offers a broadband AR effect was typically made by pouring polydimethylsiloxane onto the textured Si wafer before curing and then separating from the wafer [468,469]. This AR strategy has been widely used in the perovskite/c-Si solar cells [470,471]. Intriguingly, rose petals were also shown to be a useful mould for fabrication of AR foils [456,472,473].

Since perovskite solar cells constitute several thin films, optical modeling is required to design efficient devices [474–477]. The optical properties (refractive index and extinction coefficient) of common materials in perovskite solar cells are available. However, to acquire accurate optical modeling results, it is still strongly encouraged to independently characterize the fabricated films since the change in fabrication conditions can dramatically influence their optical properties. A significant mismatch of the refractive index between the thin films should be avoided to reduce the reflection loss. For example, optimizing the interconnection layer is useful to increase the carrier generation of the bottom cell. Conventionally, TCOs were commonly used as the interconnection of tandem devices, due to their relatively low refractive index compared to c-Si, and cannot be less than 20-nm-thick for good electrical property [436]. One approach is to get rid of the TCO layer by using the interconnection free structure, which has been successfully demonstrated using solution-processed SnO_2 or ALD deposited TiO_x on top of the c-Si [456,458]. Additionally, the TCO layer can be replaced by either a nc-Si:H(p^+)/nc-Si:H(n^+) stack [470] or an additional optical buffer layer (Si-rich SiN_x [454] or nc-SiO_x:H layer [478]) between the TCO and the c-Si. This strategy has been shown to significantly suppress parasitic reflectance compared to a TCO recombination layer. Nevertheless, to achieve the least reflection loss on a planar structure, extremely careful choice of the functional layers (both thickness and optical properties) together with an AR foil is required, which may not be practical for commercialization.

Another optical loss arises from the escape of long-wavelength photons out the rear side (following rear reflection). An effective light trapping system, namely a Lambertian scattering rear surface, can effectively increase the absorption of long-wavelength photons in tandem solar cells [474]. Werner et al. demonstrated that rear side scattering can be improved through rear side texturing. Bush et al. also demonstrated SiNP layer on the rear side could further enhance the infrared light collection [437,447]. Regardless of the texturing or non-texturing structure, the c-Si bottom cell in tandem architectures experiences higher long-wavelength optical loss (as a percentage of total incident light) than in conventional single-junction cells. As a result, the optimum wafer thickness (for highest device PCE) will be thicker for tandem devices than that for conventional cells [459].

5.1.6.2. Minimizing the parasitic absorption The front transparent electrode plays a key role in tandem device performance. Owing to the very limited conductivity of the ETL or HTL on top of the perovskite solar cell, a transparent conducting layer as a top electrode that facilitates lateral charge conduction is indispensable for the tandem device. As a result, parasitic absorption from the top electrode is inevitable. To realize a low parasitic absorption and a high conductivity, the top electrode must have relatively low carrier density, but high mobility. ITO with good transparency and conductivity is the most widely used electrode material. However, due to restriction on the processing temperature, the ITO deposition cannot be either in-situ or post annealed beyond 150 °C, hence the optimal optical and electrical performance cannot be reached [479,480]. A room temperature sputtered amorphous indium zinc oxide (IZO) layer was developed to overcome the issues. The film displays a significantly higher charrier mobility ~50 cm^2/Vs compared with that of ITO of ~10 cm^2/Vs [443]. With a similar range of carrier concentration, the thickness of this layer can be reduced to suppress the parasitic absorption at the infrared region in particular. Meanwhile, indium hydrogen oxide (IOH) with mobility of 130 cm^2/Vs was achieved in semitransparent perovskite solar cells [481]. Unfortunately, a 200 °C annealing process limits its application for the current tandem solar cells. [482] Alternatively, silver nanowires (AgNWs) and graphene have also attracted attention. AgNW electrodes can be deposited on top of perovskite films by mechanical transfer or solution technologies while achieving excellent transmittance and conductivity [442,483,484]. However, Ag can easily react with any halide components escaping from the perovskite materials to form an insulating layer of AgI that blocks charge extraction [485,486]. Graphene is

not an adequate material for use as a transparent electrode for any solar cell, since it absorbs significantly over the full spectrum, and shows a large sheet resistance [487].

Eliminating the parasitic absorption caused by the buffer layer is also important to device performances. For the n-i-p structure perovskite top cell, MoO_x is a common buffer layer before sputtering TCO on top of the organic hole transport layer. MoO_x can form a uniform and compact layer through a facile method, which prevents the potential damage to perovskite absorbers and especially for the device involves high-temperature sensitive organic layers, *e.g.* Spiro-OMeTAD [488]. However, MoO_x can absorb incident light [489]. Aiming to minimize the parasitic absorption loss, Duong et al. reduced the thickness of the MoO_x layer from 10 to 5 nm in a 4 T tandem device [451]. A 1-nm-thick Ag layer was also studied to achieve similar effects [490]. As for tandem devices with a p-i-n structure perovskite top cell, the buffer layer is generally deposited on top of C_{60} or PCBM. These fullerene displays improved thermal stability compared with Spiro-OMeTAD, providing more options for designing tandem solar cells. A solution-processed method for this buffer layer was developed by spin-coating AZO nano-particle on top of the PCBM layer [491]. A pulsed-CVD deposited SnO_2 layer developed by Bush et al. by far is the most commonly used buffer layer for the p-i-n structure [437]. With polyethylenimine ethoxylated (PEIE) functionalizing the surface of the fullerene electron transport layer, a denser, continuous and fast-growing SnO_2 film can be obtained, which acts as a buffer layer that protects the underlying organic transport and perovskite layers from sputter damage as well as the penetration of water [492]. Removing the buffer layer is a straightforward way to eliminate parasitic absorption loss. Controlling the sputtering process can avoid sputtering damage, which means a buffer layer can be removed [493,494].

Additionally, charge transport layers (HTL or ETL) lead to a parasitic absorption loss. Spiro-OMeTAD, one of the most widely used HTLs in n-i-p perovskite solar cells, has a high extinction coefficient at short wavelengths [475], caused typically current losses of 2-3 mA/cm^2 [454,474]. For good electrical performance, the thickness of the Spiro-OMeTAD layer typically needs to be over 100 nm, which makes it is difficult to reduce the parasitic absorption loss significantly. For tandem solar cells with a p-i-n perovskite front cell, fullerene-based materials such as C_{60} [495]. PCBM [496] and ICBA [497] are commonly used as the ETL. Fullerene materials have a similar high extinction coefficient compared with that of Spiro-OMeTAD. However, these materials can be deposited by a thermal evaporation process and the thickness of these ETLs can be reduced to 15-20 nm [438,498]. The parasitic absorption loss can be reduced to ~1 mA/cm^2, but still a significant room for further reduction [499]. Up to now, for tandem device fabricated on top of the planar c-Si bottom cell, the highest reported J_{SC} for p-i-n structure is 19.02 mA/cm^2, whereas the n-i-p counterpart is 17.8 mA/cm^2. Choices for the HTL in the n-i-p structure can be PTAA [500] or P3HT [501] if these polymer HTLs can be uniformly deposited on top of the perovskite layer with significantly reduced thickness (< 20 nm). Inorganic HTLs such as NiO_x [502] and CuSCN [503] can be used if the deposition techniques are compatible with the perovskite layer.

5.1.7. *Wide bandgap perovskite materials*

The purpose of developing tandem devices is to minimize the thermalization losses of high energy photons and reach higher spectral response as shown in Fig. 27 (a). To match well with bottom c-Si solar cells, high utilization of the solar spectrum above the perovskite bandgap is critical for the perovskite solar cells [504]. The metal halide perovskites are outstanding materials for fabricating PV devices, owing to their direct bandgap, excellent charge transport, sharp absorption band-edge and low parasitic absorption. Furthermore, the tunable bandgap between 1.15 and 3.06 eV provides perovskite materials with a promising opportunity for tandem applications [505]. Computational simulation elucidated that the origins of the band tunability strongly correlates with the largest metal-halide-metal angle [506]. $MAPbI_3$ with a bandgap of ~1.56 eV was the first perovskite material that realized notable PV performances [507,508]. The optimum theoretical bandgap for a single-junction device is in the range 1.1 to 1.3 eV [509

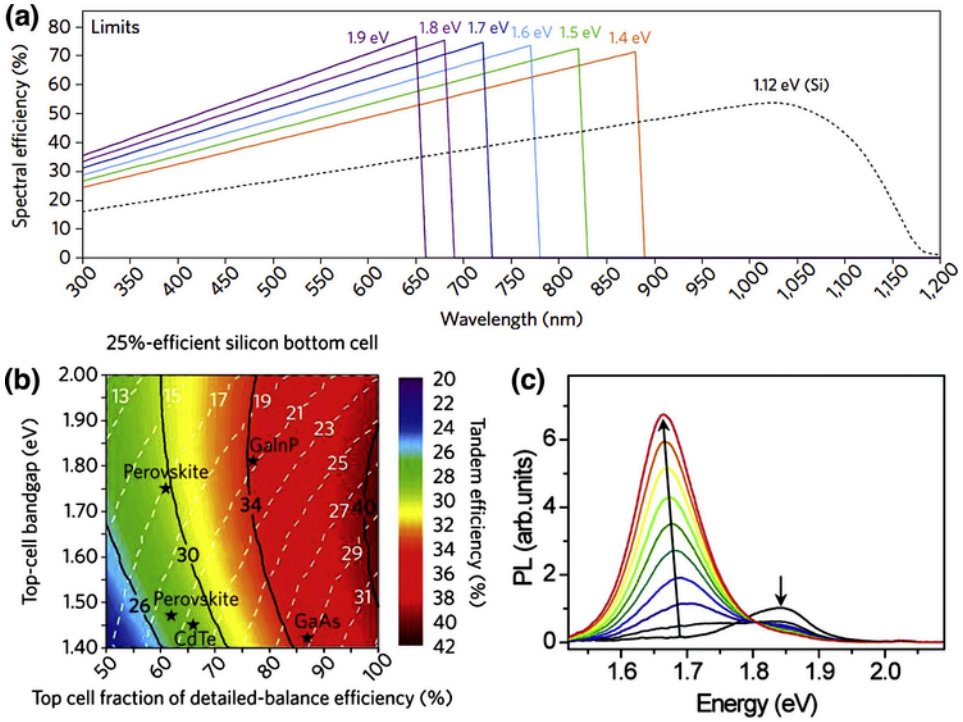

Fig. 27. Guide for predicting the maximum possible efficiency of a Si-based tandem as a function of the top-cell bandgap and efficiency. (a) Limiting spectral efficiencies of ideal top cells. (b) Tandem solar cells with Si bottom cells. Reprinted with permission from ref. [504]. Copyright 2016, Springer Nature. (c) Photoluminescence (PL) spectra of a perovskite thin film over 45 s in 5 s increments under 457 nm, 15 mW cm^2 light at 300 K. Reprinted with permission from ref. [512]. Copyright 2015, The Royal Society of Chemistry.

], while the optimum bandgap for a top sub-cell in dual junction tandem solar cell is between 1.7 to 1.75 eV as shown in Fig. 27 (b) [504]. Recent studies showed bifacial 2 T tandem structures can boost the yield compared with monofacial structures (default is monofacial structures herein) [510], whereas the optimum bandgap range can be dropped to as low as 1.63 eV [511]. Hence, it is necessary to tailor the composition of the perovskite material for better device performance.

Halide metal perovskite cells have achieved a high photon utilization; however, FF and V_{OC} still limit the output efficiency. One quantitative method of comparing the optoelectrical performance of PV devices with different materials is by calculating its V_{OC} deficit ($E_g/q - V_{OC}$). For the best performing GaAs and c-Si solar cells, the V_{OC} deficit is approximately 0.3 eV and 0.38 eV, respectively [13]. Although a V_{OC} deficit as low as 0.35 V and 0.38 V has been achieved for perovskites with a bandgap of 1.5 eV and 1.6 eV, respectively [513,514], wide bandgap perovskite solar cells still present a much higher V_{OC} loss [515].

Tuning the halide ratio between bromine and iodine is the most straightforward way of varying the bandgap [516], which has also been demonstrated in FAMA and Cs-lead-halide systems [517,518], and led to the successful realization of perovskite materials with a bandgap greater than 1.6 eV [448,519]. However, light soaking has been shown to cause partially reversible halide segregation (the Hoke effect [512]), where the perovskite segregates into iodide-rich lower-band-gap and bromine-rich higher-band-gap domains as shown in Fig. 27 (c). An electric field was also found to induce phase segregation in the dark [520]. Therefore, the phase these mixed halide perovskite layers are not stable under normal operating conditions, but instead separate into two materials with different bandgaps, resulting in a loss of performance. A prospect by Slotcavage et al. suggests that halide migration can be suppressed by reducing defect concentrations [521]. Via surface passivation [496,522], additive and solvent engineering [523–525], the quality of the bulk perovskite and interface has been improved impressively. However, the V_{OC} deficit is still around 0.45-0.5 V. Recent work by Gharibzadeh et al. achieved a V_{OC} of 1.31 V with 1.72 eV bandgap perovskites on a single-junction device, suggesting the possibility of achieving a higher efficiency for wide bandgap perovskite materials based solar cells [526].

The phase segregation effect shows a different onset depending on the ionic radius of the A-site cation. For $FAPb(Br_xI_{1-x})_3$, $MAPb(Br_xI_{1-x})_3$ and $CsPb(Br_xI_{1-x})_3$, the lowest bandgap for phase segregation are 1.52 eV, 1.7 eV and 1.9 eV, respectively. Although $MAPb(Br_xI_{1-x})_3$ can provide an ideal bandgap for tandem applications, its thermal instability is poor and the intrinsic acidic property of the A-site organic cation (MA) raises further stability issues [527–529]. Incorporation of Cs and FA is a feasible method to solve these issues. Replacing MA with FA alone, the perovskite film still shows significant phase segregation under long term illumination [530]. However, after adding Cs^+ into the A-site cation, the phenomenon can be significantly suppressed [444], with perovskite compositions with both increased Cs and Br fractions showing improved phase stability [519]. Xu et al. recently demonstrated that alloying chlorine into the perovskite lattice can shrink the lattice parameter. Negligible phase segregation was observed even at 100-sun illumination intensity and a PCE of 27% was achieved in a 2 T tandem solar cell [498].

$CsPbI_3$ with a bandgap of ~1.7 eV is an alternative semiconductor to fabricate wide bandgap perovskite for perovskite/c-Si tandem solar cells. Especially, $CsPbI_3$ based perovskites avoid the volatility of organic cations. Meanwhile, the property of single halide composition eliminates the problem of halide phase segregation. However, α-$CsPbI_3$ (black phase) is thermodynamically unstable and would change to more stable δ-$CsPbI_3$ (yellow phase) under ambient conditions [531]. Various strategies have been demonstrated to enhance the phase stability, including surface modification [532,533], crystal growth control [534], additive incorporation [535,536], and strain engineering [537]. Up to now, over 17% efficiency has been achieved with a significantly enhanced ambient stability [532].

5.2. Ultrahigh efficiency III-V/Si tandem devices

Multijunction solar cells offer the only proven pathway to exceeding the single-junction detailed balance limit of 33% efficiency at one sun. In a multijunction or tandem solar cell, the top cell(s) provide the bulk of the power generation since they have a wider bandgap and thus absorb high energy photons and convert them to electricity at (ideally) a higher voltage than the bottom cell. Since Si provides a bottom cell with excellent conversion efficiency and voltage, the constraints on top cell(s) are strict; a relatively poorly performing top cell will simply parasitically absorb light that would be better used in the Si cell alone. This effect can be captured quantitatively in the spectral efficiency, which is a measure of the wavelength-resolved efficiency of a PV material [504]. Any top cell must have a higher spectral efficiency than the Si bottom cell in some wavelength range if there is any hope that a tandem configuration will improve the overall efficiency of the device. For this reason, only two types of top cell materials have been used to demonstrate higher efficiency tandems than can be achieved with a single-junction Si cell alone: perovskites, discussed in the last section; and III-Vs, which will be discussed in this section.

III-V materials provide the highest demonstrated PV efficiencies across all configurations, from single-junction GaAs (29.1% one-sun efficiency) to six-junction cells (47.1% efficiency under concentration) [13]. Thus, it is not surprising that the highest hybrid tandem efficiencies (combining dissimilar materials) are achieved on III-V/c-Si devices. The primary challenge in combining III-V and Si technologies is the integration of the materials without performance losses. There are three primary approaches to integrate III-V/c-Si tandems: (1) direct growth of III-V materials on a Si bottom cell, (2) wafer bonding of III-V and Si sub-cells, or (3) mechanical stacking of III-V and Si devices using an adhesive. All the three approaches rely on high-efficiency Si heterojunction bottom cells, either SHJ technology or poly-Si CSPCs discussed in Section 3. Each of these has advantages and disadvantages, discussed below, which are closely linked to the desired operational mode of the ultimate tandem, *i.e.* the number of electrical terminals.

5.2.1. Multi-terminal tandems

2 T III-V/c-Si tandems are the most traditional approach, where sub-cells are connected in series (typically using a tunnel junction), providing a simple but higher efficiency replacement for a single-junction cell. However, 2 T III-V/c-Si tandems must be current matched, which constrains the choice of top cell bandgap and thickness for optimal overall performance, as shown in Fig. 28 [538]. A 2 T III-V/c-Si tandem displays a maximum efficiency that is strongly dependent on top cell bandgap, and the location of that maximum changes with spectral conditions. In contrast, a III-V/c-Si 4 T tandem has electrically isolated sub-cells which can each be run separately at their maximum power point, yielding significantly reduced sensitivity to top cell design. This means that a very wide range of top cell bandgaps can be considered. The highest efficiency III-V/c-Si two-junction tandem (with a one-sun efficiency of 32.8%) uses GaAs as a top cell [20], which is extremely far from the 2 T maximum; this shows that top cell performance and quality matter much more than bandgap for III-V/c-Si 4 T cells. Thus, III-V/c-Si 4 T cells offer the greatest design flexibility. However, a disadvantage is that 4 T cells require lateral current extraction from between the two sub-cells (metal grids or a transparent, conductive oxide), which can introduce significant optical losses [539].

A less studied option uses three instead of four terminals [540,541]. In this three-terminal (3 T) approach, IBC Si cells are connected using an electrically conductive interconnection (*e.g.*, tunnel junction) to a III-V top cell. As with a 4 T tandem, there are now two electrical circuits, which enable operation in a current-mismatched mode and thus a similar maximum efficiency potential as 4 T tandems [542]. How-

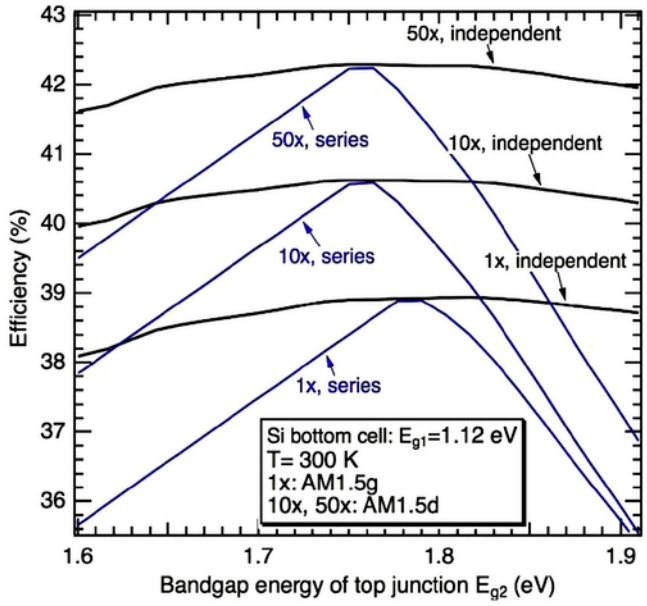

Fig. 28. Calculated efficiency of 2 T (series) and 4 T (independent) III-V/c-Si tandems as a function of top cell bandgap, shown for different optical. Reprinted with permission from ref. [538]. Copyright 2015, Elsevier.

ever, these two circuits can interact, which makes the device physics more complex [540,542]. Robust reporting of 3 T efficiencies is not yet widespread in the literature due to the complexity of interactions between the two circuits [540], and there is not yet an established cell certification method. The maximum efficiency (uncertified) that has been reported thus far is 27.3% for a GaInP/Si cell [543] – lagging behind the best 4 T GaInP/Si cell, at 32.5% efficiency [20] – however, the efficiency potential for 3 T tandems is higher because of the potential for reduced optical shading losses. There is also a multitude of different possible 3 T device configurations and top cell stacks possible, which simulations show provide options for exceeding 30% efficiency, *e.g.*, using either an isotype or tunnel junction interconnect polarity [540]. Different cell configurations are likely to present different practical challenges, and thus, more experimental work is needed to prove out these designs and push device efficiencies higher.

5.2.2. Direct Growth of III-Vs on Si

There has been extensive research on growing III-V semiconductors on Si substrates to enable two-terminal, monolithic tandems, among other desirable applications [544]. Since this process naturally results in an electrically conductive interface, it could in principle apply to either 2 T or 3 T configurations, although only 2 T has been demonstrated. Direct growth is in principle the simplest and least expensive integration method, since it leverages the low cost of Si wafers compared to GaAs and Ge, which are typically used for III-V cells. However, numerous technical difficulties have made this research topic a "grand challenge." The first challenge is antiphase domain free nucleation of a III-V material, typically GaP since it is lattice matched to Si, which requires double step surface reconstruction as described by Kroemer et al. [545] This has been achieved using two different *in situ* approaches and offcut Si wafers [546,547], but an open question in the field is how to achieve these results using solar-grade Si, which is not offcut or polished.

The second challenge to undertake in III-V/Si growth is lattice-mismatched epitaxy, since appropriate III-V top cell materials (GaAsP or GaInP) have a significantly larger lattice constant than Si, which induces dislocation formation as the epilayers relax. Metamorphic epitaxy has been introduced as a solution to this challenge, resulting in record efficiency III-V multijunction [548]. This approach has also been demonstrated on Si, resulting in cell efficiencies up to 20.1% for two junctions (GaAsP/Si) [13,549] and 24.3% for three junctions (GaInP/GaAs/Si) [13,550], but not yet exceeding the efficiency of the best single-junction Si cells alone (26.7%). These results are summarized in Fig. 29. A final challenge that faces these types of tandems, especially as cell sizes scale up, is the mismatch in thermal expansion coefficient, which can result in cracking of top cells [551].

5.2.3. Wafer bonding

Given the challenges associated with growing III-Vs on Si, the alternative approach of wafer bonding has also been used to fabricate III-V/Si tandems with conductive interlayers, with 2 T and 3 T devices demonstrated. In this approach, III-V sub-cell layers are grown on a GaAs or Ge substrate, and a Si sub-cell with a polished surface is prepared separately. These materials are joined under applied temperature and pressure to establish a bond, and then the III-V growth substrate is subsequently removed, leaving a thin III-V device stack on top of the Si cell. The two key challenges associated with this approach are surface roughness and achieving an electrically conductive bond. Surface smoothness is critical for wafer bonding, requiring polishing of the initial substrates and possibly even the epilayers post-growth. The interfaces must also be free of native oxides or other insulating layers to achieve sufficient electrical conduction. The most successful approach to surmount these challenges has been the use of "fast atom beams" to pre-treat the surfaces *in situ* before bonding, cleaning any residual oxides and activating the materials' surfaces to promote adhesion [555,556]. This process has resulted in extremely high cell efficiencies, up to 34.1% for triple-junction configurations (GaInP/AlGaAs/Si) [13,554] and 21.1% for dual junctions (AlGaAs/Si) [553].

A related, novel approach is the "smart stack" method, which uses an interlayer of metal nanoparticles (typically, Pd) in conjunction with wafer bonding to ensure electrical conduction between cells. This approach has been quite successful, with demonstrated efficiency up to 30.8% for a GaInP/AlGaAs/Si tandem [557]. Further, 3 T tandems have recently been demonstrated using this approach as well: a GaAs/Si cell was demonstrated, with the 3 T geometry enabling the use of a current-mismatched top cell (GaAs), which relaxes the constraints on top cell design [552]. Further work needed to enable continued advances in wafer bonded tandems mainly involve cost reduction: polishing is an expensive step [558], and these methods also require the use of a III-V substrate, which would need to be reclaimed in some way to recoup those costs [20]. However, the impressive efficiencies demonstrated us-

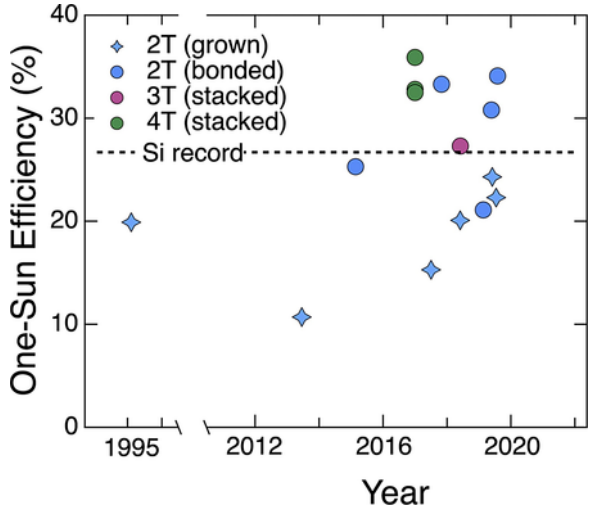

Fig. 29. Highest efficiency III-V/Si tandems at one sun using the approaches described here, including 2-junction and 3-junction devices. Data were from references [13,20,543,544,549–555].

ing wafer bonding prove that high-efficiency 2T III-V/Si tandems are achievable.

5.2.4. Mechanical stacks

The highest efficiencies have been achieved using mechanically stacked III-V/Si tandems, where III-V and Si cells are fabricated separately and then joined together using (typically, electrically insulating) glue, as shown in Fig. 30. In this approach, both cells can be fully optimized separately, without sacrificing cell quality to enable integration. One of the main benefits of mechanical stacking is that fully textured Si bottom cells can be used, which means existing, low-cost Si fabrication techniques can be leveraged and that optical absorption in the Si is optimized. However, a downside is that as with wafer bonding, III-V substrates are needed for top cell growth and thus substrate recycling is necessary to achieve competitive costs.

Historically, mechanical stacks resulted in 4T tandems due to the insulating nature of most optically transparent adhesives. 4T tandems (Fig. 30 (a)) have demonstrated the highest efficiencies, up to 32.8% using a GaAs top cell, 32.5% using a GaInP top cell, and 35.9% using a GaInP/GaAs tandem as a top cell [20]. However, recent advances in transparent, TCAs mean that mechanical stacking can now be used for conductive interconnects as well, resulting in 2T and 3T tandems [559,560]. An example device that uses this approach is shown in Fig. 30 (b), where a GaInP/Si TCA-bonded tandem was demonstrated with an efficiency of 27.3% [543]. Unlike wafer bonding, TCAs are compatible with textured Si bottom cells, which means that all the benefits of the mechanical stacking approach are retained while optical losses from lateral current extraction – the main downside of 4T tandems – are avoided. These materials and techniques are very new, and thus more research is needed to optimize materials and processing so that efficiencies reaching or exceeding 4T records can be demonstrated [504].

6. Summary and outlook

Herein, we present a comprehensive review covering all the aspects of Si heterojunction solar cells, from materials to devices, as well as their application for tandem devices. Although the diffusion-based homojunction Si solar cells, such as Al-BSF and PERC, dominates the PV market at the moment, Si heterojunction solar cells will be the next generation high-efficiency PV production. The efficiency of SHJ and Poly-Si CSPC solar cells has surpassed 26% owing to the successful structure design and theory development, demonstrating the high potential of Si heterojunction technology. Targeting a simplified fabrication process, the concept of dopant-free passivating contact (*e.g.* Si/metal compounds, Si/organic materials, and Si/2D materials) is intensively investigated and developed in the Si heterojunction community. Most of these carrier-selective contacts enable efficiencies over 20% and a champion efficiency of 23.5% has been realized. Meanwhile, tandem solar cells based Si heterojunction bottom cells, such as perovskite/Si and III-V/Si tandems, are being developed, targeting ultra-high efficiency over the theoretical limit of single-junction c-Si device (29.4%). The 35.9% efficiency of III-V/Si tandem solar cells has surpassed the theoretical limit of single-junction Si solar cells; the 29.1% efficiency of perovskite/Si tandem solar cells is also approaching the theoretical efficiency of single-junction Si solar cells. Although these notable achievements have been witnessed, the commercialization success of these Si heterojunction technologies as well as the tandem devices are still very challenging. Below, we outline possible research directions and challenges that have to be addressed for future development and commercialization.

1) SHJ solar cells are currently at the forefront of Si solar-cell research in terms of efficiency. Further improvements in terms of passivation/transparency/conductivity combinations for the contact stacks are expected to push to 27% the record single-junction Si efficiency limit. Commercialization is already happening, with major hurdles at the moment being the capital required for building a fabrication line. Reducing the cost of the main production tools, which is ongoing, is needed for further adoption. With the proven fabrication of high-efficiency device with minimal usage of indium and silver (or even their complete avoidance), there is no material resource limitation for a TW-scale production of Si heterojunction solar cells.
2) Solar cells with poly-Si alloy CSPCs have demonstrated record efficiencies at laboratory scale of 25.8% for FBC and 26.1% for IBC cell architectures. This technology shows potential for industry transfer when some challenges are addressed. Industrialization of those contact schemes especially requires the development of cost-effective metallization technique and the application of TCOs in case of thin poly-Si alloy layers. Among the various architectures developed so far, the PERC-like poly-Si FBC is the most appealing for industrial uptake due to the limited number of new tools/processes needed in comparison to the existing PERC production lines. Besides that, the feasibility of poly-Si IBC cell structure in mass production has been also proven.
3) Metal compound/c-Si heterojunction solar cells: The best efficiency over 23% has been achieved, which is approaching the conventional homojunction c-Si solar cells. Compared to the SHJ and Poly-Si CSPC technologies, the device efficiency is mainly limited by a low V_{OC}, further improvement of the surface passivation quality or development of new metal compound with excellent passivating contact properties would be the primary task. A highly transparent dopant-free electron-selective contact that is highly demanded for SHJ devices, is still not available. The development of high effi-

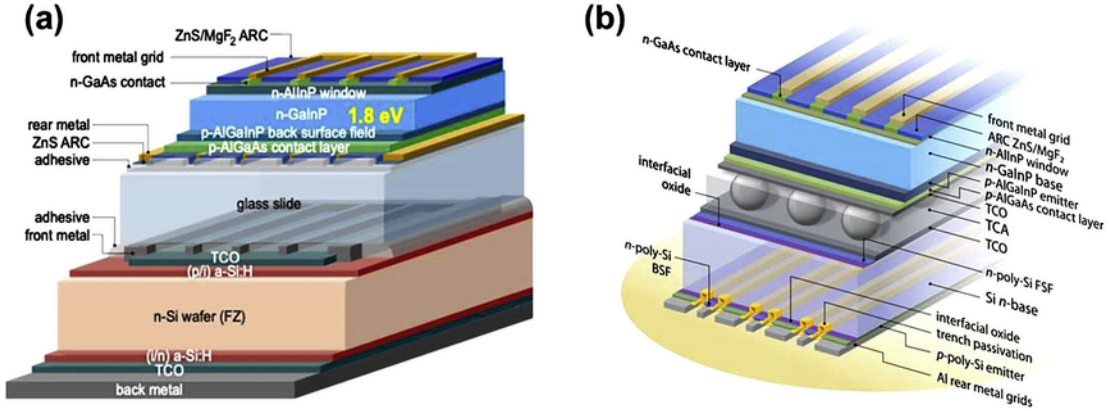

Fig. 30. Mechanically stacked solar cells. (a) Four-terminal tandem using an insulating adhesive and a Si heterojunction bottom cell. Reprinted with permission from ref. [20]. Copyright 2017, Springer Nature. (b) Three-terminal tandem using a TCA and a specially designed IBC bottom cell with a conductive top surface. Reprinted with permission from ref. [543]. Copyright 2020, The Royal Society of Chemistry.

ciency, flexible c-Si solar cells with low temperature deposited dopant-free passivation contacts on both polarities would be a very interesting topic, however, it depends on the development of high-quality dopant-free passivation contacts.

4) Si/organic heterojunction solar cells, combined with the characters of Si and organic materials, promise to design cost-effective, lightweight, and flexible c-Si solar cells. However, device stability is still an issue. The degradation of organic materials within environmental conditions, such as water, oxygen, and light, is one of the most important reasons. Given the current 25 years requirement of commercial solar cell productions, much stable organic materials are highly required.
5) Perovskite/c-Si tandem structure is a promising scheme to overcome the theory limitation of single-junction Si solar cells. In addition to the excellent optical and electrical properties, the tunable bandgap of perovskite materials guarantees an ideal alternative matching with Si to design tandem solar cells. The state-of-the-art efficiency of perovskite/Si tandem solar cells reaches 29.1%. On the other hand, the burgeoning perovskite solar cells are breaking their efficiency records quickly. Hence, over 30% efficiency is foreseeable for perovskite/Si tandem solar cells.
6) Future advances in III-V/Si tandems should focus on translating the already-achieved high efficiencies to commercially-viable prototypes. Of particular importance will be reducing the cost of the III-V materials (e.g. using low-cost growth techniques [561] and grown directly on Si [550]), demonstrating string-level interconnections that maintain high energy yield [562], and demonstrating reliability via outdoor testing and meeting qualification standards [563].

Among various PV devices, Si solar cell is still the most predominate production in market share. On the other hand, challenges still exist. We believe this review will help to learn the achievements, remaining challenges, and possible research directions, and promote this field more rapid development.

Declaration of Competing Interest

The authors report no declarations of interest.

Acknowledgments

Y. L., Y. L. and B. S. acknowledge the National Natural Science Foundation of China (91833303, 61974098 and 61674108), Jiangsu High Educational Natural Science Foundation (18KJA430012), the National Key Research and Development Program (2016YFA0201900), the 111 Program and Collaborative Innovation Center of Suzhou Nano Science and Technology, the Priority Academic Program Development of Jiangsu Higher Education Institutions and Collaborative Innovation Center of Suzhou Nano Science & Technology. A.T.'s work was supported by the U.S. Department of Energy under Contract No. DE-AC36-08GO28308 with Alliance for Sustainable Energy, LLC, the Manager and Operator of the National Renewable Energy Laboratory, with funding provided by the Department of Energy Office of Energy Efficiency and Renewable Energy Solar Energy Technologies Office under contract SETP DE-EE00034911.

References

[1] N.S. Lewis, D.G. Nocera, Proc. Natl. Acad. Sci. 103 (2006) 15729–15735.
[2] D.M. Chapin, C.S. Fuller, G.L. Pearson, J. Appl. Phys. 25 (1954) 676–677.
[3] A. Polman, M. Knight, E.C. Garnett, B. Ehrler, W.C. Sinke, Science 352 (2016), aad4424.
[4] International Technology Roadmap for Photovoltaic (ITRPV), 2020 https://itrpv.vdma.org/.
[5] M.A. Green, Sol. Energy Mater. Sol. Cells 143 (2015) 190–197.
[6] J. Zhao, A. Wang, M.A. Green, Prog. Photovolt. Res. Appl. 7 (1999) 471–474.
[7] M.A. Green, Adv. Mater. 13 (2001) 1019–1022.
[8] B. Hoex, J.J.H. Gielis, M.C.M. van de Sanden, W.M.M. Kessels, J. Appl. Phys. 104 (2008), 113703.
[9] J. Benick, B. Hoex, M.C.M.v.d. Sanden, W.M.M. Kessels, O. Schultz, S.W. Glunz, Appl. Phys. Lett. 92 (2008), 253504.
[10] T.G. Allen, J. Bullock, X.B. Yang, A. Javey, S. De Wolf, Nat. Energy 4 (2019) 914–928.
[11] M. Hermle, F. Feldmann, M. Bivour, J.C. Goldschmidt, S.W. Glunz, Appl. Phys. Rev. 7 (2020), 021305.
[12] F. Fertig, R. Lantzsch, A. Mohr, M. Schaper, M. Bartzsch, D. Wissen, F. Kersten, A. Mette, S. Peters, A. Eidner, J. Cieslak, K. Duncker, M. Junghänel, E. Jarzembowski, M. Kauert, B. Faulwetter-Quandt, D. Meißner, B. Reiche, S. Geißler, S. Hörnlein, C. Klenke, L. Niebergall, A. Schönmann, A. Weihrauch, F. Stenzel, A. Hofmann, T. Rudolph, A. Schwabedissen, M. Gundermann, M. Fischer, J.W. Müller, D.J.W. Jeong, Energy Procedia 124 (2017) 338–345.
[13] M.A. Green, E.D. Dunlop, J. Hohl-Ebinger, M. Yoshita, N. Kopidakis, A.W.Y. Ho-Baillie, Prog. Photovolt. Res. Appl. 28 (2020) 3–15.
[14] K. Yoshikawa, H. Kawasaki, W. Yoshida, T. Irie, K. Konishi, K. Nakano, T. Uto, D. Adachi, M. Kanematsu, H. Uzu, K. Yamamoto, Nat. Energy 2 (2017) 17032.
[15] F. Haase, C. Hollemann, S. Schäfer, A. Merkle, M. Rienäcker, J. Krügener, R. Brendel, R. Peibst, Sol. Energy Mater. Sol. Cells 186 (2018) 184–193.
[16] J. Schmidt, R. Peibst, R. Brendel, Sol. Energy Mater. Sol. Cells 187 (2018) 39–54.
[17] X. Yang, K. Weber, Z. Hameiri, S. De Wolf, Prog. Photovolt. Res. Appl. 25 (2017) 896–904.
[18] J. Dréon, Q. Jeangros, J. Cattin, J. Haschke, L. Antognini, C. Ballif, M. Boccard, Nano Energy 70 (2020), 104495.
[19] NERL, https://www.nrel.gov/pv/assets/pdfs/best-research-cell-efficiencies.20200128.pdf (2020).
[20] S. Essig, C. Allebé, T. Remo, J.F. Geisz, M.A. Steiner, K. Horowitz, L. Barraud, J.S. Ward, M. Schnabel, A. Descoeudres, David L. Young, M. Woodhouse, M. Despeisse, C. Ballif, A. Tamboli, Nat. Energy 2 (2017) 17144.
[21] U. Würfel, A. Cuevas, P. Würfel, IEEE J. Photovolt. 5 (2015) 461–469.
[22] J. Nelson, The Physics of Solar Cells, Imperial College Press, London, 2003.
[23] P. Würfel, U. Würfel, Physics of Solar Cells: from Basic Principles to Advanced Concepts, Wiley-VCH, Weinheim, 2009.
[24] G. Coletti, P.C.P. Bronsveld, G. Hahn, W. Warta, D. Macdonald, B. Ceccaroli, K. Wambach, N. Le Quang, J.M. Fernandez, Adv. Funct. Mater. 21 (2011) 879–890.
[25] N.E. Grant, F.E. Rougieux, D. Macdonald, J. Bullock, Y. Wan, J. Appl. Phys. 117 (2015), 055711.
[26] A.Y. Liu, D. Macdonald, Appl. Phys. Lett. 110 (2017), 191604.
[27] D. Macdonald, Appl. Phys. A 81 (2005) 1619.
[28] S.P. Phang, D. Macdonald, IEEE J. Photovolt. 4 (2014) 64–69.
[29] J. Kim, S.Y. Yoon, K. Choi, Curr. Appl. Phys. 13 (2013) 2103–2108.
[30] PVeducation, https://www.pveducation.org/pvcdrom/solar-cell-operation/iv-curve.
[31] J. Zhang, S.-T. Lee, B. Sun, Electrochim. Acta 146 (2014) 845–849.
[32] E.E. van Dyk, E.L. Meyer, Renewable Energy 29 (2004) 333–344.
[33] G. Sulyok, J. Summhammer, Energy Sci. Eng. 6 (2018) 424–436.
[34] M.A. Green, Sol. Cells 7 (1982) 337–340.
[35] R. Sinton, A. Cuevas, A Quasi-Steady-State Open-Circuit Voltage Method for Solar Cell Characterization, In: 16th European Photovoltaic Solar Energy Conference, 2000.
[36] R.A. Sinton, A. Cuevas, Appl. Phys. Lett. 69 (1996) 2510–2512.
[37] D. Macdonald, R.A. Sinton, A. Cuevas, J. Appl. Phys. 89 (2001) 2772–2778.
[38] R.H. Cox, H. Strack, Solid. State. Electron. 10 (1967) 1213–1218.
[39] G.K. Reeves, H.B. Harrison, IEEE Electron Device Lett. 3 (1982) 111–113.
[40] J. Bullock, A. Cuevas, T. Allen, C. Battaglia, Appl. Phys. Lett. 105 (2014), 232109.
[41] W. Wang, H. Lin, Z. Yang, Z. Wang, J. Wang, L. Zhang, M. Liao, Y. Zeng, P. Gao, B. Yan, J. Ye, IEEE J. Photovolt. 9 (2019) 1113–1120.
[42] D. Adachi, J.L. Hernández, K. Yamamoto, Appl. Phys. Lett. 107 (2015), 233506.
[43] S. Noguchi, H. Iwata, K. Sano, Photovoltaic device, Google Patents, 1993.
[44] REC, https://www.recgroup.com/en/alpha.
[45] Panasonic, https://na.panasonic.com/us/energy-solutions/solar/hit-panels.
[46] C. Ballif, M. Boccard, M. Despeisse, The Amazing Improvement of Silicon Heterojunction Technology: Ready for a True Mass Market Launch, In: IEEE 7th World Conference on Photovoltaic Energy Conversion, 2018.
[47] J. Haschke, O. Dupré, M. Boccard, C. Ballif, Sol. Energy Mater. Sol. Cells 187 (2018) 140–153.
[48] H. Matsunami, K. Oo, H. Ito, T. Tanaka, Jpn. J. Appl. Phys. 14 (1975) 915.

[49] K. Kajiyama, Y. Furukawa, Jpn. J. Appl. Phys. 6 (1967) 905.
[50] W. Fuhs, K. Niemann, J. Stuke, AIP Conf. Proc. 20 (1974) 345–350.
[51] M.A. Green, Physica E 14 (2002) 65–70.
[52] M. Taguchi, K. Kawamoto, S. Tsuge, T. Baba, H. Sakata, M. Morizane, K. Uchihashi, N. Nakamura, S. Kiyama, O. Oota, Prog. Photovolt. Res. Appl. 8 (2000) 503–513.
[53] K. Yamamoto, D. Adachi, H. Uzu, M. Ichikawa, T. Terashita, T. Meguro, N. Nakanishi, M. Yoshimi, J.L. Hernández, Jpn. J. Appl. Phys. 54 (2015), 08KD15.
[54] M. Despeisse, L. Barraud, B. Paviet-Salomon, A. Descoeudres, L.-L. Senaud, C. Allebe, J. Levrat, J. Horzel, A. Lachowicz, F. Debrot, J. Champliaud, A. Faes, N. Badel, J. Geissbuhler, S.M.d. Nicolas, G. Christmann, J. Diaz, L. Ding, S. Nicolay, C. Ballif, Engineering of Thin-Film Silicon Materials for High Efficiency Crystalline Silicon Solar Cells, In: IEEE 7th World Conference on Photovoltaic Energy Conversion, 2018.
[55] E. Kobayashi, S. De Wolf, J. Levrat, G. Christmann, A. Descoeudres, S. Nicolay, M. Despeisse, Y. Watabe, C. Ballif, Appl. Phys. Lett. 109 (2016) 1–6.
[56] T. Matsui, H. Sai, K. Saito, M. Kondo, Jpn. J. Appl. Phys. 51 (2012), 10NB04.
[57] M. Stuckelberger, Y. Riesen, M. Despeisse, J.-W. Schüttauf, F.-J. Haug, C. Ballif, J. Appl. Phys. 116 (2014), 094503.
[58] Z. Mrazkova, I.P. Sobkowicz, M. Foldyna, K. Postava, I. Florea, J. Pištora, P. Roca i Cabarrocas, Prog. Photovolt. Res. Appl. 26 (2018) 369–376.
[59] M. Boccard, Z.C. Holman, J. Appl. Phys. 118 (2015), 065704.
[60] W. Beyer, H. Mell, Composition and Thermal Stability of Glow-Discharge a-Si:C:H and a-Si:N:H Alloys, Springer, 1987.
[61] S. De Wolf, M. Kondo, J. Appl. Phys. 105 (2009), 103707.
[62] A.H.M. Smets, M.C.M. van de Sanden, Phys. Rev. B 76 (2007), 073202.
[63] A. Descoeudres, C. Allebe, N. Badel, L. Barraud, J. Champliaud, G. Christmann, L. Curvat, F. Debrot, A. Faes, J. Geissbiihler, J. Horzel, A. Lachowicz, J. Levrat, S. Martin de Nicolas, S. Nicolay, B. Paviet-Salomon, L.-L. Senaud, A. Tomasi, C. Ballif, M. Despeisse, Advanced Silicon Thin Films for High-Efficiency Silicon Heterojunction-Based Solar Cells, In: IEEE 44th Photovoltaic Specialist Conference, 2017.
[64] H. Sai, P.W. Chen, H.J. Hsu, T. Matsui, S. Nunomura, K. Matsubara, J. Appl. Phys. 124 (2018), 103102.
[65] T. Ruan, M. Qu, J. Wang, Y. He, X. Xu, C. Yu, Y. Zhang, H. Yan, J. Mater, Sci. Mater. Electron. 30 (2019) 13330–13335.
[66] J.P. Seif, A. Descoeudres, M. Filipič, F. Smole, M. Topič, Z.C. Holman, S. De Wolf, C. Ballif, J. Appl. Phys. 115 (2014), 024502.
[67] M. Mews, M. Liebhaber, B. Rech, L. Korte, Appl. Phys. Lett. 107 (2015), 013902.
[68] W. Liu, L. Zhang, X. Yang, J. Shi, L. Yan, L. Xu, Z. Wu, R. Chen, J. Peng, J. Kang, K. Wang, F. Meng, S. De Wolf, Z. Liu, Joule 4 (2020) 913–927.
[69] W.E. Spear, P.G. Le Comber, Solid State Commun. 88 (1975) 1015–1018.
[70] J. Robertson, Phys. Rev. B 33 (1986), 4399-4301.
[71] M. Bivour, M. Reusch, S. Schroer, F. Feldmann, J. Temmler, H. Steinkemper, M. Hermle, IEEE J. Photovolt. 4 (2014) 566–574.
[72] G. Nogay, J.P. Seif, Y. Riesen, A. Tomasi, Q. Jeangros, N. Wyrsch, F.J. Haug, S. De Wolf, C. Ballif, IEEE J. Photovolt. 6 (2016) 1654–1662.
[73] H. Mimura, Y. Hatanaka, J. Appl. Phys. 71 (1992) 2315.
[74] T.F. Schulze, L. Korte, E. Conrad, M. Schmidt, B. Rech, J. Appl. Phys. 107 (2010), 023711.
[75] P. Muralidharan, M.A. Leilaeioun, W. Weigand, Z.C. Holman, S.M. Goodnick, D. Vasileska, IEEE J. Photovolt. 10 (2020) 363–371.
[76] R.V.K. Chavali, S. De Wolf, M.A. Alam, Prog. Photovolt. Res. Appl. (2018) 241–260.
[77] L. Martini, L. Serenelli, F. Menchini, M. Izzi, M. Tucci, Prog. Photovolt. Res. Appl. (2020) 307–320.
[78] D.P. Pham, S. Kim, S. Kim, S. Lee, A.H.T. Le, J. Park, J. Yi, Mater. Sci. Semicond. Process. 96 (2019) 1–7.
[79] L. Mazzarella, A.B. Morales-Vilches, M. Hendrichs, S. Kirner, L. Korte, R. Schlatmann, B. Stannowski, IEEE J. Photovolt. 8 (2017) 70–78.
[80] A.N. Fioretti, M. Boccard, R. Monnard, C. Ballif, IEEE J. Photovolt. 9 (2019) 1158–1165.
[81] C. Peng, C. Lei, T. Ruan, J. Zhong, M. Yang, W. Long, C. Yu, Y. Li, X. Xu, High Phosphorus-doped Seed Layer in Microcrystalline Silicon Oxide Front Contact Layers for Silicon Heterojunction Solar Cells, In: IEEE 46th Photovoltaic Specialists Conference, 2019.
[82] P. Cuony, D.T.L. Alexander, I. Perez-Wurfl, M. Despeisse, G. Bugnon, M. Boccard, T. Söderström, A. Hessler-Wyser, C. Hebert, C. Ballif, Adv. Mater. 24 (2012) 1182–1186.
[83] L.V. Mercaldo, P. Delli Veneri, I. Usatii, E.M. Esposito, G. Nicotra, Sol. Energy Mater. Sol. Cells 119 (2013) 67–72.
[84] J.P. Seif, A. Descoeudres, G. Nogay, S. Hanni, S.M. De Nicolas, N. Holm, J. Geissbuhler, A. Hessler-Wyser, M. Duchamp, R.E. Dunin-Borkowski, M. Ledinsky, S. De Wolf, C. Ballif, IEEE J. Photovolt. 6 (2016) 1132–1140.
[85] L. Mazzarella, A.B. Morales-Vilches, L. Korte, R. Schlatmann, B. Stannowski, Sol. Energy Mater. Sol. Cells 179 (2018) 386–391.
[86] M. Boccard, R. Monnard, L. Antognini, C. Ballif, AIP Conf. Proc. 1999 (2018), 040003.
[87] A. Descoeudres, J. Horzel, B. Paviet-Salomon, L.L. Senaud, G. Christmann, J. Geissbühler, P. Wyss, N. Badel, J.W. Schüttauf, J. Zhao, C. Allebé, A. Faes, S. Nicolay, C. Ballif, M. Despeisse, Prog. Photovolt. Res. Appl. (2019) https://doi.org/10.1002/pip.3227.
[88] D. Chen, M. Kim, J. Shi, B. Vicari Stefani, Z. Yu, S. Liu, R. Einhaus, S. Wenham, Z. Holman, B. Hallam, Prog. Photovolt. Res. Appl. (2019) https://doi.org/10.1002/pip.3230.
[89] J. Li, X. Yu, S. Yuan, L. Yang, Z. Liu, D. Yang, Sol. Energy Mater. Sol. Cells 179 (2018) 17–21.
[90] B. Hallam, D. Chen, J. Shi, R. Einhaus, Z.C. Holman, S. Wenham, Sol. RRL 2 (2018), 1700221.
[91] R. Basnet, W. Weigand, Z.J. Yu, C. Sun, S.P. Phang, F.E. Rougieux, R. Einhaus, J. Degoulange, Z. Holman, D. Macdonald, Impact of Tabula Rasa and Phosphorus Diffusion Gettering on 21% Heterojunction Solar Cells Based on n-Type Czochralski-Grown Upgrade Metallurgical-Grade Silicon, In: IEEE 7th World Conference on Photovoltaic Energy Conversion, 2018.
[92] B. Vicari Stefani, W. Weigand, M. Wright, A. Soeriyadi, Z. Yu, M. Kim, D. Chen, Z. Holman, B. Hallam, Phys. Status Solidi A 216 (2019), 1900319.
[93] C. Sun, W. Weigand, J. Shi, Z. Yu, R. Basnet, S.P. Phang, Z.C. Holman, D. Maconald, Appl. Phys. Lett. 115 (2019), 252103.
[94] M.M. Kivambe, J. Haschke, J. Horzel, B. Aïssa, A.A. Abdallah, A. Belaidi, R. Monnard, L. Barraud, A. Descoeudres, F. Debrot, M. Despeisse, M. Boccard, C. Ballif, N. Tabet, ACS Appl. Energy Mater. 2 (2019) 4900–4906.
[95] M. Wright, M. Kim, P. Dexiang, X. Xin, Z. Wenbin, B. Wright, B. Hallam, AIP Conf. Proc. 2147 (2019), 110006.
[96] S. DeWolf, A. Descoeudres, Z.C. Holman, C. Ballif, S. De Wolf, A. Descoeudres, Z.C. Holman, C. Ballif, S. DeWolf, A. Descoeudres, Z.C. Holman, C. Ballif, Green 2 (2012) 7–24.
[97] J. Shi, M. Boccard, Z. Holman, Appl. Phys. Lett. 109 (2016), 031601.
[98] S. De Wolf, B. Demaurex, A. Descoeudres, C. Ballif, Phys. Rev. B 83 (2011), 233301.
[99] P. Mahtani, R. Varache, B. Jovet, C. Longeaud, J.-P. Kleider, N.P. Kherani, J. Appl. Phys. 114 (2013), 124503.
[100] E.M. El Mhamdi, J. Holovsky, B. Demaurex, C. Ballif, S. De Wolf, Appl. Phys. Lett. 104 (2014), 252108.
[101] J. Cattin, J. Haschke, O. Dupré, M. Boccard, C. Ballif, Passivation and Transport Modification upon Light Soaking of Silicon Heterojunction Solar Cells, In: European PV Solar Energy Conference and Exhibition, 2019.
[102] E. Kobayashi, S. De Wolf, J. Levrat, A. Descoeudres, M. Despeisse, F.-J. Haug, C. Ballif, Sol. Energy Mater. Sol. Cells 173 (2017) 43–49.
[103] A. Descoeudres, C. Allebé, N. Badel, L. Barraud, J. Champliaud, G. Christmann, F. Debrot, A. Faes, J. Geissbühler, J. Horzel, A. Lachowicz, J. Levrat, S. Martin de Nicolas, S. Nicolay, B. Paviet-Salomon, L.L. Senaud, C. Ballif, M. Despeisse, Sol. Energy 175 (2018) 54–59.
[104] J. Schube, T. Fellmeth, M. Jahn, R. Keding, S.W. Glunz, AIP Conf. Proc. 2156 (2019), 020007.
[105] J. Schube, T. Fellmeth, M. Jahn, R. Keding, S.W. Glunz, Phys. Status Solidi RRL 13 (2019) 5–9.
[106] A. Faes, A. Lachowicz, A. Bettinelli, P. Ribeyron, J. Lerat, D. Munoz, J. Geissbühler, H. Li, C. Ballif, M. Despeisse, Photovolt. Bull. 41 (2018) 1–5.
[107] J. Meier, U. Kroll, S. Benagli, L. Fesquet, J. Steinhauser, D. Borello, J.B. Orhan, Y. Djeridane, E. Vallat-Sauvain, M. Fecioru-Morariu, B. Mereu, J. Kalas, J. Hoetzel, P. Losio, M. Kupich, O. Kluth, T. Eisenhammer, D. Weidman, S. Marjanovic, G. Kohnke, Energy Procedia 15 (2012) 179–188.
[108] A. Moldovan, A. Fischer, J. Temmler, M. Bivour, T. Dannenberg, D. Erath, A. Lorenz, D. Sontag, J. Zhao, A. Wissen, F. Clement, M. Zimmer, J. Rentsch, Energy Procedia 124 (2017) 357–364.
[109] J. Geissbühler, A. Faes, A. Lachowicz, C. Ballif, M. Despeisse, Photovolt. Int. 37 (2017) 61–69.
[110] J. Geissbühler, S.D. Wolf, A. Faes, N. Badel, Q. Jeangros, A. Tomasi, L. Barraud, A. Descoeudres, M. Despeisse, C. Ballif, IEEE J. Photovolt. 4 (2014) 1055–1062.
[111] T. Koida, Y. Ueno, H. Shibata, Phys. Status Solidi A 215 (2018), 1700506.
[112] L.-L. Senaud, G. Christmann, A. Descoeudres, J. Geissbuhler, L. Barraud, N. Badel, C. Allebe, S. Nicolay, M. Despeisse, B. Paviet-Salomon, C. Ballif, IEEE J. Photovolt. 9 (2019) 1217–1224.
[113] J.P. Niemelä, B. Macco, L. Barraud, A. Descoeudres, N. Badel, M. Despeisse, G. Christmann, S. Nicolay, C. Ballif, W.M.M. Kessels, M. Creatore, Sol. Energy Mater. Sol. Cells 200 (2019), 109953.
[114] A.B. Morales-Vilches, A. Cruz, S. Pingel, S. Neubert, L. Mazzarella, D. Meza, L. Korte, R. Schlatmann, B. Stannowski, IEEE J. Photovolt. 9 (2019) 34–39.
[115] D. Lachenal, P. Papet, B. Legradic, R. Kramer, T. Kössler, L. Andreetta, N. Holm, W. Frammelsberger, D.L. Baetzner, B. Strahm, L.L. Senaud, J.W. Schüttauf, A. Descoeudres, G. Christmann, S. Nicolay, M. Despeisse, B. Paviet-Salomon, C. Ballif, Sol. Energy Mater. Sol. Cells 200 (2019), 110036.
[116] S.Y. Herasimenka, W.J. Dauksher, M. Boccard, S. Bowden, Sol. Energy Mater. Sol. Cells 158 (2016) 98–101.

[117] D.L. Bätzner, P. Papet, B. Legradic, D. Lachenal, R. Kramer, T. Kössler, L. Andreetta, S. Pitteloud, N. Holm, J.P. Cardoso, C. Aeby, W. Frammelsberger, B. Strahm, Alleviating Performance and Cost Constraints in Silicon Heterojunction Cells with HJT 2.0, In: IEEE 46th Photovoltaic Specialists Conference, 2019.
[118] T. Koida, H. Fujiwara, M. Kondo, Sol. Energy Mater. Sol. Cells 93 (2009) 851–854.
[119] L. Barraud, Z.C. Holman, N. Badel, P. Reiss, A. Descoeudres, C. Battaglia, S. De Wolf, C. Ballif, Sol. Energy Mater. Sol. Cells 115 (2013) 151–156.
[120] E. Kobayashi, Y. Watabe, T. Yamamoto, Y. Yamada, Sol. Energy Mater. Sol. Cells 149 (2016) 75–80.
[121] J. Yu, J. Bian, W. Duan, Y. Liu, J. Shi, F. Meng, Z. Liu, Sol. Energy Mater. Sol. Cells 144 (2015) 359–363.
[122] M. Morales-Masis, E. Rucavado, R. Monnard, L. Barraud, J. Holovský, M. Despeisse, M. Boccard, C. Ballif, IEEE J. Photovolt. 8 (2018) 1202–1207.
[123] B. Demaurex, S. De Wolf, A. Descoeudres, Z. Charles Holman, C. Ballif, Appl. Phys. Lett. 101 (2012), 171604.
[124] R. Röler, C. Leendertz, L. Korte, N. Mingirulli, B. Rech, J. Appl. Phys. 113 (2013), 144513.
[125] A. Tomasi, F. Sahli, J.P. Seif, L. Fanni, S.M.d.N. Agut, J. Geissbühler, B. Paviet-Salomon, S. Nicolay, L. Barraud, B. Niesen, S. De Wolf, C. Ballif, IEEE J. Photovolt. 6 (2016) 17–27.
[126] H. Li, W. Duan, A. Lambertz, J. Hupkes, K. Ding, U. Rau, O. Astakhov, IEEE J. Photovolt. 9 (2019) 1485–1491.
[127] J. Cattin, J. Haschke, C. Ballif, M. Boccard, Appl. Phys. Lett. 116 (2020), 113901.
[128] J. Haschke, G. Christmann, C. Messmer, M. Bivour, M. Boccard, C. Ballif, J. Appl. Phys. 127 (2020), 114501.
[129] M. Taguchi, A. Yano, S. Tohoda, K. Matsuyama, Y. Nakamura, T. Nishiwaki, K. Fujita, E. Maruyama, IEEE J. Photovolt. 4 (2014) 96–99.
[130] C.X. Xu, Micro-crystalline Silicon Oxide Front Contact Layers for Silicon Heterojunction Solar Cells, In: 2nd International Workshop on SHJ Solar Cells, 2019.
[131] W.F. Brinkman, D.E. Haggan, W.W. Troutman, IEEE J. Solid-State Circuits 32 (1997) 1858–1865.
[132] R.B. Fair, Proc. IEEE 86 (1998) 111–137.
[133] I.R.C. Post, P. Ashburn, G.R. Wolstenholme, IEEE Trans. Electron Dev. 39 (1992) 1717–1731.
[134] Y.H. Kwark, R. Sinton, R.M. Swanson, SIPOS Heterojunction contacts to silicon, In: Int. Electron Devices Meet., 1984.
[135] E. Yablonovitch, T. Gmitter, R.M. Swanson, Y.H. Kwark, Appl. Phys. Lett. 47 (1985) 1211–1213.
[136] N.G. Tarr, IEEE Electron Device Lett. 6 (1985) 655–658.
[137] F.A. Lindholm, A. Neugroschel, M. Arienzo, P.A. Iles, IEEE Electron Device Lett. 6 (1985) 363–365.
[138] F. Feldmann, M. Bivour, C. Reichel, M. Hermle, S.W. Glunz, A Passivated Rear Contact for High-Efficiency n-Type Silicon Solar Cells Enabling High Vocs and FF& 82%, In: 28th European PV Solar Energy Conference and Exhibition, 2013.
[139] U. Römer, R. Peibst, T. Ohrdes, B. Lim, J. Krügener, T. Wietler, R. Brendel, IEEE J. Photovolt. 5 (2015) 507–514.
[140] M.K. Stodolny, M. Lenes, Y. Wu, G.J.M. Janssen, I.G. Romijn, J.R.M. Luchies, L.J. Geerligs, Sol. Energy Mater. Sol. Cells 158 (2016) 24–28.
[141] S. Duttagupta, N. Nandakumar, P. Padhamnath, J.K. Buatis, R. Stangl, A.G. Aberle, Sol. Energy Mater. Sol. Cells 187 (2018) 76–81.
[142] Y. Chen, D. Chen, C. Liu, Z. Wang, Y. Zou, Y. He, Y. Wang, L. Yuan, J. Gong, W. Lin, X. Zhang, Y. Yang, H. Shen, Z. Feng, P.P. Altermatt, P.J. Verlinden, Prog. Photovolt. Res. Appl. 27 (2019) 827–834.
[143] G. Limodio, G. Yang, Y. De Groot, P. Procel, L. Mazzarella, A.W. Weber, O. Isabella, M. Zeman, Prog. Photovolt. Res. Appl. (2020) https://doi.org/10.1002/pip.3250.
[144] A. Richter, J. Benick, F. Feldmann, A. Fell, M. Hermle, S.W. Glunz, Sol. Energy Mater. Sol. Cells 173 (2017) 96–105.
[145] A. Richter, J. Benick, F. Feldmann, A. Fell, B. Steinhauser, J. Polzin, N. Tucher, J. Murthy, M. Hermle, S. Glunz, Both Sides Contacted Silicon Solar Cells: Options for Approaching 26% Efficiency, In: 36th European PV Solar Energy Conference and Exhibition, 2019.
[146] R. Brendel, R. Peibst, IEEE J. Photovolt. 6 (2016) 1413–1420.
[147] A. Cuevas, Y. Wan, D. Yan, C. Samundsett, T. Allen, X. Zhang, J. Cui, J. Bullock, Sol. Energy Mater. Sol. Cells 184 (2018) 38–47.
[148] J. Melskens, B.W.H. Van De Loo, B. Macco, L.E. Black, S. Smit, W.M.M. Kessels, IEEE J. Photovolt. 8 (2018) 373–388.
[149] S.W. Glunz, F. Feldmann, Sol. Energy Mater. Sol. Cells 185 (2018) 260–269.
[150] F. Feldmann, M. Bivour, C. Reichel, M. Hermle, S.W. Glunz, H. Steinkemper, M. Hermle, S.W. Glunz, M. Simon, M. Bivour, C. Reichel, M. Hermle, S.W. Glunz, P. Stradins, S. Essig, W. Nemeth, B.G. Lee, D. Young, A. Norman, Y. Liu, J.-w. Luo, E. Warren, A. Dameron, V. Lasalvia, M. Page, Y. Ok, Y. Tao, V. Upadhyaya, K. Jones, A. Rohatgi, J.C. Goldschmidt, Sol. Energy Mater. Sol. Cells 131 (2014) 46–50.
[151] D. Yan, A. Cuevas, J. Bullock, Y. Wan, C. Samundsett, Sol. Energy Mater. Sol. Cells 142 (2015) 75–82.
[152] D. Yan, A. Cuevas, Y. Wan, J. Bullock, Sol. Energy Mater. Sol. Cells 152 (2016) 73–79.
[153] F. Feldmann, C. Reichel, R. Müller, M. Hermle, Sol. Energy Mater. Sol. Cells 159 (2017) 265–271.
[154] G. Yang, A. Ingenito, N. van Hameren, O. Isabella, M. Zeman, Appl. Phys. Lett. 108 (2016), 033903.
[155] F. Feldmann, G. Nogay, P. Löper, D.L. Young, B.G. Lee, P. Stradins, M. Hermle, S.W. Glunz, Sol. Energy Mater. Sol. Cells 178 (2018) 15–19.
[156] A. Ingenito, G. Nogay, J. Stuckelberger, P. Wyss, L. Gnocchi, C. Allebe, J. Horzel, M. Despeisse, F.-J. Haug, P. Loper, C. Ballif, IEEE J. Photovolt. 9 (2019) 346–354.
[157] R. Peibst, U. Romer, Y. Larionova, M. Rienacker, A. Merkle, N. Folchert, S. Reiter, M. Turcu, B. Min, J. Krugener, D. Tetzlaff, E. Bugiel, T. Wietler, R. Brendel, Sol. Energy Mater. Sol. Cells 158 (2016) 60–67.
[158] T.F. Wietler, D. Tetzlaff, J. Krügener, M. Rienäcker, F. Haase, Y. Larionova, R. Brendel, R. Peibst, Appl. Phys. Lett. 110 (2017), 253902.
[159] N. Folchert, M. Rienäcker, A.A. Yeo, B. Min, R. Peibst, R. Brendel, Sol. Energy Mater. Sol. Cells 185 (2018) 425–430.
[160] P. Procel, G. Yang, O. Isabella, M. Zeman, IEEE J. Photovolt. 9 (2019) 374–384.
[161] H. Steinkemper, F. Feldmann, M. Bivour, M. Hermle, IEEE J. Photovolt. 5 (2015) 1348–1356.
[162] P. Procel, P. Löper, F. Crupi, C. Ballif, A. Ingenito, Sol. Energy Mater. Sol. Cells 200 (2019), 109937.
[163] S. Choi, K.H. Min, M.S. Jeong, J.I. Lee, M.G. Kang, H.E. Song, Y. Kang, H.S. Lee, D. Kim, K.H. Kim, Sci. Rep. 7 (2017) 1–11.
[164] A. Campa, F. Smole, N. Folchert, T. Wietler, B. Min, R. Brendel, M. Topic, IEEE J. Photovolt. 9 (2019) 1575–1582.
[165] A.S. Kale, W. Nemeth, H. Guthrey, E. Kennedy, A.G. Norman, M. Page, M. Al-Jassim, D.L. Young, S. Agarwal, P. Stradins, Appl. Phys. Lett. 114 (2019), 083902.
[166] F. Feldmann, J. Schön, J. Niess, W. Lerch, M. Hermle, Sol. Energy Mater. Sol. Cells 200 (2019), 109978.
[167] U. Wurfel, A. Cuevas, P. Wurfel, IEEE J. Photovolt. 5 (2015) 461–469.
[168] A. Ingenito, G. Nogay, Q. Jeangros, E. Rucavado, C. Allebé, S. Eswara, N. Valle, T. Wirtz, J. Horzel, T. Koida, M. Morales-Masis, M. Despeisse, F.-J. Haug, P. Löper, C. Ballif, Nat. Energy 3 (2018) 800–808.
[169] G. Nogay, J. Stuckelberger, P. Wyss, Q. Jeangros, C. Allebé, X. Niquille, F. Debrot, M. Despeisse, F.-J. Haug, P. Löper, C. Ballif, ACS Appl. Mater. Interfaces 8 (2016) 35660–35667.
[170] G. Yang, P. Guo, P. Procel, A. Weeber, O. Isabella, M. Zeman, Appl. Phys. Lett. 112 (2018), 193904.
[171] M. Köhler, M. Pomaska, F. Lentz, F. Finger, U. Rau, K. Ding, ACS Appl. Mater. Interfaces 10 (2018) 14259–14263.
[172] A. Cuevas, T. Allen, J. Bullock, Skin Care for Healthy Silicon Solar Cells, In: IEEE 42nd Photovoltaic Specialist Conference, 2015.
[173] A.G. Aberle, Prog. Photovolt. Res. Appl. 8 (2000) 473–487.
[174] A.D. Upadhyaya, Y.-w. Ok, E. Chang, V. Upadhyaya, K. Madani, K. Tate, B. Rounsaville, C.-j. Choi, V. Chandrasekaran, V. Yelundur, A. Gupta, A. Rohatgi, IEEE J. Photovolt. 6 (2016) 153–158.
[175] H. Kim, S. Bae, K.s. Ji, S.M. Kim, J.W. Yang, C.H. Lee, K.D. Lee, S. Kim, Y. Kang, H.S. Lee, D. Kim, Appl. Surf. Sci. 409 (2017) 140–148.
[176] A. Moldovan, F. Feldmann, M. Zimmer, J. Rentsch, J. Benick, M. Hermle, Sol. Energy Mater. Sol. Cells 142 (2015) 123–127.
[177] T. Gao, Q. Yang, X. Guo, Y. Huang, Z. Zhang, Z. Wang, M. Liao, C. Shou, Y. Zeng, B. Yan, G. Hou, X. Zhang, Y. Zhao, J. Ye, Sol. Energy Mater. Sol. Cells 200 (2019), 109926.
[178] M. Lozac'h, S. Nunomura, K. Matsubara, Sol. Energy Mater. Sol. Cells 207 (2020), 110357.
[179] J. Schmidt, R. Peibst, R. Brendel, Sol. Energy Mater. Sol. Cells 187 (2018) 39–54.
[180] A.S. Kale, W. Nemeth, H. Guthrey, S.U. Nanayakkara, V. Lasalvia, S. Theingi, D. Findley, M. Page, M. Al-Jassim, D.L. Young, P. Stradins, S. Agarwal, ACS Appl. Mater. Interfaces 11 (2019) 42021–42031.
[181] H.Z. Massoud, Solid. State. Electron. 41 (1997) 929–934.
[182] T.G. Allen, A. Cuevas, Appl. Phys. Lett. 105 (2014) 1–5.
[183] G. Krugel, F. Jenkner, A. Moldovan, W. Wolke, J. Rentsch, R. Preu, Energy Procedia 55 (2014) 797–804.
[184] F. Lin, B. Hoex, Y.H. Koh, J. Lin, A.G. Aberle, ECS J. Solid State Sci. Technol. 2 (2013) 28–31.
[185] J. Steffens, J. Rinder, G. Hahn, B. Terheiden, AIP Conf. Proc. 2147 (2019), 040018.
[186] B. Nemeth, D.L. Young, M.R. Page, V. Lasalvia, S. Johnston, R. Reedy, P. Stradins, J. Mater. Res. 31 (2016) 671–681.
[187] J. Temmler, J.I. Polzin, F. Feldmann, L. Kraus, B. Kafle, S. Mack, A. Moldovan, M. Hermle, J. Rentsch, Phys. Status Solidi A 215 (2018), 1800449.
[188] A. Dastgheib-Shirazi, M. Steyer, G. Micard, H. Wagner, P.P. Altermatt, G. Hahn, Energy Procedia 38 (2013) 254–262.
[189] Y. Schiele, S. Fahr, S. Joos, G. Hahn, B. Terheiden, Study on Boron Emitter Formation by BBR3 Diffusion for n-type Si Solar Cell Applications, In: 28th European PV Solar Energy Conference and Exhibition, 2013.
[190] M. Hayes, B. Martel, G.W. Alam, H. Lignier, S. Dubois, E. Pihan, O. Palais, Phys. Status Solidi A 216 (2019), 1900321.
[191] F. Feldmann, R. Müller, C. Reichel, M. Hermle, Phys. Status Solidi RRL 8 (2014) 767–770.

[192] D.L. Young, B.G. Lee, D. Fogel, W. Nemeth, V. LaSalvia, S. Theingi, M. Page, M. Young, C. Perkins, P. Stradins, IEEE J. Photovolt. 7 (2017) 1640–1645.
[193] A. Richter, J. Benick, R. Müller, F. Feldmann, C. Reichel, M. Hermle, S.W. Glunz, Prog. Photovolt. Res. Appl. 26 (2018) 579–586.
[194] G. Nogay, J. Stuckelberger, P. Wyss, E. Rucavado, C. Allebé, T. Koida, M. Morales-Masis, M. Despeisse, F.-J. Haug, P. Löper, C. Ballif, Sol. Energy Mater. Sol. Cells 173 (2017) 18–24.
[195] M. Schnabel, B.W.H. Van De Loo, W. Nemeth, B. Macco, P. Stradins, W.M.M. Kessels, D.L. Young, Appl. Phys. Lett. 112 (2018), 203901.
[196] S. Lindekugel, H. Lautenschlager, T. Ruof, S. Reber, Plasma Hydrogen Passivation For Crystalline Silicon Thin-Films, In: 23rd European PV Solar Energy Conference and Exhibition, 2008.
[197] J. Stuckelberger, G. Nogay, P. Wyss, Q. Jeangros, C. Allebé, F. Debrot, X. Niquille, M. Ledinsky, A. Fejfar, M. Despeisse, F.-J. Haug, P. Löper, C. Ballif, Sol. Energy Mater. Sol. Cells 158 (2016) 2–10.
[198] G. Nogay, A. Ingenito, E. Rucavado, Q. Jeangros, J. Stuckelberger, P. Wyss, M. Morales-Masis, F. Haug, P. Löper, C. Ballif, IEEE J. Photovolt. 8 (2018) 1478–1485.
[199] M. Singh, R. Santbergen, L. Mazzarella, A. Madrampazakis, G. Yang, R. Vismara, Z. Remes, A. Weeber, M. Zeman, O. Isabella, Sol. Energy Mater. Sol. Cells 210 (2020), 110507.
[200] M. Pomaska, M. Köhler, P. Procel Moya, A. Zamchiy, A. Singh, D.Y. Kim, O. Isabella, M. Zeman, S. Li, K. Qiu, A. Eberst, V. Smirnov, F. Finger, U. Rau, K. Ding, Prog. Photovolt. Res. Appl. 28 (2020) 321–327.
[201] M. Kohler, F. Finger, U. Rau, K. Ding, M. Pomaska, A. Zamchiy, A. Lambertz, W. Duan, F. Lentz, S. Li, V. Smirnov, T. Kirchartz, IEEE J. Photovolt. 10 (2020) 46–53.
[202] C.J. McHargue, J.M. Williams, Nucl. Instr. Meth. B 80-81 (1993) 889–894.
[203] T. Tachibana, K. Tanahashi, T. Mochizuki, K. Shirasawa, H. Takato, Bifacial Interdigitated-Back-Contact (IBC) Crystalline Silicon Solar Cell: Fabrication and Evaluation by Internal Quantum Efficiency Mapping, In: IEEE 7th World Conference on Photovoltaic Energy Conversion, 2018.
[204] C. Messmer, A. Fell, F. Feldmann, N. Wöhrle, J. Schön, M. Hermle, IEEE J. Photovolt. 10 (2019) 335–342.
[205] A. Ingenito, G. Limodio, P. Procel, G. Yang, H. Dijkslag, O. Isabella, M. Zeman, Sol. RRL 1 (2017), 1700040.
[206] U. Römer, A. Merkle, R. Peibst, T. Ohrdes, B. Lim, J. Krügener, R. Brendel, Ion-Implanted poly-Si/c-Si Junctions as a Back-Surface Field in Back-Junction Back-Contacted Solar Cells, In: 29th European PV Solar Energy Conference and Exhibition, 2014.
[207] M. Rienäcker, A. Merkle, U. Römer, H. Kohlenberg, J. Krügener, R. Brendel, R. Peibst, Energy Procedia 92 (2016) 412–418.
[208] J. Krügener, F. Haase, M. Rienäcker, R. Brendel, H.J. Osten, R. Peibst, Sol. Energy Mater. Sol. Cells 173 (2017) 85–91.
[209] C. Hollemann, F. Haase, S. Schäfer, J. Krügener, R. Brendel, R. Peibst, Prog. Photovolt. Res. Appl. 27 (2019) 950–958.
[210] F. Feldmann, M. Bivour, C. Reichel, H. Steinkemper, M. Hermle, S.W. Glunz, Sol. Energy Mater. Sol. Cells 131 (2014) 46–50.
[211] S.W. Glunz, F. Feldmann, A. Richter, M. Bivour, C. Reichel, H. Steinkemper, J. Benick, M. Hermle, The Irresistible Charm of a Simple Current Flow Pattern–25% with a Solar Cell Featuring a Full-Area Back Contact, In: 31st European PV Solar Energy Conference and Exhibition, 2015.
[212] C. Reichel, R. Müller, F. Feldmann, A. Richter, M. Hermle, S.W. Glunz, J. Appl. Phys. 122 (2017).
[213] C. Allebe, C. Ballif, J.J.D. Leon, A. Ingenito, A. Descoeudres, G. Nogay, P. Wyss, F.-J. Haug, M. Despeisse, S. Nicolay, PECVD Based Layers for Improved High Temperature Industrial Solar cell Processes, In: IEEE 46th Photovoltaic Specialists Conference, 2019.
[214] D. Yan, A. Cuevas, S.P. Phang, Y. Wan, D. Macdonald, Appl. Phys. Lett. 113 (2018), 061603.
[215] D. Yan, S.P. Phang, Y. Wan, C. Samundsett, D. Macdonald, A. Cuevas, Sol. Energy Mater. Sol. Cells 193 (2019) 80–84.
[216] S. Duttagupta, N. Nandakumar, R. Stangl, A.G. Aberle, In: IEEE 7th World Conference on Photovoltaic Energy Conversion, 2018, pp. 1991–1994.
[217] N. Nandakumar, J. Rodriguez, T. Kluge, T. Grosse, D. Landgraf, N. Balaji, M. Esber, P. Padhamnath, S. Duttagupta, 21.6% MonoPoly TM cells with in-situ Interfacial Oxide and Poly-Si Layers Deposited by Inline PECVD, In: IEEE 7th World Conference on Photovoltaic Energy Conversion, 2018.
[218] N. Nandakumar, J. Rodriguez, T. Kluge, T. Groβe, L. Fondop, P. Padhamnath, N. Balaji, M. König, S. Duttagupta, Prog. Photovolt. Res. Appl. 27 (2019) 107–112.
[219] N. Nandakumar, J. Rodriguez, T. Kluge, T. Grosse, L. Fondop, N. Balaji, P. Padhamnath, M. Konig, S. Duttagupta, Investigation of 23% MonoPoly Screen-Printed Silicon Solar Cells with an Industrial Rear Passivated Contact, In: IEEE 46th Photovoltaic Specialists Conference, 2019.
[220] P. Padhamnath, A. Khanna, N. Nandakumar, N. Nampalli, V. Shanmugam, A.G. Aberle, S. Duttagupta, Sol. Energy Mater. Sol. Cells 207 (2020), 110358.
[221] G. Yang, A. Ingenito, O. Isabella, M. Zeman, Sol. Energy Mater. Sol. Cells 158 (2016) 84–90.
[222] G. Yang, P. Guo, P. Procel, G. Limodio, A. Weeber, O. Isabella, M. Zeman, Sol. Energy Mater. Sol. Cells 186 (2018) 9–13.
[223] M.K. Stodolny, J. Anker, B.L.J. Geerligs, G.J.M. Janssen, B.W.H. Van De Loo, J. Melskens, R. Santbergen, O. Isabella, J. Schmitz, M. Lenes, J.M. Luchies, W.M.M. Kessels, I. Romijn, Energy Procedia 124 (2017) 635–642.
[224] P. Stradins, S. Essig, W. Nemeth, B.G. Lee, D. Young, A. Norman, Y. Liu, J.-w. Luo, E. Warren, A. Dameron, V. Lasalvia, M. Page, Y. Ok, Passivated Tunneling Contacts to N-Type Wafer Silicon and Their Implementation into High Performance Solar Cells Preprint, In: 6th World Conference on Photovoltaic Energy Conversion, 2014.
[225] W. Nemeth, V. Lasalvia, M.R. Page, E.L. Warren, A. Dameron, A.G. Norman, B.G. Lee, D.L. Young, P. Stradins, Implementation of Tunneling Pasivated Contacts into Industrially Relevant n-Cz Si Solar Cells, In: IEEE 42nd Photovoltaic Specialist Conference, 2015.
[226] D.L. Young, S. Theingi, V. LaSalvia, K. Chen, W. Nemeth, D. Findley, M. Page, P. Stradins, In: Self-Aligned, Selective Area Poly-Si/SiO_2 Passivated Contacts for Enhanced Photocurrent in Front/Back Solar Cells IEEE 46th Photovoltaic Specialists Conference, 2019.
[227] H. Park, S.J. Park, S. Bae, J.Y. Hyun, C.H. Lee, S.H. Shin, Y. Kang, H.S. Lee, D. Kim, Role of Polysilicon in Poly-Si/SiOx Passivating Contact Solar Cells, In: IEEE 7th World Conference on Photovoltaic Energy Conversion, 2018.
[228] H. Park, H. Park, S.J. Park, S. Bae, H. Kim, J.W. Yang, J.Y. Hyun, C.H. Lee, S.H. Shin, Y. Kang, H.-S. Lee, D. Kim, Sol. Energy Mater. Sol. Cells 189 (2019) 21–26.
[229] H.J. Park, Y. Lee, S.J. Park, S. Bae, S. Kim, D. Oh, J. Park, Y. Kim, H. Guim, Y. Kang, H.S. Lee, D. Kim, J. Yi, Prog. Photovolt. Res. Appl. 27 (2019) 1104–1114.
[230] Z. Zhang, Y. Zeng, C.-S. Jiang, Y. Huang, M. Liao, H. Tong, M. Al-Jassim, P. Gao, C. Shou, X. Zhou, B. Yan, J. Ye, Sol. Energy Mater. Sol. Cells 187 (2018) 113–122.
[231] Q. Yang, M. Liao, Z. Wang, J. Zheng, Y. lin, X. Guo, Z. Rui, D. Huang, L. Lu, M. Feng, P. Cheng, C. Shou, Y. Zeng, B. Yan, J. Ye, Sol. Energy Mater. Sol. Cells 210 (2020), 110518.
[232] V.U. Yuguo Tao, Chia-Wei Chen, Adam Payne, Elizabeth Lori Chang, A.U.a.A. Rohatgi, Prog. Photovolt. Res. Appl. 24 (2016) 830–835.
[233] G. Limodio, G. Yang, H. Ge, P. Procel, Y. De Groot, L. Mazzarella, O. Isabella, M. Zeman, Sol. Energy Mater. Sol. Cells 194 (2019) 28–35.
[234] P. Spinelli, M.A. Sen, E.G. Hoek, B.W.J. Kikkert, G. Yang, O. Isabella, A.W. Weeber, P.C.P. Bronsveld, AIP Conf. Proc. 1999 (2018), 040021.
[235] A. Onno, C. Chen, P. Koswatta, M. Boccard, Z.C. Holman, J. Appl. Phys. 126 (2019), 183103.
[236] V.L.D.L. Young, B. Nemeth, S. Theingi, A. Kale, D. Findley, J. Atkins, M. Page, P. Stradins, Front/Back Poly-Si/SiO_2 Passivated Contact Device with Voc & 720 mV, In: 35th European PV Solar Energy Conference and Exhibition, 2019.
[237] F. Feldmann, K.U. Ritzau, M. Bivour, A. Moldovan, S. Modi, J. Temmler, M. Hermle, S.W. Glunz, Energy Procedia 77 (2015) 263–270.
[238] R. Santbergen, G. Yang, P. Procel, G. Limodio, A. Weeber, O. Isabella, M. Zeman, Optical Analysis of Poly-Si and Poly-SiOx Carrier-Selective Passivating Contacts for c-Si Solar Cells, OSA Light, Energy and the Environment (2017).
[239] S. Reiter, N. Koper, R. Reineke-Koch, Y. Larionova, M. Turcu, J. Krügener, D. Tetzlaff, T. Wietler, U. Höhne, J.D. Kähler, R. Brendel, R. Peibst, Energy Procedia 92 (2016) 199–204.
[240] L. Mazzarella, P. Procel, Y. Zhao, G. Limodio, C. Han, G. Yang, A. Weeber, O. Isabella, M. Zeman, Insights into Charge Carrier Transport Mechanisms of SiO_2/Poly-SiCx/TCO Contact Structures for Si Solar Cells, In: 10th International Conference on Crystalline Silicon Photovoltaics, 2019.
[241] C. Han, L. Mazzarella, Y. Zhao, G. Yang, P. Procel, M. Tijssen, A. Montes, L. Spitaleri, A. Gulino, X. Zhang, O. Isabella, ACS Appl. Mater. Interfaces 11 (2019) 45586–45595.
[242] J.A.M.K. Stodolny, C.J.J. Tool, M. Koppes, A.A. Mewe, P. Manshanden, M. Lenes, I.G. Romijn, Novel Schemes of p^+ poly-Si Hydrogenation Implemented in Industrial 6'' Bifacial Front-and-Rear Passivating Contacts Solar Cells, In: 35th European PV Solar Energy Conference and Exhibition, 2018.
[243] G. Yang, P. Procel, C. Han, L. Mazzarella, M. Singh, A. Weeber, Ultra-thin Poly-Si Passivating Contacts for c-Si Solar Cells, In: 29th International Photovoltaic Science and Engineering Conference, 2019.
[244] J. Stuckelberger, D. Yan, S.P. Phang, C. Samundsett, D. Macdonald, Industrial Solar Cells Featuring Carrier Selective front Contacts, In: Aisa Pacific Solor Research Conference, 2019.
[245] R. Peibst, C. Kruse, S. Schäfer, V. Mertens, S. Bordihn, T. Dullweber, F. Haase, C. Hollemann, B. Lim, B. Min, R. Niepelt, H. Schulte-Huxel, R. Brendel, Prog. Photovolt. Res. Appl. (2019) https://doi.org/10.1002/pip.3201.
[246] C. Reichel, F. Granek, M. Hermle, S.W. Glunz, Prog. Photovolt. Res. Appl. 21 (2013) 1063–1076.
[247] A. Tomasi, B. Paviet-Salomon, Q. Jeangros, J. Haschke, G. Christmann, L. Barraud, A. Descoeudres, J.P. Seif, S. Nicolay, M. Despeisse, S. De Wolf, C. Ballif, Nat. Energy 2 (2017) 17062.

[248] K. Yoshikawa, H. Kawasaki, W. Yoshida, T. Irie, K. Konishi, K. Nakano, T. Uto, D. Adachi, M. Kanematsu, H. Uzu, K. Yamamoto, Nat. Energy 2 (2017) 17032.
[249] P.J. Cousins, D.D. Smith, H.C. Luan, J. Manning, T.D. Dennis, A. Waldhauer, K.E. Wilson, G. Harley, W.P. Mulligan, Generation 3: Improved Performance at Lower Cost, In: IEEE 35th Photovoltaic Specialists Conference, 2010.
[250] T.F.F. Feldmann, B. Steinhauser, H. Nagel, D. Ourinson, S. Mack, E. Lohmüller, J.-I. Polzin, J. Benick, A. Richter, A. Moldovan, M. Bivour, F. Clement, J. Rentsch, M. Hermle, S.W. Glunz, Large Area TOPCon Cells Realized by a PECVD Tube Process, In: 36th European PV Solar Energy Conference and Exhibition, 2019.
[251] P. Padhamnath, J. Wong, B. Nagarajan, J. Kitz, Sol. Energy Mater. Sol. Cells 192 (2018) 109–116.
[252] H.E. Çiftpınar, M.K. Stodolny, Y. Wu, G.J.M. Janssen, J. Löffler, J. Schmitz, M. Lenes, J.-M. Luchies, L.J. Geerligs, Energy Procedia 124 (2017) 851–861.
[253] A. Chaudhary, J. Hoß, J. Lossen, R.v. Swaaij, M. Zeman, AIP Conf. Proc. 2147 (2019), 040002.
[254] R. Peibst, Y. Larionova, S. Reiter, T.F. Wietler, N. Orlowski, S. Schafer, B. Min, M. Stratmann, D. Tetzlaff, J. Krugener, U. Hohne, J.D. Kahler, H. Mehlich, S. Frigge, R. Brendel, IEEE J. Photovolt. 8 (2018) 719–725.
[255] E. Bruhat, T. Desrues, D. Blanc-pélissier, B. Martel, AIP Conf. Proc. 2147 (2019), 040001.
[256] B. Grübel, G. Cimiotti, V. Arya, T. Fellmeth, F. Feldmann, B. Steinhauser, T. Kluge, D. Landgraf, M. Glatthaar, M.B. Gmbh, Plated Ni/Cu/Ag for TOPCon Solar Cell Metallization, In: 36th European PV Solar Energy Conference and Exhibition, 2019.
[257] F. Haase, T. Neubert, R. Horbelt, B. Terheiden, K. Bothe, R. Brendel, Sol. Energy Mater. Sol. Cells 95 (2011) 2698–2700.
[258] A.F. Christoph Messmer, Frank Feldmann, Jonas Schon, Martin Hemle, In: 36th European PV Solar Energy Conference and Exhibition, 2019.
[259] J. Solar, http://ir.jinkosolar.com/news-releases/news-release-details/jinkosolar-large-area-n-type-topcon-monocrystalline-silicon (2019).
[260] M. Stodolny, Y. Wu, J. Anker, X. Lu, J. Liu, P. Bronsveld, A. Mewe, G. Janssen, G. Coletti, K. Tool, B. Geerligs, J. Löffler, A. Weeber, PolySi Based Passivating Contacts Enabling Industrial Silicon Solar Cell Efficiencies up to 24 %, In: IEEE 46th Photovoltaic Specialists Conference, 2019.
[261] CanadianSolar, http://investors.canadiansolar.com/news-releases/news-release-details/canadian-solar-sets-2381-conversion-efficiency-world-record-n (2020).
[262] CanadianSolar, http://investors.canadiansolar.com/news-releases/news-release-details/canadian-solar-sets-2280-conversion-efficiency-world-record-p (2019).
[263] F. Feldmann, B. Steinhauser, V. Arya, A. Büchler, A.A. Brand, S. Kluska, M. Hermle, S.W. Glunz, Evaluation of Topcon Technology on Large Area Solar Cells, In: 33rd European PV Solar Energy Conference and Exhibition, 2017.
[264] A.B. Morales-vilches, Y. Larionova, T. Wietler, ZnO:Al/a-SiOx front Contact for Polycrystalline-Silicon-on-Oxide (POLO) Solar Cells, In: IEEE 8th International Conference on Crystalline Silicon Photovoltaics, 2018.
[265] Z. Zhang, Y. Zeng, Y. Huang, X. Guo, Z. Wang, Q. Yang, C. Shou, B. Yan, J. Ye, Improvement of Passivation Quality by Post-Crystallization Treatments with Different Methods for High Quality Tunnel Oxide Passivated Contact c-Si Solar Cells, In: IEEE 46th Photovoltaic Specialists Conference, 2019.
[266] D. Qiu, W. Duan, A. Lambertz, K. Bittkau, P. Steuter, Y. Liu, A. Gad, M. Pomaska, U. Rau, K. Ding, Sol. Energy Mater. Sol. Cells 209 (2020), 110471.
[267] D. Ding, G. Lu, Z. Li, Y. Zhang, W. Shen, Sol. Energy 193 (2019) 494–501.
[268] C. J., The Industrial Application of n-type Bifacial Passivating-Contact Technology, In: 9th International Conference on Crystalline Silicon Photovoltaics, 2019.
[269] Y. Yang, In: Recent Progress at Trina in Large Area IBC Cells with Passivated Contacts, nPV workshop, 2018.
[270] A. Mewe, M. Stodolny, J. Anker, M. Lenes, X. Pagès, Y. Wu, K. Tool, B. Geerligs, I. Romijn, AIP Conf. Proc. 1999 (2018).
[271] C. Hollemann, F. Haase, M. Rienäcker, V. Barnscheidt, J. Krügener, N. Folchert, R. Brendel, S. Richter, S. Großer, E. Sauter, J. Hübner, M. Oestreich, R. Peibst, Sci. Rep. 10 (2020) 658.
[272] K. Yoshikawa, W. Yoshida, T. Irie, H. Kawasaki, K. Konishi, H. Ishibashi, T. Asatani, D. Adachi, M. Kanematsu, H. Uzu, K. Yamamoto, Sol. Energy Mater. Sol. Cells 173 (2017) 37–42.
[273] X. Yang, K. Weber, Z. Hameiri, S. De Wolf, Prog. Photovolt. Res. Appl. 25 (2017) 896–904.
[274] S. Zhong, J. Dreon, Q. Jeangros, E. Aydin, S. De Wolf, F. Fu, M. Boccard, C. Ballif, Adv. Funct. Mater. 30 (2020), 1907840.
[275] X. Yang, Q. Bi, H. Ali, K. Davis, W.V. Schoenfeld, K. Weber, Adv. Mater. 28 (2016) 5891–5897.
[276] X. Yang, P. Zheng, Q. Bi, K. Weber, Sol. Energy Mater. Sol. Cells 150 (2016) 32–38.
[277] S. Avasthi, W.E. McClain, G. Man, A. Kahn, J. Schwartz, J.C. Sturm, Appl. Phys. Lett. 102 (2013), 203901.
[278] Y. Wan, C. Samundsett, J. Bullock, M. Hettick, T. Allen, D. Yan, J. Peng, Y. Wu, J. Cui, A. Javey, A. Cuevas, Adv. Energy Mater. 7 (2017), 1601863.
[279] G. Chistiakova, B. Macco, L. Korte, IEEE J. Photovolt. 10 (2020) 398–406.
[280] Y. Wan, S.K. Karuturi, C. Samundsett, J. Bullock, M. Hettick, D. Yan, J. Peng, P.R. Narangari, S. Mokkapati, H.H. Tan, C. Jagadish, A. Javey, A. Cuevas, ACS Energy Lett. 3 (2018) 125–131.
[281] B. Macco, L.E. Black, J. Melskens, B.W.H. van de Loo, W.-J.H. Berghuis, M.A. Verheijen, W.M.M. Kessels, Sol. Energy Mater. Sol. Cells 184 (2018) 98–104.
[282] B. Liao, B. Hoex, A.G. Aberle, D. Chi, C.S. Bhatia, Appl. Phys. Lett. 104 (2014), 253903.
[283] G. Sahasrabudhe, S.M. Rupich, J. Jhaveri, A.H. Berg, K.A. Nagamatsu, G. Man, Y.J. Chabal, A. Kahn, S. Wagner, J.C. Sturm, J. Schwartz, J. Am. Chem. Soc. 137 (2015) 14842–14845.
[284] J. Jhaveri, K.A. Nagamatsu, A.H. Berg, G. Man, G. Sahasrabudhe, S. Wagner, J. Schwartz, A. Kahn, J.C. Sturm, Double-Heterojunction Crystalline Silicon Solar Cell with Electron-Selective TiO_2 Cathode Contact Fabricated at 100°C with Open-Circuit Voltage of 640 mV, In: IEEE 42nd Photovoltaic Specialist Conference, 2015.
[285] M. Boccard, X. Yang, K. Weber, Z.C. Holman, Passivation and Carrier Selectivity of TiO_2 Contacts Combined with Different Passivation Layers and Electrodes for Silicon Solar Cells, In: IEEE 43rd Photovoltaic Specialists Conference, 2016.
[286] H. Ali, X. Yang, K. Weber, W.V. Schoenfeld, K.O. Davis, Microsc. Microanal. 23 (2017) 900–904.
[287] J. Bullock, Y. Wan, M. Hettick, X. Zhaoran, S.P. Phang, D. Yan, H. Wang, W. Ji, C. Samundsett, Z. Hameiri, D. Macdonald, A. Cuevas, A. Javey, Adv. Energy Mater. 9 (2019), 1803367.
[288] T.G. Allen, J. Bullock, Q. Jeangros, C. Samundsett, Y. Wan, J. Cui, A. Hessler-Wyser, S. De Wolf, A. Javey, A. Cuevas, Adv. Energy Mater. 7 (2017), 1602606.
[289] J. Cho, J. Melskens, M.R. Payo, M. Debucquoy, H.S. Radhakrishnan, I. Gordon, J. Szlufcik, W.M.M. Kessels, J. Poortmans, ACS Appl. Energy Mater. 2 (2019) 1393–1404.
[290] B. Hussain, Prog. Photovolt. Res. Appl. 25 (2017) 919–927.
[291] F. Wang, S. Zhao, B. Liu, Y. Li, Q. Ren, R. Du, N. Wang, C. Wei, X. Chen, G. Wang, B. Yan, Y. Zhao, X. Zhang, Nano Energy 39 (2017) 437–443.
[292] Z. Wang, Y. Yang, L. Zhang, H. Lin, Z. Zhang, D. Wang, S. Peng, D. He, J. Ye, P. Gao, Nano Energy 54 (2018) 99–105.
[293] J. Bullock, M. Hettick, J. Geissbühler, A.J. Ong, T. Allen, Carolin M. Sutter-Fella, T. Chen, H. Ota, E.W. Schaler, S. De Wolf, C. Ballif, A. Cuevas, A. Javey, Nat. Energy 1 (2016) 15031.
[294] J. Bullock, Y. Wan, Z. Xu, S. Essig, M. Hettick, H. Wang, W. Ji, M. Boccard, A. Cuevas, C. Ballif, A. Javey, ACS Energy Lett. 3 (2018) 508–513.
[295] J. Bullock, P. Zheng, Q. Jeangros, M. Tosun, M. Hettick, C.M. Sutter-Fella, Y. Wan, T. Allen, D. Yan, D. Macdonald, S. De Wolf, A. Hessler-Wyser, A. Cuevas, A. Javey, Adv. Energy Mater. 6 (2016), 1600241.
[296] Y. Wan, C. Samundsett, J. Bullock, T. Allen, M. Hettick, D. Yan, P. Zheng, X. Zhang, J. Cui, J. McKeon, A. Javey, A. Cuevas, ACS Appl. Mater. Interfaces 8 (2016) 14671–14677.
[297] W. Wu, W. Lin, S. Zhong, B. Paviet-Salomon, M. Despeisse, Q. Jeangros, Z. Liang, M. Boccard, H. Shen, C. Ballif, Phys. Status Solidi RRL 14 (2020), 1900688.
[298] Y. Wan, C. Samundsett, D. Yan, T. Allen, J. Peng, J. Cui, X. Zhang, J. Bullock, A. Cuevas, Appl. Phys. Lett. 109 (2016), 113901.
[299] H. Tong, Z.H. Yang, X.X. Wang, Z.L. Liu, Z.X. Chen, X.X. Ke, M.L. Sui, J. Tang, T.B. Yu, Z.Y. Ge, Y.H. Zeng, P.Q. Gao, J.C. Ye, Adv. Energy Mater. 8 (2018), 1702921.
[300] E. Nurlaela, A. Ziani, K. Takanabe, Mater. Renew. Sustain. Energy 5 (2016) 18.
[301] J.-S. Park, H.-S. Park, S.-W. Kang, J. Electrochem. Soc. 149 (2002) C28–C32.
[302] X. Yang, E. Aydin, H. Xu, J. Kang, M. Hedhili, W. Liu, Y. Wan, J. Peng, C. Samundsett, A. Cuevas, S. De Wolf, Adv. Energy Mater. 8 (2018), 1800608.
[303] X. Yang, W. Liu, M. De Bastiani, T. Allen, J. Kang, H. Xu, E. Aydin, L. Xu, Q. Bi, H. Dang, E. AlHabshi, K. Kotsovos, A. AlSaggaf, I. Gereige, Y. Wan, J. Peng, C. Samundsett, A. Cuevas, S. De Wolf, Joule 3 (2019) 1314–1327.
[304] D.B. Patel, H.-S. Kim, M. Patel, K.R. Chauhan, J.E. Park, D. Lim, J. Kim, Appl. Phys. Lett. 109 (2016), 133902.
[305] M. Xue, R. Islam, Y. Chen, J. Chen, C.-Y. Lu, A.M. Pleus, C. Tae, K. Xu, Y. Liu, T.I. Kamins, K.C. Saraswat, J.S. Harris, J. Appl. Phys. 123 (2018), 143101.
[306] P. Ravindra, R. Mukherjee, S. Avasthi, IEEE J. Photovolt. 7 (2017) 1278–1283.
[307] C. Battaglia, X. Yin, M. Zheng, I.D. Sharp, T. Chen, S. McDonnell, A. Azcatl, C. Carraro, B. Ma, R. Maboudian, R.M. Wallace, A. Javey, Nano Lett. 14 (2014) 967–971.
[308] C. Battaglia, S.M.d. Nicolás, S.D. Wolf, X. Yin, M. Zheng, C. Ballif, A. Javey, Appl. Phys. Lett. 104 (2014), 113902.
[309] J. Geissbühler, J. Werner, S.M.d. Nicolas, L. Barraud, A. Hessler-Wyser, M. Despeisse, S. Nicolay, A. Tomasi, B. Niesen, S.D. Wolf, C. Ballif, Appl. Phys. Lett. 107 (2015), 081601.

[310] L.G. Gerling, S. Mahato, A. Morales-Vilches, G. Masmitja, P. Ortega, C. Voz, R. Alcubilla, J. Puigdollers, Sol. Energy Mater. Sol. Cells 145 (2016) 109–115.
[311] G. Masmitjà, L.G. Gerling, P. Ortega, J. Puigdollers, I. Martín, C. Voz, R. Alcubilla, J. Mater. Chem. A 5 (2017) 9182–9189.
[312] G. Masmitjà, P. Ortega, J. Puigdollers, L.G. Gerling, I. Martín, C. Voz, R. Alcubilla, J. Mater. Chem. A 6 (2018) 3977–3985.
[313] M. Bivour, J. Temmler, H. Steinkemper, M. Hermle, Sol. Energy Mater. Sol. Cells 142 (2015) 34–41.
[314] M. Mews, L. Korte, B. Rech, Sol. Energy Mater. Sol. Cells 158 (2016) 77–83.
[315] S. Essig, J. Dréon, E. Rucavado, M. Mews, T. Koida, M. Boccard, J. Werner, J. Geissbühler, P. Löper, M. Morales-Masis, L. Korte, S. De Wolf, C. Ballif, Sol. RRL 2 (2018), 1700227.
[316] B. Macco, M.F.J. Vos, N.F.W. Thissen, A.A. Bol, W.M.M. Kessels, Phys. Status Solidi RRL 9 (2015) 393–396.
[317] M. Bivour, B. Macco, J. Temmler, W.M.M. Kessels, M. Hermle, Energy Procedia 92 (2016) 443–449.
[318] L.G. Gerling, S. Mahato, A. Morales-Vilches, G. Masmitja, P. Ortega, C. Voz, R. Alcubilla, J. Puigdollers, Sol. Energy Mater. Sol. Cells 145 (2016) 109–115.
[319] X. Yang, Atomic Layer Deposition of Vanadium Oxide as Hole-Selective Contact for Crystalline Silicon Solar Cells, In: 10th International Conference on Crystalline Silicon Photovoltaics, 2020.
[320] W. Lin, W. Wu, Z. Liu, K. Qiu, L. Cai, Z. Yao, B. Ai, Z. Liang, H. Shen, ACS Appl. Mater. Interfaces 10 (2018) 13645–13651.
[321] T. Zhang, C.-Y. Lee, Y. Wan, S. Lim, B. Hoex, J. Appl. Phys. 124 (2018), 073106.
[322] S. Cao, J. Li, Y. Lin, T. Pan, G. Du, J. Zhang, L. Yang, X. Chen, L. Lu, N. Min, M. Yin, D. Li, Sol. RRL 3 (2019), 1900274.
[323] J. Bullock, C. Samundsett, A. Cuevas, D. Yan, Y. Wan, T. Allen, IEEE J. Photovolt. 5 (2015) 1591–1594.
[324] D. Zielke, C. Niehaves, W. Lövenich, A. Elschner, M. Hörteis, J. Schmidt, Energy Procedia 77 (2015) 331–339.
[325] M.J. Sailor, E.J. Ginsburg, C.B. Gorman, A. Kumar, R.H. Grubbs, N.S. Lewis, Science 249 (1990) 1146–1150.
[326] V. Gowrishankar, S.R. Scully, M.D. McGehee, Q. Wang, H.M. Branz, Appl. Phys. Lett. 89 (2006), 252102.
[327] C.-Y. Liu, Z.C. Holman, U.R. Kortshagen, Nano Lett. 9 (2009) 449–452.
[328] S.-C. Shiu, J.-J. Chao, S.-C. Hung, C.-L. Yeh, C.-F. Lin, Chem. Mater. 22 (2010) 3108–3113.
[329] W. Ji, T. Allen, X. Yang, G. Zeng, S. De Wolf, A. Javey, ACS Energy Lett. 5 (2020) 897–902.
[330] X. Shen, B. Sun, D. Liu, S.T. Lee, J. Am. Chem. Soc. 133 (2011) 19408–19415.
[331] S. Avasthi, S. Lee, Y.L. Loo, J.C. Sturm, Adv. Mater. 23 (2011) 5762–5766.
[332] W.R. Wei, M.L. Tsai, S.T. Ho, S.H. Tai, C.R. Ho, S.H. Tsai, C.W. Liu, R.J. Chung, J.H. He, Nano Lett 13 (2013) 3658–3663.
[333] P. Yu, C.-Y. Tsai, J.-K. Chang, C.-C. Lai, P.-H. Chen, Y.-C. Lai, P.-T. Tsai, M.-C. Li, H.-T. Pan, Y.-Y. Huang, C.-I. Wu, Y.-L. Chueh, S.-W. Chen, C.-H. Du, S.-F. Horng, H.-F. Meng, ACS Nano 7 (2013) 10780–10787.
[334] R. Liu, S.T. Lee, B. Sun, Adv. Mater. 26 (2014) 6007–6012.
[335] J. Zhang, T. Song, X. Shen, X. Yu, S.-T. Lee, B. Sun, ACS Nano 8 (2014) 11369–11376.
[336] K.T. Park, H.J. Kim, M.J. Park, J.H. Jeong, J. Lee, D.G. Choi, J.H. Lee, J.H. Choi, Sci. Rep. 5 (2015) 12093.
[337] Q. Liu, R. Ishikawa, S. Funada, T. Ohki, K. Ueno, H. Shirai, Adv. Energy Mater. 5 (2015), 1500744.
[338] Y.T. Lee, F.R. Lin, C.H. Chen, Z. Pei, ACS Appl. Mater. Interfaces 8 (2016) 34537–34545.
[339] J.P. Thomas, K.T. Leung, J. Mater. Chem. A 4 (2016) 17537–17542.
[340] S. Wu, W. Cui, N. Aghdassi, T. Song, S. Duhm, S.-T. Lee, B. Sun, Adv. Funct. Mater. 26 (2016) 5035–5041.
[341] X. Zhang, D. Yang, Z. Yang, X. Guo, B. Liu, X. Ren, S.F. Liu, Sci. Rep. 6 (2016) 35091.
[342] Y. Han, Y. Liu, J. Yuan, H. Dong, Y. Li, W. Ma, S.T. Lee, B. Sun, ACS Nano 11 (2017) 7215–7222.
[343] J. He, P. Gao, Z. Yang, J. Yu, W. Yu, Y. Zhang, J. Sheng, J. Ye, J.C. Amine, Y. Cui, Adv. Mater. 29 (2017), 1606321.
[344] J. Liu, Y. Ji, Y. Liu, Z. Xia, Y. Han, Y. Li, B. Sun, Adv. Energy Mater. 7 (2017), 1700311.
[345] J. He, Y. Wan, P. Gao, J. Tang, J. Ye, Adv. Funct. Mater. 28 (2018), 1802192.
[346] J. He, W. Zhang, J. Ye, P. Gao, Nano Energy 43 (2018) 117–123.
[347] S.-S. Yoon, D.-Y. Khang, Adv. Energy Mater. 8 (2018), 1702655.
[348] J. He, M.A. Hossain, H. Lin, W. Wang, S.K. Karuturi, B. Hoex, J. Ye, P. Gao, J. Bullock, Y. Wan, ACS Nano 13 (2019) 6356–6362.
[349] J. Ouyang, Displays 34 (2013) 423–436.
[350] Y. Wang, C. Zhu, R. Pfattner, H. Yan, L. Jin, S. Chen, F. Molina-Lopez, F. Lissel, J. Liu, N.I. Rabiah, Z. Chen, J.W. Chung, C. Linder, M.F. Toney, B. Murmann, Z. Bao, Sci. Adv. 3 (2017), e1602076.
[351] J.P. Thomas, K.T. Leung, Adv. Funct. Mater. 24 (2014) 4978–4985.
[352] J.P. Thomas, L. Zhao, D. McGillivray, K.T. Leung, J. Mater. Chem. A 2 (2014) 2383–2389.
[353] J.P. Thomas, S. Srivastava, L. Zhao, M. Abd-Ellah, D. McGillivray, J.S. Kang, M.A. Rahman, N. Moghimi, N.F. Heinig, K.T. Leung, ACS Appl. Mater. Interfaces 7 (2015) 7466–7470.
[354] Y. Zhu, T. Song, F. Zhang, S.-T. Lee, B. Sun, Appl. Phys. Lett. 102 (2013), 113504.
[355] Q. Fan, Q. Zhang, W. Zhou, X. Xia, F. Yang, N. Zhang, S. Xiao, K. Li, X. Gu, Z. Xiao, H. Chen, Y. Wang, H. Liu, W. Zhou, S. Xie, Nano Energy 33 (2017) 436–444.
[356] J.P. Thomas, M.A. Rahman, S. Srivastava, J.S. Kang, D. McGillivray, M. Abd-Ellah, N.F. Heinig, K.T. Leung, ACS Nano 12 (2018) 9495–9503.
[357] N. Kim, B.H. Lee, D. Choi, G. Kim, H. Kim, J.R. Kim, J. Lee, Y.H. Kahng, K. Lee, Phys. Rev. Lett. 109 (2012), 106405.
[358] S. Jackle, M. Mattiza, M. Liebhaber, G. Bronstrup, M. Rommel, K. Lips, S. Christiansen, Sci. Rep. 5 (2015) 13008.
[359] M. Pietsch, S. Jäckle, S. Christiansen, Appl. Phys. A 115 (2014) 1109–1113.
[360] X. Fang, T. Song, R. Liu, B. Sun, J. Phys. Chem. C 118 (2014) 20238–20245.
[361] Y. Liu, Z.G. Zhang, Z. Xia, J. Zhang, Y. Liu, F. Liang, Y. Li, T. Song, X. Yu, S.T. Lee, B. Sun, ACS Nano 10 (2016) 704–712.
[362] A.S. Erickson, A. Zohar, D. Cahen, Adv. Energy Mater. 4 (2014), 1301724.
[363] X. Mu, X. Yu, D. Xu, X. Shen, Z. Xia, H. He, H. Zhu, J. Xie, B. Sun, D. Yang, Nano Energy 16 (2015) 54–61.
[364] J. He, P. Gao, Z. Ling, L. Ding, Z. Yang, J. Ye, Y. Cui, ACS Nano 10 (2016) 11525–11531.
[365] X. Yu, X. Shen, X. Mu, J. Zhang, B. Sun, L. Zeng, L. Yang, Y. Wu, H. He, D. Yang, Sci. Rep. 5 (2015) 17371.
[366] T.-G. Chen, B.-Y. Huang, E.-C. Chen, P. Yu, H.-F. Meng, Appl. Phys. Lett. 101 (2012), 033301.
[367] L. He, D. Lai, H. Wang, C. Jiang, Rusli, Small 8 (2012) 1664–1668.
[368] S. Jeong, E.C. Garnett, S. Wang, Z. Yu, S. Fan, M.L. Brongersma, M.D. McGehee, Y. Cui, Nano Lett. 12 (2012) 2971–2976.
[369] P.R. Pudasaini, F. Ruiz-Zepeda, M. Sharma, D. Elam, A. Ponce, A.A. Ayon, ACS Appl. Mater. Interfaces 5 (2013) 9620–9627.
[370] H. Jeong, H. Song, Y. Pak, I.K. Kwon, K. Jo, H. Lee, G.Y. Jung, Adv. Mater. 26 (2014) 3445–3450.
[371] Z. Wang, S. Peng, Y. Wen, T. Qin, Q. Liu, D. He, G. Cao, Nano Energy 41 (2017) 519–526.
[372] J. He, Z. Yang, P. Liu, S. Wu, P. Gao, M. Wang, S. Zhou, X. Li, H. Cao, J. Ye, Adv. Energy Mater. 6 (2016), 1501793.
[373] J. Melskens, B.W. van de Loo, B. Macco, M.F. Vos, J. Palmans, S. Smit, W. Kessels, Concepts and Prospects of Passivating Contacts for Crystalline Silicon Solar Cells, In: IEEE 42nd Photovoltaic Specialist Conference, 2015.
[374] S. Olibet, E. Vallat-Sauvain, C. Ballif, Phys. Rev. B 76 (2007), 035326.
[375] K.T. Wong, N.S. Lewis, Acc. Chem. Res. 47 (2014) 3037–3044.
[376] F. Zhang, B. Sun, T. Song, X. Zhu, S. Lee, Chem. Mater. 23 (2011) 2084–2090.
[377] F. Zhang, D. Liu, Y. Zhang, H. Wei, T. Song, B. Sun, ACS Appl. Mater. Interfaces 5 (2013) 4678–4684.
[378] J. Zhang, Y. Zhang, F. Zhang, B. Sun, Appl. Phys. Lett. 102 (2013), 013501.
[379] J. Oh, H.C. Yuan, H.M. Branz, Nat. Nanotechnol. 7 (2012) 743–748.
[380] A.S. Erickson, N.K. Kedem, A.E. Haj-Yahia, D. Cahen, Appl. Phys. Lett. 101 (2012), 233901.
[381] Y. Liu, J. Zhang, H. Wu, W. Cui, R. Wang, K. Ding, S.-T. Lee, B. Sun, Nano Energy 34 (2017) 257–263.
[382] Y.T. Lee, F.R. Lin, C.H. Chen, Z. Pei, ACS Appl Mater Interfaces 8 (2016) 34537–34545.
[383] K.A. Nagamatsu, S. Avasthi, G. Sahasrabudhe, G. Man, J. Jhaveri, A.H. Berg, J. Schwartz, A. Kahn, S. Wagner, J.C. Sturm, Appl. Phys. Lett. 106 (2015), 123906.
[384] Y.S. Kou, S.T. Yang, S. Thiyagu, C.T. Liu, J.W. Wu, C.F. Lin, Nanoscale 8 (2016) 5379–5385.
[385] D. Zielke, A. Pazidis, F. Werner, J. Schmidt, Sol. Energy Mater. Sol. Cells 131 (2014) 110–116.
[386] K.W. Chang, K.W. Sun, Org. Electron. 55 (2018) 82–89.
[387] D. Zielke, R. Gogolin, M.-U. Halbich, C. Marquardt, W. Lövenich, R. Sauer, J. Schmidt, Sol. RRL 2 (2018), 1700191.
[388] M.U. Halbich, D. Zielke, R. Gogolin, R. Sauer-Stieglitz, W. Lovenich, J. Schmidt, Sci. Rep. 9 (2019) 9775.
[389] Y. Zhang, F. Zu, S.-T. Lee, L. Liao, N. Zhao, B. Sun, Adv. Energy Mater. 4 (2014), 1300923.
[390] D. Wang, J. Sheng, S. Wu, J. Zhu, S. Chen, P. Gao, J. Ye, Appl. Phys. Lett. 109 (2016), 043901.
[391] F. Dross, A. Milhe, J. Robbelein, I. Gordon, P. Bouchard, G. Beaucarne, J. Poortmans, Stress-Induced Lift-Off Method for Kerf-Loss-Free Wafering of Ultra-thin (~50 μm) Crystalline Si Wafers, In: IEEE 33rd Photovoltaic Specialists Conference, 2008.
[392] A. Mavrokefalos, S.E. Han, S. Yerci, M.S. Branham, G. Chen, Nano Lett. 12 (2012) 2792–2796.
[393] L. He, C. Jiang, H. Wang, D. Lai, Y. Heng Tan, C. Seng Tan, Rusli, Appl. Phys. Lett. 100 (2012), 103104.
[394] J. Zhang, Y. Zhang, T. Song, X. Shen, X. Yu, S.T. Lee, B. Sun, B. Jia, ACS Appl. Mater. Interfaces 9 (2017) 21723–21729.

[395] M. Sharma, P.R. Pudasaini, F. Ruiz-Zepeda, D. Elam, A.A. Ayon, ACS Appl. Mater. Interfaces 6 (2014) 4356–4363.
[396] S. Thiyagu, C.C. Hsueh, C.T. Liu, H.J. Syu, T.C. Lin, C.F. Lin, Nanoscale 6 (2014) 3361–3366.
[397] J. He, P. Gao, M. Liao, X. Yang, Z. Ying, S. Zhou, J. Ye, Y. Cui, ACS Nano 9 (2015) 6522–6531.
[398] X. Crispin, F.L.E. Jakobsson, A. Crispin, P.C.M. Grim, P. Andersson, A. Volodin, C. van Haesendonck, M. Van der Auweraer, W.R. Salaneck, M. Berggren, Chem. Mater. 18 (2006) 4354–4360.
[399] T. Miyasaka, T.N. Murakami, Appl. Phys. Lett. 85 (2004) 3932–3934.
[400] X. Chen, H. Sun, Z. Yang, G. Guan, Z. Zhang, L. Qiu, H. Peng, J. Mater. Chem. A 2 (2014) 1897–1902.
[401] Y. Fu, H. Wu, S. Ye, X. Cai, X. Yu, S. Hou, H. Kafafy, D. Zou, Energy Environ. Sci. 6 (2013) 805–812.
[402] L. Zheng, Z.-H. Lin, G. Cheng, W. Wu, X. Wen, S. Lee, Z.L. Wang, Nano Energy 9 (2014) 291–300.
[403] L. Zheng, G. Cheng, J. Chen, L. Lin, J. Wang, Y. Liu, H. Li, Z.L. Wang, Adv. Energy Mater. 5 (2015), 1501152.
[404] Q. Tang, X. Wang, P. Yang, B. He, Angew. Chem. Int. Ed. 55 (2016) 5243–5246.
[405] Z. Wen, M.H. Yeh, H. Guo, J. Wang, Y. Zi, W. Xu, J. Deng, L. Zhu, X. Wang, C. Hu, L. Zhu, X. Sun, Z.L. Wang, Sci. Adv. 2 (2016), e1600097.
[406] R. Liu, J. Wang, T. Sun, M. Wang, C. Wu, H. Zou, T. Song, X. Zhang, S.T. Lee, Z.L. Wang, B. Sun, Nano Lett. 17 (2017) 4240–4247.
[407] Y. Liu, N. Sun, J. Liu, Z. Wen, X. Sun, S.T. Lee, B. Sun, ACS Nano 12 (2018) 2893–2899.
[408] M. Xu, T. Liang, M. Shi, H. Chen, Chem. Rev. 113 (2013) 3766–3798.
[409] A. Gupta, T. Sakthivel, S. Seal, Prog. Mater Sci. 73 (2015) 44–126.
[410] E. Lhuillier, S. Pedetti, S. Ithurria, B. Nadal, H. Heuclin, B. Dubertret, Acc. Chem. Res. 48 (2015) 22–30.
[411] B. Peng, P.K. Ang, K.P. Loh, Nano Today 10 (2015) 128–137.
[412] G. Fiori, F. Bonaccorso, G. Iannaccone, T. Palacios, D. Neumaier, A. Seabaugh, S.K. Banerjee, L. Colombo, Nat. Nanotechnol. 9 (2014) 768–779.
[413] D. Sinha, J.U. Lee, Nano Lett. 14 (2014) 4660–4664.
[414] X. Li, H. Zhu, K. Wang, A. Cao, J. Wei, C. Li, Y. Jia, Z. Li, X. Li, D. Wu, Adv. Mater. 22 (2010) 2743–2748.
[415] X. Miao, S. Tongay, M.K. Petterson, K. Berke, A.G. Rinzler, B.R. Appleton, A.F. Hebard, Nano Lett. 12 (2012) 2745–2750.
[416] T. Cui, R. Lv, Z.-H. Huang, S. Chen, Z. Zhang, X. Gan, Y. Jia, X. Li, K. Wang, D. Wu, F. Kang, J. Mater. Chem. A 1 (2013) 5736.
[417] E. Shi, H. Li, L. Yang, L. Zhang, Z. Li, P. Li, Y. Shang, S. Wu, X. Li, J. Wei, K. Wang, H. Zhu, D. Wu, Y. Fang, A. Cao, Nano Lett. 13 (2013) 1776–1781.
[418] X.Z. Zhang, C. Xie, J.S. Jie, X.W. Zhang, Y.M. Wu, W.J. Zhang, J. Mater. Chem. A 1 (2013) 6593–6601.
[419] D. Xu, X. Yu, D. Gao, C. Li, M. Zhong, H. Zhu, S. Yuan, Z. Lin, D. Yang, J. Mater. Chem. A 4 (2016) 10558–10565.
[420] S.K. Pradhan, B. Xiao, A.K. Pradhan, Sol. Energy Mater. Sol. Cells 144 (2016) 117–127.
[421] S.B. Kang, K.C. Kwon, K.S. Choi, R. Lee, K. Hong, J.M. Suh, M.J. Im, A. Sanger, I.Y. Choi, S.Y. Kim, J.C. Shin, H.W. Jang, K.J. Choi, Nano Energy 50 (2018) 649–658.
[422] H. Xu, L. Xin, L. Liu, D. Pang, Y. Jiao, R. Cong, W. Yu, Mater. Lett. 238 (2019) 13–16.
[423] M.-L. Tsai, S.-H. Su, J.-K. Chang, D.-S. Tsai, C.-H. Chen, C.-I. Wu, L.-J. Li, L.-J. Chen, J.-H. He, ACS Nano 8 (2014) 8317–8322.
[424] L.Z. Hao, W. Gao, Y.J. Liu, Z.D. Han, Q.Z. Xue, W.Y. Guo, J. Zhu, Y.R. Li, Nanoscale 7 (2015) 8304–8308.
[425] A.U. Rehman, M.F. Khan, M.A. Shehzad, S. Hussain, M.F. Bhopal, S.H. Lee, J. Eom, Y. Seo, J. Jung, S.H. Lee, ACS Appl. Mater. Interfaces 8 (2016) 29383–29390.
[426] M. Naguib, V.N. Mochalin, M.W. Barsoum, Y. Gogotsi, Adv. Mater. 26 (2014) 992–1005.
[427] Y. Liu, H. Xiao, W.A. Goddard 3rd, J. Am. Chem. Soc. 138 (2016) 15853–15856.
[428] L.P. Yu, A.S.R. Bati, T.S.L. Grace, M. Batmunkh, J.G. Shapter, Adv. Energy Mater. 9 (2019), 1901063.
[429] A. Richter, M. Hermle, S.W. Glunz, IEEE J. Photovolt. 3 (2013) 1184–1191.
[430] T.P. White, N.N. Lal, K.R. Catchpole, IEEE J. Photovolt. 4 (2014) 208–214.
[431] M.T. Hörantner, H. Snaith, Energy Environ. Sci. 10 (2017) 1983–1993.
[432] J. Werner, B. Niesen, C. Ballif, Adv. Mater. Interfaces 5 (2018), 1700731.
[433] M.A. Green, E.D. Dunlop, D.H. Levi, J. Hohl-Ebinger, M. Yoshita, A.W.Y. Ho-Baillie, Prog. Photovolt. Res. Appl. 27 (2019) 565–575.
[434] J.P. Mailoa, C.D. Bailie, E.C. Johlin, E.T. Hoke, A.J. Akey, W.H. Nguyen, M.D. Mcgehee, T. Buonassisi, Appl. Phys. Lett. 106 (2015), 121105.
[435] S. Albrecht, M. Saliba, J.P. Correa Baena, F. Lang, L. Kegelmann, M. Mews, L. Steier, A. Abate, J. Rappich, L. Korte, R. Schlatmann, M.K. Nazeeruddin, A. Hagfeldt, M. Grätzel, B. Rech, Energy Environ. Sci. 9 (2016) 81–88.
[436] J. Werner, C.H. Weng, A. Walter, L. Fesquet, J.P. Seif, S. De Wolf, B. Niesen, C. Ballif, J. Phys. Chem. Lett. 7 (2016) 161–166.
[437] K.A. Bush, A.F. Palmstrom, Z.J. Yu, M. Boccard, R. Cheacharoen, J.P. Mailoa, D.P. McMeekin, R.L.Z. Hoye, C.D. Bailie, T. Leijtens, I.M. Peters, M.C. Minichetti, N. Rolston, R. Prasanna, S. Sofia, D. Harwood, W. Ma, F. Moghadam, H.J. Snaith, T. Buonassisi, Z.C. Holman, S.F. Bent, M.D. McGehee, Nat. Energy 2 (2017) 17009.
[438] F. Sahli, J. Werner, B.A. Kamino, M. Bräuninger, R. Monnard, B. Paviet-Salomon, L. Barraud, L. Ding, J.J. Diaz Leon, D. Sacchetto, G. Cattaneo, M. Despeisse, M. Boccard, S. Nicolay, Q. Jeangros, B. Niesen, C. Ballif, Nat. Mater. 17 (2018) 820–826.
[439] OxfordPV, Oxford PV sets world record for perovskite solar cell, in: https://www.oxfordpv.com/news/oxford-pv-sets-world-record-perovskite-solar-cell, 2018.
[440] OxfordPV, Oxford PV perovskite solar cell achieves 28% efficiency, in: https://www.oxfordpv.com/news/oxford-pv-perovskite-solar-cell-achieves-28-efficiency, 2018.
[441] P. Löper, S.-J. Moon, S. Martín de Nicolas, B. Niesen, M. Ledinsky, S. Nicolay, J. Bailat, J.-H. Yum, S. De Wolf, C. Ballif, Phys. Chem. Chem. Phys. 17 (2015) 1619–1629.
[442] C.D. Bailie, M.G. Christoforo, J.P. Mailoa, A.R. Bowring, E.L. Unger, W.H. Nguyen, J. Burschka, N. Pellet, J.Z. Lee, M. Grätzel, R. Noufi, T. Buonassisi, A. Salleo, M.D. McGehee, Energy Environ. Sci. 8 (2015) 956–963.
[443] J. Werner, G. Dubuis, A. Walter, P. Löper, S.J. Moon, S. Nicolay, M. Morales-Masis, S. De Wolf, B. Niesen, C. Ballif, Sol. Energy Mater. Sol. Cells 141 (2015) 407–413.
[444] D.P. McMeekin, G. Sadoughi, W. Rehman, G.E. Eperon, M. Saliba, M.T. Hörantner, A. Haghighirad, N. Sakai, L. Korte, B. Rech, M.B. Johnston, L.M. Herz, H.J. Snaith, Science 351 (2016) 151–155.
[445] T. Duong, N. Lal, D. Grant, D. Jacobs, P. Zheng, S. Rahman, H. Shen, M. Stocks, A. Blakers, K. Weber, T.P. White, K.R. Catchpole, IEEE J. Photovolt. 6 (2016) 679–687.
[446] B. Chen, Y. Bai, Z. Yu, T. Li, X. Zheng, Q. Dong, L. Shen, M. Boccard, A. Gruverman, Z. Holman, J. Huang, Adv. Energy Mater. 6 (2016), 1601128.
[447] J.r.m. Werner, L. Barraud, A. Walter, M. Bräuninger, F. Sahli, D. Sacchetto, N. Tétreault, B. Paviet-Salomon, S.-J. Moon, C. Allebé, M. Despeisse, S. Nicolay, S.D. Wolf, B. Niesen, C. Ballif, ACS Energy Lett. 1 (2016) 474–480.
[448] T. Duong, Y. Wu, H. Shen, J. Peng, X. Fu, D. Jacobs, E.C. Wang, T.C. Kho, K.C. Fong, M. Stocks, E. Franklin, A. Blakers, N. Zin, K. McIntosh, W. Li, Y.B. Cheng, T.P. White, K. Weber, K. Catchpole, Adv. Energy Mater. 7 (2017), 1700228.
[449] C.O. Ramírez Quiroz, Y. Shen, M. Salvador, K. Forberich, N. Schrenker, G.D. Spyropoulos, T. Heumüller, B. Wilkinson, T. Kirchartz, E. Spiecker, P.J. Verlinden, X. Zhang, M.A. Green, A. Ho-Baillie, C.J. Brabec, J. Mater. Chem. A 6 (2018) 3583–3592.
[450] M. Jaysankar, B.A.L. Raul, J. Bastos, C. Burgess, C. Weijtens, M. Creatore, T. Aernouts, Y. Kuang, R. Gehlhaar, A. Hadipour, J. Poortmans, ACS Energy Lett. 4 (2019) 259–264.
[451] T. Duong, H. Pham, T.C. Kho, P. Phang, K.C. Fong, D. Yan, Y. Yin, J. Peng, M.A. Mahmud, S. Gharibzadeh, B.A. Nejand, I.M. Hossain, M.R. Khan, N. Mozaffari, Y. Wu, H. Shen, J. Zheng, H. Mai, W. Liang, C. Samundsett, M. Stocks, K. McIntosh, G.G. Andersson, U. Lemmer, B.S. Richards, U.W. Paetzold, A. Ho-Ballie, Y. Liu, D. Macdonald, A. Blakers, J. Wong-Leung, T. White, K. Weber, K. Catchpole, Adv. Energy Mater. 10 (2020), 1903553.
[452] B. Chen, S.-W. Baek, Y. Hou, E. Aydin, M. De Bastiani, B. Scheffel, A. Proppe, Z. Huang, M. Wei, Y.-K. Wang, E.-H. Jung, T.G. Allen, E. Van Kerschaver, F.P. García de Arquer, M.I. Saidaminov, S. Hoogland, S. De Wolf, E.H. Sargent, Nat. Commun. 11 (2020) 1257.
[453] J. Werner, A. Walter, E. Rucavado, S.-J. Moon, D. Sacchetto, M. Rienaecker, R. Peibst, R. Brendel, X. Niquille, S.D. Wolf, P. Löper, M. Morales-Masis, S. Nicolay, B. Niesen, C. Ballif, Appl. Phys. Lett. 109 (2016), 233902.
[454] Y. Wu, D. Yan, J. Peng, T. Duong, Y. Wan, P. Phang, H. Shen, N. Wu, C. Barugkin, X. Fu, S. Surve, D. Walter, T. White, K. Catchpole, K. Weber, Energy Environ. Sci. 10 (2017) 2472–2479.
[455] R. Fan, N. Zhou, L. Zhang, R. Yang, Y. Meng, L. Li, T. Guo, Y. Chen, Z. Xu, G. Zheng, Y. Huang, L. Li, L. Qin, X. Qiu, Q. Chen, H. Zhou, Solar RRL 1 (2017), 1700149.
[456] J. Zheng, C.F.J. Lau, H. Mehrvarz, F.-J. Ma, Y. Jiang, X. Deng, A. Soeriyadi, J. Kim, M. Zhang, L. Hu, X. Cui, D.S. Lee, J. Bing, Y. Cho, C. Chen, M.A. Green, S. Huang, A.W.Y. Ho-Baillie, Energy Environ. Sci. 11 (2018) 2432–2443.
[457] J. Zheng, H. Mehrvarz, F.J. Ma, C.F.J. Lau, M.A. Green, S. Huang, A.W.Y. Ho-Baillie, ACS Energy Lett. 3 (2018) 2299–2300.
[458] H. Shen, S.T. Omelchenko, D.A. Jacobs, S. Yalamanchili, Y. Wan, D. Yan, P. Phang, T. Duong, Y. Wu, Y. Yin, C. Samundsett, J. Peng, N. Wu, T.P. White, G.G. Andersson, N.S. Lewis, K.R. Catchpole, Sci. Adv. 4 (2018), eaau9711.
[459] Y. Wu, A. Fell, K.J. Weber, Sol. RRL 2 (2018), 1800193.
[460] G. Nogay, F. Sahli, J. Werner, R. Monnard, M. Boccard, M. Despeisse, F.J. Haug, Q. Jeangros, A. Ingenito, C. Ballif, ACS Energy Lett. 4 (2019) 844–845.
[461] T. Sameshima, J. Takenezawa, M. Hasumi, T. Koida, T. Kaneko, M. Karasawa, M. Kondo, Jpn. J. Appl. Phys. 50 (2011) 2–6.

[462] C.O. Ramírez Quiroz, G.D. Spyropoulos, M. Salvador, L.M. Roch, M. Berlinghof, J. Darío Perea, K. Forberich, L.I. Dion-Bertrand, N.J. Schrenker, A. Classen, N. Gasparini, G. Chistiakova, M. Mews, L. Korte, B. Rech, N. Li, F. Hauke, E. Spiecker, T. Ameri, S. Albrecht, G. Abellán, S. León, T. Unruh, A. Hirsch, A. Aspuru-Guzik, C.J. Brabec, Adv. Funct. Mater. 29 (2019), 1901476.
[463] T.R. Klein, B.G. Lee, M. Schnabel, E.L. Warren, P. Stradins, A.C. Tamboli, M.F.A.M.V. Hest, ACS Appl. Mater. Interfaces 10 (2018) 8086–8091.
[464] I.Y. Choi, C.U. Kim, W. Park, H. Lee, M.H. Song, K.K. Hong, S.I. Seok, K.J. Choi, Nano Energy 65 (2019), 104044.
[465] E. Lamanna, F. Matteocci, E. Calabrò, L. Serenelli, E. Salza, L. Martini, F. Menchini, M. Izzi, A. Agresti, S. Pescetelli, S. Bellani, A.E. Del Río Castillo, F. Bonaccorso, M. Tucci, A. Di Carlo, Joule 4 (2020) 865–881.
[466] B. Chen, Z.J. Yu, S. Manzoor, S. Wang, W. Weigand, Z. Yu, G. Yang, Z. Ni, X. Dai, Z.C. Holman, J. Huang, Joule 4 (2020) 850–864.
[467] Y. Hou, E. Aydin, M. De Bastiani, C. Xiao, F.H. Isikgor, D.J. Xue, B. Chen, H. Chen, B. Bahrami, A.H. Chowdhury, A. Johnston, S.W. Baek, Z. Huang, M. Wei, Y. Dong, J. Troughton, R. Jalmood, A.J. Mirabelli, T.G. Allen, E. Van Kerschaver, M.I. Saidaminov, D. Baran, Q. Qiao, K. Zhu, S. De Wolf, E.H. Sargent, Science 367 (2020) 1135–1140.
[468] C. Ulbrich, A. Gerber, K. Hermans, A. Lambertz, U. Rau, Prog. Photovolt. Res. Appl. 21 (2013) 1672–1681.
[469] J. Escarré, K. Söderström, M. Despeisse, S. Nicolay, C. Battaglia, G. Bugnon, L. Ding, F. Meillaud, F.J. Haug, C. Ballif, Sol. Energy Mater. Sol. Cells 98 (2012) 185–190.
[470] F. Sahli, B.A. Kamino, J. Werner, M. Bräuninger, B. Paviet-Salomon, L. Barraud, R. Monnard, J.P. Seif, A. Tomasi, Q. Jeangros, A. Hessler-Wyser, S. De Wolf, M. Despeisse, S. Nicolay, B. Niesen, C. Ballif, Adv. Energy Mater. 8 (2018), 1701609.
[471] K.A. Bush, S. Manzoor, K. Frohna, Z.J. Yu, J.A. Raiford, A.F. Palmstrom, H.-P. Wang, R. Prasanna, S.F. Bent, Z.C. Holman, M.D. McGehee, ACS Energy Lett. 3 (2018) 2173–2180.
[472] K. Li, Y. Zhang, H. Zhen, H. Wang, S. Liu, F. Yan, Z. Zheng, J. Mater. Chem. A 5 (2017) 969–974.
[473] R. Schmager, B. Fritz, R. Hünig, K. Ding, U. Lemmer, B.S. Richards, G. Gomard, U.W. Paetzold, ACS Photonics 4 (2017) 2687–2692.
[474] D.T. Grant, K.R. Catchpole, K.J. Weber, T.P. White, Opt. Express 24 (2016) A1454–A1470.
[475] M. Filipič, P. Löper, B. Niesen, S.D. Wolf, J. Krč, C. Ballif, M. Topič, Opt. Express 23 (2015) A263–A278.
[476] L.M. Mazzarella, M.A.W. Erth, K.L.J. Äger, M.A.J. Ošt, L.A.R.S.K. Orte, S.T.A. Lbrecht, R.U.S. Chlatmann, B. Ernd, S. Tannowski, Opt. Express 26 (2018) A487–A497.
[477] S. Altazin, L. Stepanova, J. Werner, B. Niesen, C. Ballif, B. Ruhstaller, Opt. Express 26 (2018) A579–A590.
[478] L. Mazzarella, Y.H. Lin, S. Kirner, A.B. Morales-Vilches, L. Korte, S. Albrecht, E. Crossland, B. Stannowski, C. Case, H.J. Snaith, R. Schlatmann, Adv. Energy Mater. 9 (2019), 1803241.
[479] Y. Hu, X. Diao, C. Wang, W. Hao, T. Wang, Vacuum 75 (2004) 183–188.
[480] L.-j. Meng, M.P. dos Santos, Thin Solid Films 322 (1998) 56–62.
[481] F. Fu, T. Feurer, T. Jager, E. Avancini, B. Bissig, S. Yoon, S. Buecheler, A.N. Tiwari, Nat. Commun. 6 (2015) 8932.
[482] T. Koida, H. Fujiwara, M. Kondo, Sol. Energy Mater. Sol. Cells 93 (2009) 851–854.
[483] F. Guo, H. Azimi, Y. Hou, T. Przybilla, M. Hu, C. Bronnbauer, S. Langner, E. Spiecker, K. Forberich, C.J. Brabec, Nanoscale 7 (2015) 1642–1649.
[484] T. Gahlmann, K.O. Brinkmann, T. Becker, C. Tückmantel, C. Kreusel, F. gen Hassend, S. Weber, T. Riedl, Adv. Energy Mater. 10 (2020), 1903897.
[485] Y. Kato, L.K. Ono, M.V. Lee, S. Wang, S.R. Raga, Y. Qi, Adv. Mater. Interfaces 2 (2015), 1500195.
[486] S. Svanström, T.J. Jacobsson, G. Boschloo, E.M.J. Johansson, H. Rensmo, U.B. Cappel, ACS Appl. Mater. Interfaces 12 (2020) 7212–7221.
[487] F. Lang, M.A. Gluba, S. Albrecht, J. Rappich, L. Korte, B. Rech, N.H. Nickel, J. Phys. Chem. Lett. 6 (2015) 2745–2750.
[488] Y. Han, S. Meyer, Y. Dkhissi, K. Weber, J.M. Pringle, U. Bach, L. Spiccia, Y.B. Cheng, J. Mater. Chem. A 3 (2015) 8139–8147.
[489] J. Werner, J. Geissbühler, A. Dabirian, S. Nicolay, M. Morales-Masis, S.D. Wolf, B. Niesen, C. Ballif, ACS Appl. Mater. Interfaces 8 (2016) 17260–17267.
[490] H.A. Dewi, H. Wang, J. Li, M. Thway, R. Sridharan, R. Stangl, F. Lin, A.G. Aberle, N. Mathews, A. Bruno, S. Mhaisalkar, ACS Appl. Mater. Interfaces 11 (2019) 34178–34187.
[491] K.A. Bush, C.D. Bailie, Y. Chen, A.R. Bowring, W. Wang, W. Ma, T. Leijtens, F. Moghadam, M.D. McGehee, Adv. Mater. 28 (2016) 3937–3943.
[492] J.A. Raiford, C.C. Boyd, A.F. Palmstrom, E.J. Wolf, B.A. Fearon, J.J. Berry, M.D. McGehee, S.F. Bent, Adv. Energy Mater. 9 (2019), 1902353.
[493] A.J. Bett, P.S.C. Schulze, K.M. Winkler, Ö.S. Kabakli, I. Ketterer, L.E. Mundt, S.K. Reichmuth, G. Siefer, L. Cojocaru, L. Tutsch, M. Bivour, M. Hermle, S.W. Glunz, J.C. Goldschmidt, Prog. Photovolt. Res. Appl. 28 (2020) 99–110.
[494] A.J. Bett, K.M. Winkler, M. Bivour, L. Cojocaru, Ö. Kabakli, P.S.C. Schulze, G. Siefer, L. Tutsch, M. Hermle, S.W. Glunz, J.C. Goldschmidt, ACS Appl. Mater. Interfaces 11 (2019) 45796–45804.
[495] D. Luo, W. Yang, Z. Wang, A. Sadhanala, Q. Hu, Science 360 (2018) 1442–1446.
[496] X. Zheng, B. Chen, J. Dai, Y. Fang, Y. Bai, Y. Lin, H. Wei, Xiao C. Zeng, J. Huang, Nat. Energy 2 (2017) 17102.
[497] Y. Shao, Y. Yuan, J. Huang, Nat. Energy 1 (2016) 15001.
[498] J. Xu, C.C. Boyd, Z.J. Yu, A.F. Palmstrom, D.J. Witter, B.W. Larson, R.M. France, J. Werner, S.P. Harvey, E.J. Wolf, W. Weigand, S. Manzoor, M.F.A.M.V. Hest, J.J. Berry, J.M. Luther, Z.C. Holman, M.D. Mcgehee, Science 367 (2020) 1097–1104.
[499] D.A. Jacobs, M. Langenhorst, F. Sahli, B.S. Richards, T.P. White, C. Ballif, K.R. Catchpole, U.W. Paetzold, J. Phys. Chem. Lett. 10 (2019) 3159–3170.
[500] W.S. Yang, B.-W. Park, E.H. Jung, N.J. Jeon, Y.C. Kim, D.U. Lee, S.S. Shin, J. Seo, E.K. Kim, J.H. Noh, S.I. Seok, Science 356 (2017) 1376–1379.
[501] E.H. Jung, N.J. Jeon, E.Y. Park, C.S. Moon, T.J. Shin, T.Y. Yang, J.H. Noh, J. Seo, Nature 567 (2019) 511–515.
[502] Z. Liu, A. Zhu, F. Cai, L. Tao, Y. Zhou, Z. Zhao, Q. Chen, Y.-B. Cheng, H. Zhou, J. Mater. Chem. A 5 (2017) 6597–6605.
[503] N. Arora, M.I. Dar, A. Hinderhofer, N. Pellet, F. Schreiber, S.M. Zakeeruddin, M. Gratzel, Science 358 (2017) 768–771.
[504] Z. Yu, M. Leilaeioun, Z. Holman, Nat. Energy 1 (2016) 16137.
[505] G.E. Eperon, M.T. Hörantner, H.J. Snaith, Nat. Rev. Chem. 1 (2017) 0095.
[506] M.R. Filip, G.E. Eperon, H.J. Snaith, F. Giustino, Nat. Commun. 5 (2014) 5757.
[507] A. Kojima, K. Teshima, Y. Shirai, T. Miyasaka, J. Am. Chem. Soc. 131 (2009) 6050–6051.
[508] M.M. Lee, J. Teuscher, T. Miyasaka, T.N. Murakami, H.J. Snaith, Science 338 (2012) 643–647.
[509] W. Shockley, H.J. Queisser, J. Appl. Phys. 32 (1961) 510–519.
[510] O. Dupré, A. Tuomiranta, Q. Jeangros, M. Boccard, P. Alet, C. Ballif, IEEE J. Photovolt. 10 (2020) 714–721.
[511] A. Onno, N. Rodkey, A. Asgharzadeh, S. Manzoor, Z.J. Yu, F. Toor, Z.C. Holman, Joule 4 (2020) 580–596.
[512] E.T. Hoke, D.J. Slotcavage, E.R. Dohner, A.R. Bowring, H.I. Karunadasa, M.D. McGehee, Chem. Sci. 6 (2015) 613–617.
[513] H. Min, M. Kim, S.U. Lee, H. Kim, G. Kim, K. Choi, J.H. Lee, S.I. Seok, Science 366 (2019) 749–753.
[514] J. Peng, J.I. Khan, W. Liu, E. Ugur, T. Duong, Y. Wu, H. Shen, K. Wang, H. Dang, E. Aydin, X. Yang, Y. Wan, K.J. Weber, K.R. Catchpole, F. Laquai, S. De Wolf, T.P. White, Adv. Energy Mater. 8 (2018), 1801208.
[515] T. Leijtens, K.A. Bush, R. Prasanna, M.D. McGehee, Nat. Energy 3 (2018) 828–838.
[516] J.H. Noh, S.H. Im, J.H. Heo, T.N. Mandal, S.I. Seok, Nano Lett. 13 (2013) 1764–1769.
[517] R.J. Sutton, G.E. Eperon, L. Miranda, E.S. Parrott, B.A. Kamino, J.B. Patel, M.T. Hörantner, M.B. Johnston, A.A. Haghighirad, D.T. Moore, H.J. Snaith, Adv. Energy Mater. 6 (2016), 1502458.
[518] G.E. Eperon, S.D. Stranks, C. Menelaou, M.B. Johnston, L.M. Herz, H.J. Snaith, Energy Environ. Sci. 7 (2014) 982.
[519] K.A. Bush, K. Frohna, R. Prasanna, R.E. Beal, T. Leijtens, S.A. Swifter, M.D. McGehee, ACS Energy Lett. 3 (2018) 428–435.
[520] T. Duong, H.K. Mulmudi, Y. Wu, X. Fu, H. Shen, J. Peng, N. Wu, H.T. Nguyen, D. MacDonald, M.N. Lockrey, T.P. White, K. Weber, K.R. Catchpole, ACS Appl. Mater. Interfaces 9 (2017) 26859–26866.
[521] D.J. Slotcavage, H.I. Karunadasa, M.D. McGehee, ACS Energy Lett. 1 (2016) 1199–1205.
[522] Y. Zhou, F. Wang, Y. Cao, J.P. Wang, H.H. Fang, M.A. Loi, N. Zhao, C.P. Wong, Adv. Energy Mater. 7 (2017), 1701048.
[523] Y. Yu, C. Wang, C.R. Grice, N. Shrestha, D. Zhao, W. Liao, L. Guan, R.A. Awni, W. Meng, A.J. Cimaroli, K. Zhu, R.J. Ellingson, Y. Yan, ACS Energy Lett. 2 (2017) 1177–1182.
[524] D.H. Kim, C.P. Muzzillo, J. Tong, A.F. Palmstrom, B.W. Larson, C. Choi, S.P. Harvey, S. Glynn, J.B. Whitaker, F. Zhang, Z. Li, H. Lu, M.F.A.M. van Hest, J.J. Berry, L.M. Mansfield, Y. Huang, Y. Yan, K. Zhu, Joule 3 (2019) 1734–1745.
[525] J. Kim, M.I. Saidaminov, H. Tan, Y. Zhao, Y. Kim, J. Choi, J.W. Jo, J. Fan, R. Quintero-Bermudez, Z. Yang, L.N. Quan, M. Wei, O. Voznyy, E.H. Sargent, Adv. Mater. 30 (2018), 1706275.
[526] S. Gharibzadeh, B. Abdollahi Nejand, M. Jakoby, T. Abzieher, D. Hauschild, S. Moghadamzadeh, J.A. Schwenzer, P. Brenner, R. Schmager, A.A. Haghighirad, L. Weinhardt, U. Lemmer, B.S. Richards, I.A. Howard, U.W. Paetzold, Adv. Energy Mater. 9 (2019), 1803699.
[527] J. Yang, B.D. Siempelkamp, E. Mosconi, F. De Angelis, T.L. Kelly, Chem. Mater. 27 (2015) 4229–4236.
[528] T. Leijtens, K. Bush, R. Cheacharoen, R. Beal, A. Bowring, M.D. McGehee, J. Mater. Chem. A 5 (2017) 11483–11500.
[529] B. Conings, J. Drijkoningen, N. Gauquelin, A. Babayigit, J. D'Haen, L. D'Olieslaeger, A. Ethirajan, J. Verbeeck, J. Manca, E. Mosconi, F.D. Angelis, H.-G. Boyen, Adv. Energy Mater. 5 (2015), 1500477.
[530] W. Rehman, R.L. Milot, G.E. Eperon, C. Wehrenfennig, J.L. Boland, H.J. Snaith, M.B. Johnston, L.M. Herz, Adv. Mater. 27 (2015) 7938–7944.

[531] Z. Li, M. Yang, J.S. Park, S.H. Wei, J.J. Berry, K. Zhu, Chem. Mater. 28 (2016) 284–292.
[532] Y. Wang, T. Zhang, M. Kan, Y. Zhao, J. Am. Chem. Soc. 140 (2018) 12345–12348.
[533] Y. Wang, T. Zhang, M. Kan, Y. Li, T. Wang, Y. Zhao, Joule 2 (2018) 2065–2075.
[534] P. Wang, X. Zhang, Y. Zhou, Q. Jiang, Q. Ye, Z. Chu, X. Li, X. Yang, Z. Yin, J. You, Nat. Commun. 9 (2018) 2225.
[535] K. Wang, Z. Jin, L. Liang, H. Bian, D. Bai, H. Wang, J. Zhang, Q. Wang, S. Liu, Nat. Commun. 9 (2018) 4544.
[536] Q. Wang, X. Zheng, Y. Deng, J. Zhao, Z. Chen, J. Huang, Joule 1 (2017) 371–382.
[537] J.A. Steele, H. Jin, I. Dovgaliuk, R.F. Berger, T. Braeckevelt, H. Yuan, C. Martin, E. Solano, K. Lejaeghere, S.M.J. Rogge, C. Notebaert, W. Vandezande, K.P.F. Janssen, B. Goderis, E. Debroye, Y.K. Wang, Y. Dong, D. Ma, M. Saidaminov, H. Tan, Z. Lu, V. Dyadkin, D. Chernyshov, V. Van Speybroeck, E.H. Sargent, J. Hofkens, M.B.J. Roeffaers, Science 365 (2019) 679–684.
[538] S. Essig, S. Ward, M.A. Steiner, D.J. Friedman, J.F. Geisz, P. Stradins, D.L. Young, Energy Procedia 77 (2015) 464–469.
[539] S.E. Sofia, N. Sahraei, J.P. Mailoa, T. Buonassisi, I.M. Peters, IEEE J. Photovolt. 7 (2017) 934–940.
[540] E.L. Warren, W.E. McMahon, M. Rienäcker, K.T. VanSant, R.C. Whitehead, R. Peibst, A.C. Tamboli, ACS Energy Lett. 5 (2020) 1233–1242.
[541] R. Santbergen, H. Uzu, K. Yamamoto, M. Zeman, IEEE J. Photovolt. 9 (2019) 446–451.
[542] E.L. Warren, M.G. Deceglie, M. Rienäcker, R. Peibst, A.C. Tamboli, P. Stradins, Sustain. Energy Fuels 2 (2018) 1141–1147.
[543] M. Schnabel, H. Schulte-Huxel, M. Rienäcker, E.L. Warren, P.F. Ndione, B. Nemeth, T.R. Klein, M.F.A.M. van Hest, J.F. Geisz, R. Peibst, P. Stradins, A.C. Tamboli, Sustain. Energy Fuels 4 (2020) 549–558.
[544] T. Soga, M. Yang, T. Jimbo, M. Umeno, Jpn. J. Appl. Phys. 35 (1996) 1401–1404.
[545] H. Kroemer, J. Cryst. Growth 81 (1987) 193–204.
[546] T.J. Grassman, M.R. Brenner, S. Rajagopalan, R. Unocic, R. Dehoff, M. Mills, H. Fraser, S.A. Ringel, Appl. Phys. Lett. 94 (2009), 232106.
[547] E.L. Warren, A.E. Kibbler, R.M. France, A.G. Norman, P. Stradins, W.E. McMahon, Appl. Phys. Lett. 107 (2015), 082109.
[548] R.M. France, F. Dimroth, T.J. Grassman, R.R. King, MRS Bull. 41 (2016) 202–209.
[549] T.J. Grassman, D.J. Chmielewski, S.D. Carnevale, J.A. Carlin, S.A. Ringel, IEEE J. Photovolt. 6 (2016) 326–331.
[550] M. Feifel, D. Lackner, J. Ohlmann, J. Benick, M. Hermle, F. Dimroth, Sol. RRL 3 (2019), 1900313.
[551] M. Vaisman, N. Jain, Q. Li, K.M. Lau, E. Makoutz, T. Saenz, W.E. McMahon, A.C. Tamboli, E.L. Warren, IEEE J. Photovolt. 8 (2018) 1635–1640.
[552] T. Tayagaki, K. Makita, T. Tachibana, H. Mizuno, R. Oshima, H. Takato, T. Sugaya, IEEE J. Photovolt. 10 (2020) 358–362.
[553] E. Veinberg-Vidal, L. Vauche, K. Medjoubi, C. Weick, C. Besançon, P. Garcia-Linares, A. Datas, A. Kaminski-Cachopo, P. Voarino, P. Mur, J. Decobert, C. Dupré, Prog. Photovolt. Res. Appl. 27 (2019) 652–661.
[554] R. Cariou, J. Benick, F. Feldmann, O. Höhn, H. Hauser, P. Beutel, N. Razek, M. Wimplinger, B. Bläsi, D. Lackner, M. Hermle, G. Siefer, S.W. Glunz, A.W. Bett, F. Dimroth, Nat. Energy 3 (2018) 326–333.
[555] S. Essig, J. Benick, M. Schachtner, A. Wekkeli, M. Hermle, F. Dimroth, IEEE J. Photovolt. 5 (2015) 977–981.
[556] K. Derendorf, S. Essig, E. Oliva, V. Klinger, T. Roesener, S.P. Philipps, J. Benick, M. Hermle, M. Schachtner, G. Siefer, W. Jäger, F. Dimroth, IEEE J. Photovolt. 3 (2013) 1423–1428.
[557] K. Makita, H. Mizuno, T. Tayagaki, T. Aihara, R. Oshima, Y. Shoji, H. Sai, H. Takato, R. Müller, P. Beutel, D. Lackner, J. Benick, M. Hermle, F. Dimroth, T. Sugaya, Prog. Photovolt. Res. Appl. 28 (2020) 16–24.
[558] A.C. Tamboli, S. Essig, K.A.W. Horowitz, M. Woodhouse, M.F.A.M.v. Hest, A.G. Norman, M.A. Steiner, P. Stradins, Indium Zinc Oxide Mediated Wafer Bonding for III–V/Si Tandem Solar Cells, In: IEEE 42nd Photovoltaic Specialist Conference, 2015.
[559] T.R. Klein, B.G. Lee, M. Schnabel, E.L. Warren, P. Stradins, A.C. Tamboli, M.F.A.M. van Hest, ACS Appl. Mater. Interfaces 10 (2018) 8086–8091.
[560] U. Heitmann, O. Höhn, H. Hauser, S. Kluska, J. Bartsch, S. Janz, AIP Conf. Proc. 2147 (2019), 130001.
[561] K.T. VanSant, J. Simon, J.F. Geisz, E.L. Warren, K.L. Schulte, A.J. Ptak, M.S. Young, M. Rienäcker, H. Schulte-Huxel, R. Peibst, A.C. Tamboli, ACS Appl. Energy Mater. 2 (2019) 2375–2380.
[562] H. Schulte-Huxel, D.J. Friedman, A.C. Tamboli, IEEE J. Photovolt. 8 (2018) 1370–1375.
[563] K. Araki, H. Tawa, H. Saiki, Y. Ota, K. Nishioka, M. Yamaguchi, Appl. Sci. 10 (2020) 2529.

Yuqiang Liu currently is a postdoc. scholar in Energy Materials and Surface Sciences Unit at Okinawa Institute of Science and Technology Graduate University in Japan. He obtained his Ph.D. from Institute of Functional Nano & Soft Materials, Soochow University, China. His current research focuses on recombination mechanism of perovskite light-emitting diodes and device engineering of organic/inorganic hybrid solar cells.

Yajuan Li is a postdoctoral in Institute of Functional Nano & Soft Materials, Soochow University, China. She received her Ph.D. in Physical Chemistry at Dalian Institute of Chemical Physics (DICP), Chinese Academy of Science. Her main research field is electrochemical energy storage, water energy harvesting, halide perovskite solar cells, and carrier selective contacts for crystal silicon solar cells.

Yiliang Wu is an ACAP (Australian Centre for Advanced Photovoltaics) research fellow at Australian National University, Australia, where he received his Ph.D. in renewable engineering. His main research field is perovskite solar cells, study on hysteresis mechanism, and monolithic perovskite/c-Si tandem solar cells.

Guangtao Yang received his Ph.D. degree from the Photovoltaic Materials and Devices group in Delft University of Technology, the Netherlands, in 2015. After his PhD, he worked as postdoc. researcher in Delft University of Technology and then Eindhoven University of Technology on the c-Si solar cells research topics. He joined Delft University of Technology as a postdoc researcher again in 2018 with focusing on the research of c-Si solar cells with passivating contacts, including passivating contacts material optimization and solar cell device fabrication.

Luana Mazzarella is postdoc researcher at Delft University of Technology, the Netherlands, in the Photovoltaic Materials and Devices group. In 2013 she joined the PVcomB group at Helmholtz Zentrum Berlin to pursue her Ph.D. on the development of innovative contact materials and device concepts in silicon heterojunction solar cells. She received her Ph.D. degree at the Technische Universität Berlin in 2017 with the highest grade. After the first postdoc. activity at the Institute for Silicon Photovoltaics, Helmholtz-Zentrum Berlin, working on monolithic c-Si/perovskite tandem devices, she joined the Photovoltaic Materials and Devices group in Delft in 2018. Her research interests include passivating contacts for high-efficiency cells based on alloyed thin-film silicon and poly-Si materials, transition metal oxides and hybrid tandem solar cells.

Paul Procel-Moya received his Ph.D. degree from the University of Calabria, Rende, Italy in 2017 for his research in numerical simulations of advanced silicon solar cells. In 2015, for an internship, he joined the Photovoltaic Materials and Devices Group at Delft University of Technology, where he worked on advanced opto-electrical simulations of solar cells. From 2017, he joined Delft University of Technology as a postdoc. researcher focusing on design and development of silicon heterojunction solar cells. His research interests include opto-electrical simulations and design of solar cells and semiconductor devices using novel concepts and material structures.

Adele Tamboli received her Ph.D. in Materials from the University of California, Santa Barbara, in 2009, followed by postdoc. research in Applied Physics at the California Institute of Technology. She cur-

rently works in the Materials Science Center at the National Renewable Energy Laboratory in Golden, Colorado, and holds a joint appointment at the Colorado School of Mines. Her research focuses on improved device architectures for multijunction solar cells, including three- and four-terminal, III-V/Si tandems. She also has an active research program in the discovery and development of new semiconductor materials for energy applications.

Klaus Weber is Associate Professor in the Research School of Electrical, Energy and Materials Engineering at the Australian National University (ANU), Canberra, Australia. He received his Ph.D. in Engineering from the ANU. He has carried out pioneering work in silicon photovoltaics, including the development of several innovative thin silicon solar cell architectures which were transferred to industry. His current research focuses on perovskite photovoltaics, with a particular focus on addressing commercialisation challenges of the technology.

Mathieu Boccard received his PhD from EPFL, PVlab in 2012 for his work on thin-film-silicon tandem solar cells. He then joined ASU, Tempe (USA) for a postdoc. Research on high-efficiency crystalline silicon, CdTe-based and perovskite/silicon tandem solar cells. Since 2017, he is leading the silicon heterojunction activities in EPFL, PVlab, working on fundamental aspects and novel-material development for carrier-selective contacts and multijunction devices.

Olindo Isabella is an associate professor at Delft University of Technology, the Netherlands, where he leads the Photovoltaic Materials and Devices group. He received his Ph.D. cum laude in Opto-Electronics at Delft University of Technology. After a research visiting period at the National Institute of Advanced Industrial Science and Technology, Japan, he joined the Photovoltaic Materials and Devices group in 2013. His research interests span across the PV value chain, from solar energy materials to c-Si and hybrid tandem solar cells, smart and multi-functional PV modules and X-Integrated PV Systems.

Xinbo Yang is a professor in College of Energy, Soochow Institute for Energy and Materials InnovationS (SIEMIS), Soochow University, China. He received his Ph.D. degree in Materials Science from the Chinese Academy of Sciences in 2010. He was a JSPS Fellow in Tohoku University, an ARENA Fellow in the Australian National University and a research scientist in King Abdullah University of Science and Technology (KAUST) in Saudi Arabia. His current research interests include high efficiency silicon solar cells with advanced passivating contact technologies, perovskite/silicon tandem solar cells, and novel solar cell materials and concepts.

Baoquan Sun is a chair professor in Institute of Functional Nano & Soft Materials, Soochow University, China. He received his Ph.D. in Chemistry Materials at Tsinghua University in Beijing. After being postdoc. research in Cavendish Laboratory at Cambridge University and Los Alamos National Laboratory, he joined Institute of Functional and Soft Materials in 2008. His main research field is nanostructured semiconductor materials, conducting ink, charge separation and transport, interface engineering for flexible electronics, light emitting diodes and organic/inorganic silicon heterojunction solar cells.